THE INTERFACIAL FAILURE OF BONDED MATERIALS AND COMPOSITES

By

Arun Krishnan

Dissertation

Submitted to the Faculty of the

Graduate School of Vanderbilt University

in partial fulfillment of the requirements for the degree of

DOCTOR OF PHILOSOPHY

in

Civil Engineering

December, 2010

Nashville, Tennessee

Members of Dissertation Committee

Professor Caglar Oskay (Chair)

Professor Prodyot K. Basu

Professor Sankaran Mahadevan

Professor Carol A. Rubin

Professor Luoyu R. Xu

ABSTRACT

Composites and adhesive joints are being increasingly used in modern structures. It becomes very important to characterize the failure in such materials especially at the interface between constituents. This dissertation is focused on interfacial failure in composites and bonded polymers. A short-beam shear fracture approach is developed to measure the mode-II fracture toughness of materials with a preferred interface. This method is more efficient than previous methods due to minimal friction between crack faces. A novel failure criterion proposed by Leguillon (2002) is used to predict crack initiation from notches. This dissertation advances the scope of this criterion to predict failure from notches with a connected interface. Same- and bi-material systems are tested under three-point bending to provide relevant data for verification which is also expected to be a benchmark for future numerical simulations. Finally, the compression-after-impact (CAI) of glass/vinyl ester composites subject to sea water aging is investigated experimentally. A reduced order multiscale computational model is used to explain the damage mechanisms in the composite and to capture the experimental degradation in CAI strength.

To my wonderful parents, Dr. S.R. Krishnan and Ms. Latha Krishnan,

and to my dear sister Anu Krishnan

ACKNOWLEDGEMENTS

This thesis would not have been possible without the support of several amazing people. I thank both my advisors Dr. Caglar Oskay and Dr. Luoyu Roy Xu for their guidance, support, motivation, enthusiasm and commitment. I am very grateful to Dr. Oskay for his excellent advice and unstinted support. I have thoroughly enjoyed working with both my advisors. I am deeply indebted to Prof. P.K. Basu for his expert guidance and administrative help throughout my graduate years. I would like to thank Prof. Sankaran Mahadevan for his interest in my graduate studies and also for his role in this dissertation as a committee member. I also thank my committee member Prof. Carol Rubin for her valuable inputs to my research. I thank Prof. David Kosson and the Department of Civil Engineering at Vanderbilt for their financial and academic support. This dissertation has been funded by the NSF and the ONR.

I acknowledge Dr. Anna Pandolfi for mentoring my research during my stay in Politecnico di Milano, Milan, Italy. I thank Prof. Dominique Leguillon and Dr. Van-Xuan Tran of University of Pierre and Marie Curie, Paris for their valuable inputs to my research. I also thank Prof. Uday Vaidya and Dr. Haibin Ning for their assistance in preparation of marine composite samples and for allowing me to use their lab facilities at University of Alabama, Birmingham. I acknowledge Mr. John Fellenstein for machining my specimens. I also thank all my friends, group mates and office mates at Vanderbilt for making my stay at Vandy an enjoyable and a memorable one.

I express my sincere and heartfelt thanks to my parents Dr. S.R. Krishnan and Ms. Latha Krishnan for their unconditional support and mentoring throughout my life. I also

thank my sister Ms. Anu Krishnan for her constant motivation. I would not have completed my PhD if not for my family's love, affection and care. I dedicate this dissertation to my parents and sister.

TABLE OF CONTENTS

LIST OF TABLES

LIST OF FIGURES

CHAPTER I

INTRODUCTION

1.1 Overview

Failure prediction is critical to ensure the optimal performance of structures involving advanced materials, like marine vehicles, aerospace structures and space vehicles. Significant advances in the field of fracture mechanics since the Second World War have offset the problem of failure in structures. However, the increase in complexity and the need for greater accuracy in modern structures have precipitated the need for novel failure criterions to be incorporated into design in order to avert failure (Anderson, 2004). Failure results from the weakest link in a structure. This is often the interface between two or more types of materials. In case of composites it becomes the fiber/matrix interface and in case of bonded polymers, the bonding line is the interface. Fracture resistance of composite materials is strongly influenced by the constituent interfacial toughness. Reliability of microelectronic devices, adhesively bonded joints and coatings subject to harsh environmental conditions depend on the strength of the interface (Liechti and Chai, 1991). The failure mechanism in a human tooth has been shown to be adhesive or adhesive-cohesive depending on the interfacial fracture toughness of the dentin-resin interface (Lin and Douglas, 1994). Recently, enhanced interface interactions between the carbon nanotubes (fiber) and epoxy (matrix) have been shown to improve the flexural strength and fracture toughness of polymer nanocomposites (Geng et al., 2008). These mechanical and fracture properties have been found to increase with increasing carbon nanotube volume fraction due to interfacial

interactions which is usually not observed in the absence of interface treatment (Xu et al., 2004). These and several other applications demonstrate the importance of studying failure along the interface in advanced materials to prevent catastrophic disasters at many different scales. In order to achieve this, we need a combination of fundamental theoretical work coupled with experimental work involving applications to real life.

Composite materials and polymers have started replacing metals and alloys due to their higher strength-to-weight ratio, superior environmental resistance and improved fatigue properties (Cantwell and Morton, 1991). Additionally, composites offer a higher general overall performance at a lower manufacturing cost than metals. To illustrate the importance of composites in modern structures, the Boeing 787 aircraft is taken as an example. The new Boeing 787 aircraft uses about 50% by weight (and 80% by volume) of composites in its construction. This is much higher than its predecessor, the Boeing 777 which used only about 12% by weight of composite materials (Boeing 787 Fact sheet). Polymer composite materials (PMC) are being increasingly used by the US navy on ships and aircrafts in the last half century (ONR fact sheet). Composites are being used as primary and secondary load-bearing members in lightweight foundations, deckhouses and masts, machinery components, pumps, heat exchangers, and in auxiliary items in naval ships (Sorathia et al., 1999). The universal use of composites in several disciplines has necessitated an urgent need for novel material testing methods. These methods need to be cost-effective and utilize minimal material while providing accurate values of mechanical and fracture properties. High performance composites are being used in harsh environmental conditions including constant sea water exposure, high temperature, high pressures and severe chemical exposure. In such cases, it becomes

important to characterize relevant composite material properties under environmental aged conditions.

This dissertation is focused on the study of interfacial failure in composites and bonded polymers. This involves an integration of experimental and numerical approaches to characterize and understand the mechanical properties of composite and bonded polymer materials. An experimental method is developed to accurately measure interfacial fracture toughness (Krishnan and Xu, 2010). Experiments are carried on out bonded polymers to study the influence of a notch on an interface. A rich set of data including load-displacement curves, crack paths, fringe pictures and experimental data points are presented. This is expected to be useful benchmark for current and future computational methods. The durability of composites is characterized by subjecting marine high performance composites to sea water exposure over a time period of 30 months. A numerical analysis of the same is carried out using a reduced order multiscale computational model with changes incorporated due to sea water exposure.

1.2 Organization

This dissertation is organized into five chapters. Chapter 1 presents an introduction to the research objectives and presents the organization of the dissertation. Chapter 2 presents a short-beam shear fracture (SBSF) approach to measure the mode II fracture toughness of materials with preferred interfaces and composites materials. The experimental preparation, testing of specimens and numerical validation of the pure shear fracture test is included in this chapter. Chapter 3 discusses the experimental preparation, testing and analysis of notch interface specimens in detail. This investigation is

conducted to study the combined influence of a notch and an interface on the failure mechanics of brittle materials. A novel failure criterion is validated using the experimental approach presented in Chapter 3. Chapter 4 presents a combined experimental and numerical investigation into the compression-after-impact response of sea water aged E-glass/vinyl ester composites. The first part of Chapter 4 describes the preparation and testing of marine composite specimens and their corresponding degradation in material properties when subjected to sea water aging. The second part of Chapter 4 presents a numerical model of the compression mechanism. Chapter 5 is a conclusion to the dissertation.

1.3 Objectives and Motivation

The three major objectives of this dissertation are briefly described below. Each of the objectives is explained in significant detail in the following chapters.

1.3.1 Objective 1: Short-Beam Shear Fracture approach

With the increasing pace of computational research, it becomes important to present reliable and relevant experimental data for efficient research. It becomes necessary to introduce novel experimental methods to calculate complicated experimental parameters. The fracture toughness is one such parameter for which existing experimental procedures require careful preparation and testing. In this proposal a novel method for measuring the mode-II fracture toughness is introduced. This method is based on an existing shear fixture and also requires simple tools and little understanding of complicated fracture mechanics principles. This method is also shown to measure the

pure mode-II fracture toughness thereby placing it in an elite set of experiments designed at isolating the fracture modes.

The mode II fracture toughness is difficult to measure due to crack kinking (Anderson, 2004), which ensures that existing methods do not provide an accurate value. A mode II crack is possible only for special materials with preferred interfaces like wood, bonded materials or composite materials. For unidirectional composite materials with fiber/matrix interfaces, a mode II crack is possible due to the strong constraining of fibers to suppress any kinked cracks, as has been shown in recent dynamic shear crack experiments by Coker and Rosakis (2001). A prominent experimental approach to measure the mode II interlaminar fracture toughness of fiber-reinforced composite materials is the end-notched flexure test (Daniel and Ishai, 2005). But this beam bending test requires cumbersome numerical procedures like data reduction methods to correct for the shear and crack tip deflection (Yoshihara and Satoh, 2009). This tends to complicate the experimental measurement of the mode II fracture toughness which is a fundamental material property.

A critical issue hindering the usefulness of such beam bending experiments in conjunction with Linear Elastics Fracture Mechanics (LEFM) analysis is the significant absence of the “K-dominance zone” in these thin composite beams. Also these beam bending methods are unable to eliminate friction between the cracked faces, behind the crack tip which can cause significant increase in values of K_{IIC} higher than the intrinsic values. For other non-beam bending methods, it has been shown that the compressive stresses ahead of the crack tip significantly affect the mode II fracture toughness of composite materials (Bing and Sun, 2007). Also, the values of the measured mode II

fracture toughnesses are strongly dependent on the type of test used and show a wide variation. With the extensive applications of composite materials, it is very important to develop new approaches to measure the mode II fracture toughnesses.

The Iosipescu shear test has been used to measure shear strength of composites and bonded polymers. The advantage of this method is the presence of zero interfacial normal stress (zero bending moment) at the specimen center and this is used to develop an efficient experimental method in determining the mode II fracture toughness of bonded polymers. This method, which is based on the Iosipescu fixture, minimizes the effect of friction on the mode-II fracture toughness. A theoretical formula is derived and is verified using finite element analysis. This formula is extended to include composite materials and a calibration chart is provided. Experimental specimens of bonded polymers are tested to measure fracture toughness values and the load-displacement curves are verified numerically using cohesive element simulation. The current objective is to measure the mode-II fracture toughness alone with our approach, which is much easier to use than previous ones.

1.3.2 Objective 2: Experimental investigation into notch-interface interactions

While fracture mechanics has a wealth of literature on cracks, there is little research on notches. Indeed a crack is only a special case of a notch with notch angle of 0^o as treated in the Williams (1952) expansion. Notches in the form of re-entrant corners are found in many simple and complex real-life applications. An example would be the wing design for a joint striker as shown in Fig. 1.1. Crack onset at a notch with a connected interface is still an open problem with few researchers developing reliable

failure criterions. Developing a generalized notch-interface failure criterion is very important from a fundamental failure mechanics viewpoint and for engineering applications.

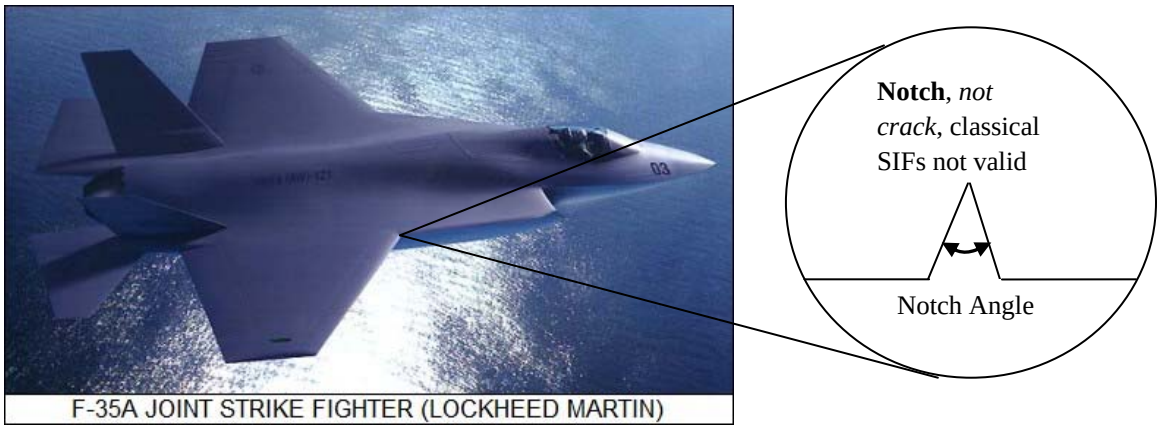

Fig. 1.1 Schematic diagram showing presence of notches in real life applications.

In this dissertation, novel experimental work is conducted in order to generate a rich amount of experimental data which can serve as a benchmark for current and future theoretical and computational work. The experimental data also provide interesting results for the numerical simulation of the involved crack propagation problem as well. While experimental investigations have been conducted for notched polymer specimens (Dunn et al., 1997a), the problem of notched specimens with an interface does not have any experimental validation. A novel failure criterion proposed by Leguillon (2002) is a combination of a strength and fracture criterion. The strength criterion should involve the presence of shear and normal stress in order to address the presence of an interface. Our work also presents experimental data which will be valuable for numerical simulation of

two problems: crack initiation at the notch tip and crack propagation along the interface including subsequent kinking into bulk material.

1.3.3 Objective 3: Experimental and numerical modeling of compression-after-impact

Composite materials are increasingly being used in the construction of boats, recreational ships and naval warships. The naval environment is very unique due to the presence of increased and constant exposure to moisture and due to the effect of tidal wave pressure. Also, there might be blast loading due to underwater explosions in the sea similar to the one shown in Fig. 1.2. All these pose a great challenge to the design of composites for marine structures. To address this issue, an actual face plate of a sandwich composite is subject to sea water aging and this is followed by compression after impact testing.

Composites are currently being used in ship construction and in underwater structures. Constant exposure to seawater makes durability and dynamic failure properties critical for naval composite ships. However, previous approaches and measurements have significantly underestimated the actual durability of a composite structure inside seawater. While a real ship has only side exposed to sea water, experimental approaches tend to immerse the composite samples in sea water. This causes a significant property reduction which is not the case in reality. In this experimental investigation, a ‘fish tank’ is made out of marine composite samples. The individual panels are tested under compression after impact after different aging times. This provides a curve of strength degradation over a time of about 30 months. A reduced order multiscale homogenization model is used to model the degradation in strength with

time. Our model captures the decrease in compression-after-impact strength with time and shows that this is a property of the structural geometry of the composite and not of the material.

Fig. 1.2 Unique naval environment (blast loading due to underwater explosion) poses challenges to design of composite ships.

1.4 Conclusions

This dissertation is focused on failure at the interface in case of bonded polymers and composite materials. Three objectives involving experimental investigations and numerical simulations are undertaken in this dissertation. A new approach to measure fracture toughness is proposed which is expected to be useful and practical in the composite industry. Experimental investigations are undertaken to assist in the verification of a novel failure criterion to predict fracture initiation from a notch

connected with an interface. Finally, a combined experimental and numerical investigation to model the compression-after-impact strength of marine composites is conducted. Results and discussions from these objectives are presented in the next three chapters.

CHAPTER II

A SHORT-BEAM SHEAR FRACTURE APPROACH TO MEASURE MODE-II FRACTURE TOUGHNESS

2.1 Introduction

The mode II fracture toughness has long been a difficult property to quantify for isotropic materials as a mode II crack tends to kink away from the main crack (Anderson, 2004), and thereby makes the measured fracture toughness indeed the mode I fracture toughness. A mode II crack is possible only for special materials with preferred interfaces like wood, bonded materials or composite materials. For unidirectional composite materials with fiber/matrix interfaces, a mode II crack is possible due to the strong constraining of fibers to suppress any kinked cracks. This has been shown in recent dynamic shear crack experiments by Coker and Rosakis (2001). Therefore, several experimental approaches have been proposed to measure the mode II interlaminar fracture toughness of fiber-reinforced composite materials such as the end-notched flexure test (Daniel and Ishai, 2005; Arrese et al., 2010; Yoshihara, 2010). But, these beam bending tests usually require numerical procedures like data reduction methods to correct for the shear and crack tip deflection (Wang and Qiao, 2004; Yoshihara and Satoh, 2009). Friction between the crack faces is another reason for fluctuations in results. The influence of friction on the energy release rate and compliance has been discussed in Gradin et al. (1991). These issues tend to complicate the experimental measurement of the mode II fracture toughness which is a fundamental material property.

A critical issue in beam bending experiments in conjunction with Linear Elastics Fracture Mechanics (LEFM) analysis is the significant absence of the "K-dominance zone" in these thin composite beams (Rosakis and Ravi-Chandar, 1986; Sun, 2008; Qian and Sun, 2008; Sun and Qian, 2009). On the other hand, most of these beam bending methods are unable to eliminate friction between the cracked faces, behind the crack tip. This can cause a significant increase in values of K_{IIC} which become higher than the intrinsic values. For other non-beam bending methods, it has been shown that the compressive stresses ahead of the crack tip significantly affect the mode II fracture toughness of composite materials (Bing and Sun, 2007). Also, the values of the measured mode II fracture toughnesses are strongly dependent on the type of test used and show a wide variation (Ayatollahi and Aliha, 2006). With the extensive applications of composite materials, it is very important to develop new approaches to measure the mode II fracture toughnesses.

The Iosipescu shear test has been developed and extensively modified to measure the shear strength of composites and bonded polymers (Walrath and Adams, 1983; Sullivan et al., 1984; Grediac et al., 1994; El-Hajjar and Haj-Ali, 2004; Melin and Neumister, 2006). This fixture has been used to characterize the shear strength of short-beam shear specimens; and the average shear strengths are found to be very close to the shear strengths of the Iosipescu shear specimens in spite of very different interfacial shear stress distributions (Krishnan and Xu, 2010). In the current investigation, the advantage of having zero interfacial normal stress (zero bending moment) at the specimen center is used to develop an efficient experimental method to determine the mode II fracture toughness of bonded polymers. The proposed short-beam shear fracture (SBSF)

approach, which is based on the Iosipescu fixture, minimizes the effect of friction on the mode-II fracture toughness. A theoretical formula is derived and is verified using finite element analysis. This formula is extended to include composite materials and a calibration chart is provided. Experimental specimens of bonded polymers are tested to measure fracture toughness values and the load-displacement curves are verified numerically using cohesive element simulation. Additionally, four-point bending fracture tests are conducted to compare with the fracture toughness values obtained from the short-beam shear fracture (SBSF) experiment using the Iosipescu fixture. Previously, Bansal and Kumosa (1998) have proposed a "Double Edge-Crack" Iosipescu shear specimen to measure the mixed-mode fracture toughness of composite materials subjected to biaxial loads. The current objective, however, is to measure the mode-II fracture toughness alone with our approach, which is much easier to use than previous ones.

2.2 Theoretical Background

2.2.1 Formula for homogenous materials

The stress intensity factors of an asymmetric four-point bend specimen (Fig. 2.1) have been calculated by Suresh et al., (1990)

$$K_I = 6\tau\sqrt{\pi a}\,\frac{S}{W}F_I^{4PB}\left(\frac{a}{W}\right) \tag{2.1}$$

$$K_{II} = \tau\sqrt{\pi a}F_{II}^{4PB}\left(\frac{a}{W}\right) \tag{2.2}$$

Where K_I and K_{II} are the mode I and mode II stress intensity factors respectively; τ is the shear stress across the interface, W is the specimen width, a is the crack length and S is the off-set distance between the crack plane and the loading point. F_I^{4PB} and F_{II}^{4PB} are dimensionless functions of a/W and are provided in Suresh et al. (1990) for four-point bending.

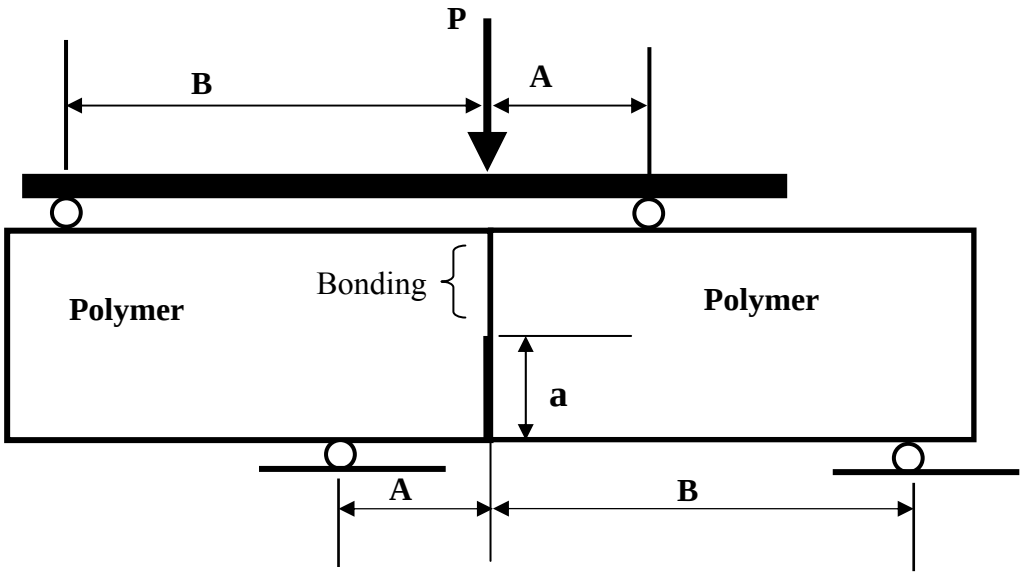

Fig. 2.1 Schematic diagram of a four-point bending test

Additionally, the shear stress per unit thickness can be expressed as

$$\tau = \frac{P}{W}\frac{A-B}{A+B} \tag{2.3}$$

Here, *P* is the applied load, *A* and *B* are distances of the loading points from the center as shown in Fig. 2.1. Since, there is no offset S in our case, the mode-I stress intensity factor is 0. The mode-II stress intensity factor for four-point bending specimens can then be represented as,

$$K_{II} = \frac{P}{Wt}\left(\frac{A-B}{A+B}\right)\sqrt{\pi a}F_{II}^{4PB}\left(\frac{a}{W}\right) \tag{2.4}$$

We choose A and B values of 20 mm and 40 mm respectively for four-point bending tests.

In this investigation, a short-beam shear fracture specimen (Fig. 2.2(a)) with a bonded interface is chosen to match those dimensions required for a widely used Iosipescu test fixture (Krishnan and Xu, 2010). This approach to measure mode-II fracture toughness is a novel approach which has not been proposed before. The proposed test is based on the Iosipescu test fixture which is an ASTM standard (D5379) for measurement of shear strength of composite materials. The short-beam shear fracture test is indeed an asymmetric four-point bend test. We choose specific adhesives with similar Young's modulus as the bonded polymers (Young's modulus is 1-5GPa). Also, the actual thickness of the adhesive interface is only of the order of the micrometers, which is negligible in comparison with other dimensions of the specimen. Thus, the bonded same-material specimen can be treated as homogenous materials, however is not isotropic as the strength/fracture toughness along the adhesive interface will be different from the strength/fracture toughness of the bulk material. The loads on the Iosipescu fixture are applied in the form of displacements on anti-symmetric loading blocks. The corresponding loads are not point loads and are applied from the loading blocks in the form of highly non-linear line loads. However, these loads can be expressed as equivalent point loads acting at a specific distance from the center line as shown in Fig. 2.1. Therefore, these two kinds of specimens have the same shape of the shear force and moment diagrams, as shown in Fig. 2.2(b). Based on statics analysis, since the bending

moment is zero at the both specimen centers, the bending normal stress and then the mode-I fracture toughness should be zero.

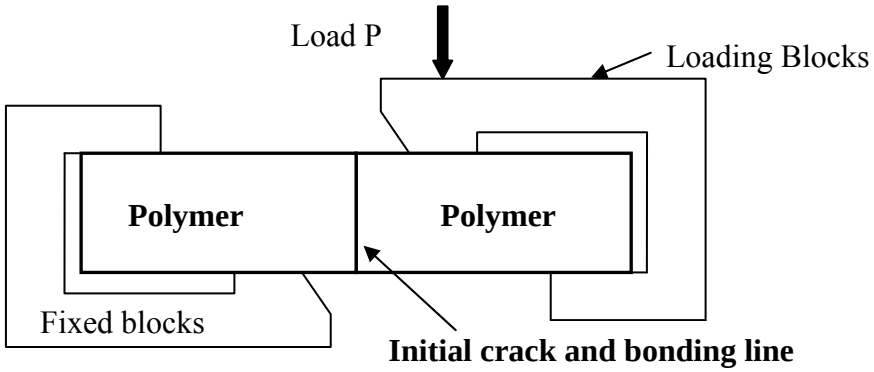

Fig. 2.2 (a) Schematic diagram of the short-beam shear fracture test with loading blocks in the Iosipescu fixture

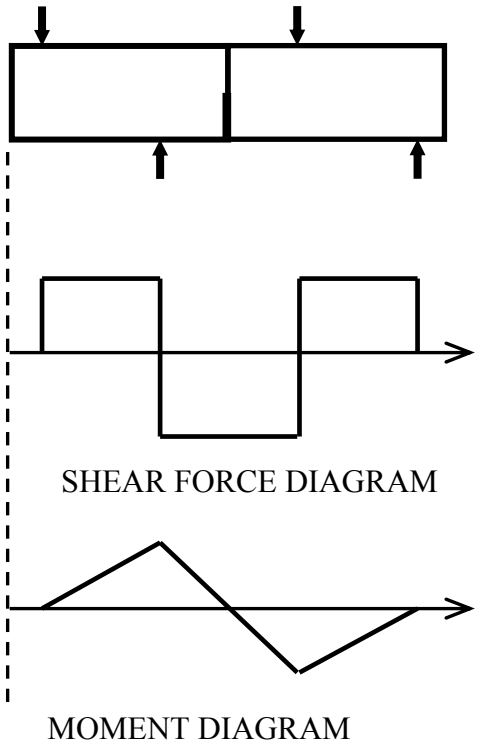

Fig. 2.2 (b) Shear force and moment diagrams for both four-point bending specimen and short-beam shear fracture specimen.

Meanwhile, the shear force around the specimen center is a constant over a wide range of applied displacements and elastic moduli, which is a great advantage for a pure shear fracture experiment. It should be noticed that the shear force of the specimen center for the four-point bending test is P(A-B)/(A+B), which is different from the shear force of the SBSF test (V=P).

For a short-beam shear fracture specimen, equivalent points *A* and *B* are calculated to be 16 mm and 34.5 mm for isotropic materials. These values are calculated from finite element simulations with the corresponding procedure outlined later in this chapter. The average shear stress per unit thickness for the short-beam shear fracture specimen in an Iosipescu fixture is expressed as

$$\tau = \frac{P}{W} \tag{2.5}$$

Therefore, we obtain the formula for K_{II} for short-beam shear fracture specimens as

$$K_{II} = \frac{P}{Wt}\sqrt{\pi a}F_{II}^{SBSF}\left(\frac{a}{W}\right) \tag{2.6}$$

Here, *t* is the thickness of the short-beam shear specimen and F_{II}^{SBS} is a dimensionless constant. Also, in the present case, we use *a/W* of 0.5 for the convenient purpose of specimen preparations. The constant F_{II}^{SBS} is determined using finite element simulations (described later) as 1.379. Also, the critical energy release rate or fracture toughness G_{IIC} can be expressed as

$$G_{IIC} = \frac{K_{IIC}^{\ 2}}{E^*} \tag{2.7}$$

Therefore, from equation (2.6), the fracture toughness G_{IIC} for the short-beam shear fracture can be expressed as

$$G_{IIC} = \frac{\left(F_{II}^{SBSF}\right)^2}{E^*}\left(\frac{P_C}{W}\right)^2 \frac{\pi a}{t^2} \tag{2.8}$$

Here, E^* is the effective plane elastic modulus for both plane stress and strain cases and P_C is the critical load at the crack initiation in the specimen.

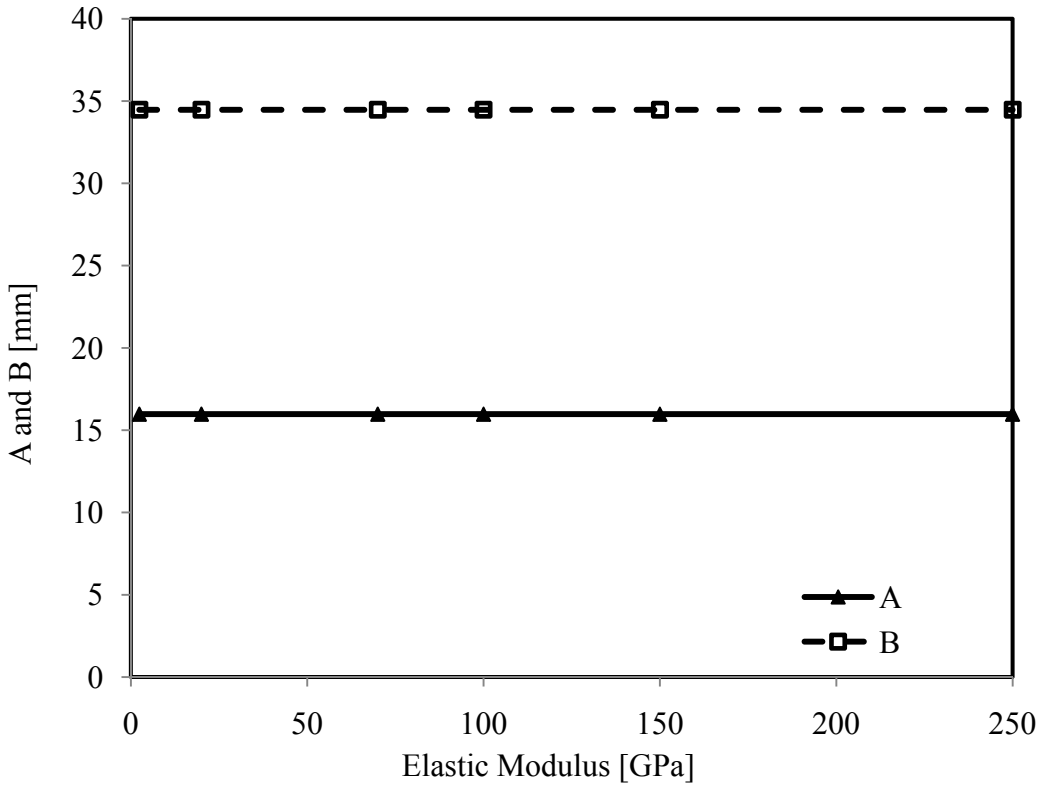

Fig. 2.3 Finite element analysis results showing very small variations of *A* and *B* with a wide range of elastic moduli under an applied displacement of 0.2 mm

Equations (2.6) and (2.8) are valid for our short-beam shear specimen when an Iosipescu fixture is used. The applicability of equation (2.7) is tested over a wide range of elastic

moduli and applied displacements. This validity is checked by obtaining equivalent values of *A* and *B* over a variety of elastic moduli. Values of *A* and *B* remain constant for a wide range of elastic moduli (at a constant applied displacement of 0.2 mm) as shown in Fig. 2.4, and for a wide range of applied displacement (at a constant elastic modulus of 2.4 GPa), as shown in Fig. 2.3. This demonstrates that equation (2.8) is valid for most engineering materials. In our simulation, applied displacement is up to 4.0 mm, which is much larger than the actual displacement in our experiments (around 1.0 mm).

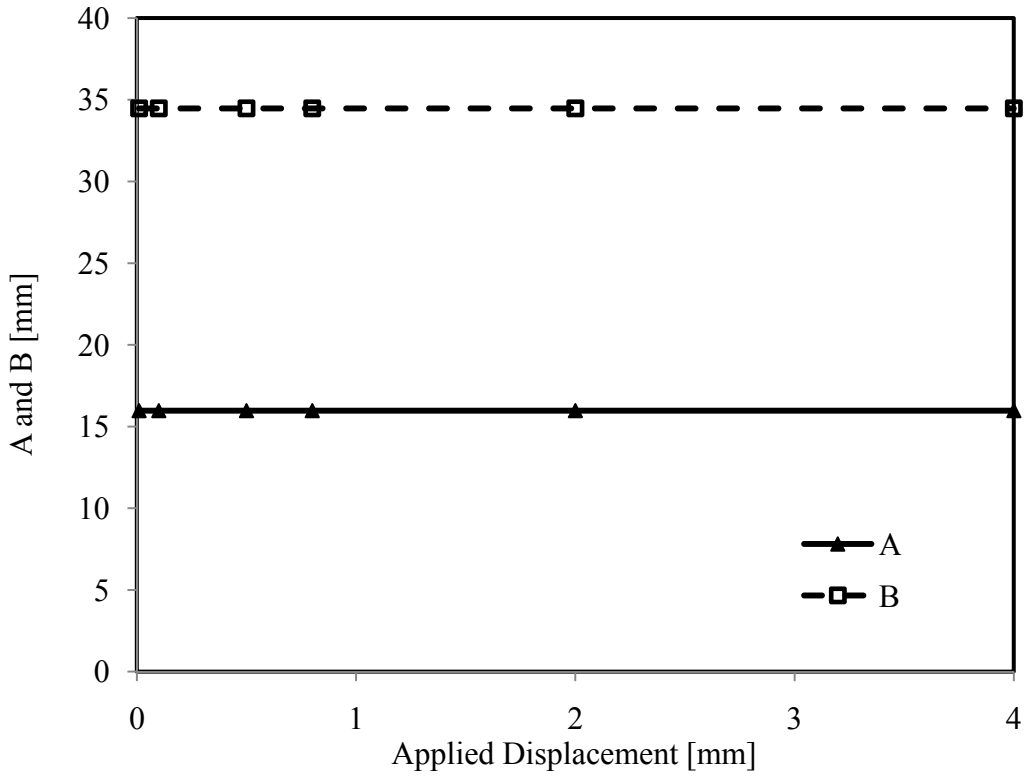

Fig. 2.4 Finite element analysis results showing very small variations of *A* and *B* with a wide range of applied displacements for polymeric specimen with an elastic modulus of 2.4 GPa

2.2.2 Formula for orthotropic fibrous composite materials

The above discussion can be extended to orthotropic materials such as unidirectional fiber composite materials as shown in Fig. 2.5. A similar analysis to determine the fracture toughness of composite materials is conducted. First, the effective plane elastic modulus of the composite materials is calculated by using the formula presented below (Sih et al., 1965; Xu et al., 1996)

$$\frac{1}{E^*} = \frac{1}{\sqrt{2}E_{22}}\sqrt{\sqrt{\frac{E_{22}}{E_{11}}} + \left(\frac{1}{G_{12}} - \frac{2\nu_{12}}{E_{11}}\right)\frac{E_{22}}{2}} \tag{2.8}$$

Here, E_{11} and E_{22} are the elastic moduli of the composite in the fiber (longitudinal) and transverse directions. In this investigation, the mode-II crack path should be the same direction with the fiber, or equivalently the fibers should be along the y direction. The local 1-2 coordinate system is shown in Fig. 2.5. G_{12} is the shear modulus of the composite and ν_{12} is the Poisson's ratio of the composite. The fracture energy can then be calculated by using the same relationship in equation (2.8), but by using the effective Young's modulus of the composites. The values of *A* and *B* in case of composites are calculated from finite elements to be 15.5 mm and 32.5 mm and are found to be slightly different from same-material specimens. In order to determine values of *A* and *B* the loads on the specimen are calculated using finite elements. A similar approach as in case of same-material specimens is used. The equivalent loading points for *A* and *B* are found to be constant and are plotted against the ratio of the typical composite elastic moduli E_{11} and E_{22} in Fig. 2.6. (data from Daniel and Ishai, 2005)

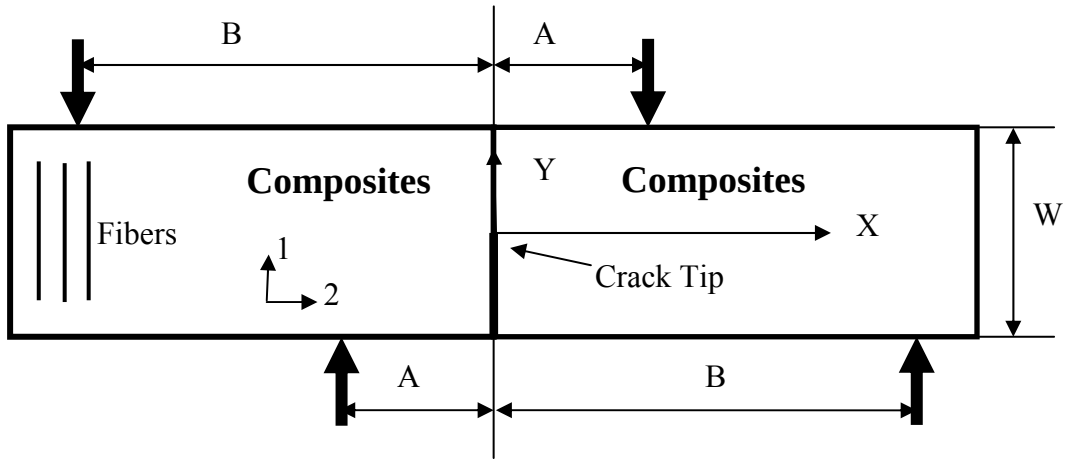

Fig. 2.5 Schematic diagram of a short-beam shear specimen for unidirectional composites materials

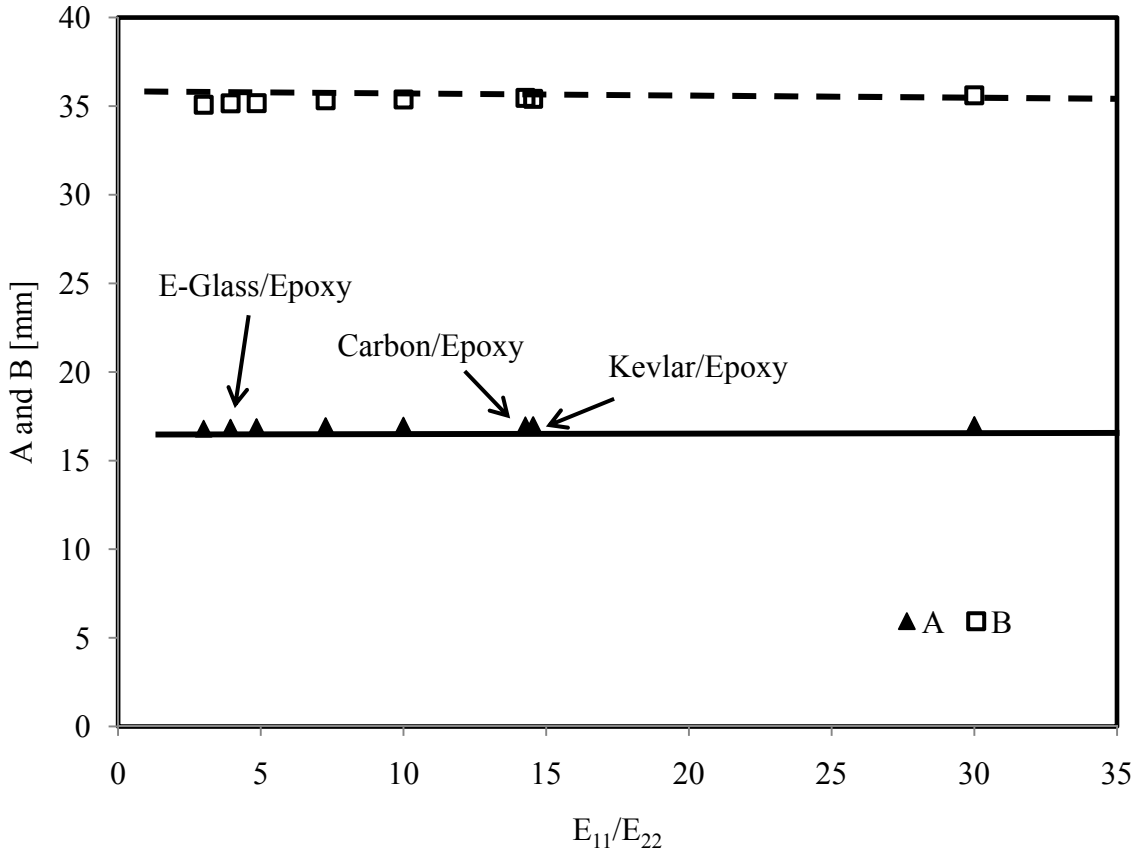

Fig. 2.6 Finite element analysis results showing very small variation in *A* and *B* with elastic modulus ratio for different types of orthotropic composite materials.

2.3 Experimental investigation

2.3.1 Specimen preparation and test procedure

This investigation includes two types of specimens: 1. short-beam shear fracture (SBSF) specimens with dimensions required for the Iosipescu fixture, and 2. four-point bending specimens with slightly larger dimensions. For the Iosipescu fixture, specimens were made of two individual halves of length 38.1 mm, width (W) of 19.1 mm and thickness of 5.5 mm. Specimens tested under four-point bending had individual half-length of 61 mm, width (W) of 30.5 mm and thickness of 5.5 mm. All specimens were made of polycarbonate and PMMA and were bonded at the interface using an adhesive to enable interfacial failure. The bonding surfaces of the individual halves were sand-blasted to improve the bonding quality. While Weldon-10 was used to provide strong bonding, Loctite 384 was used to provide weak bonding. These adhesives were specifically chosen such that their elastic modulus when cured was close to those of polycarbonate and PMMA (2-4 GPa). This was done to simplify the mechanics of the polymer/adhesive/polymer interface. Each specimen had an initial crack (a/W=0.5) which was made by covering one half of the adhesive using a thin tape. The adhesive was then applied to the other half and the specimen was bonded using a special fixture to guarantee dimensionality. The specimens were left to cure for a period of 24 hours to achieve the bonding strength.

The experimental set-up consisted of three parts including a mechanical system to load the specimens, an optical system to capture fringe patterns and an imaging set-up to record the images (Xu et al., 2004a). The fringes were solely used to observe the failure

process and to determine the crack path. The mechanical system consisted of a MTS 810 test machine and an Iosipescu fixture. Four-point bending fixture was used to apply load for the other type of specimens with an A of 20 mm and B of 40 mm (as shown in Fig. 2.1). Load was applied to the movable part of the Iosipescu fixture in the form of displacements at a rate of 1 mm/min until failure. About seven to ten specimens were tested in each case to ensure repeatability.

2.3.2 Experimental Results for Mode-II fracture toughness

Experimental results for short-beam shear fracture tests and four-point bending tests are presented in Table 2.1. Short-beam shear specimens showed two fracture modes: if the interfacial bonding was strong, the initial crack, although loaded in shear, kinks from the original crack path and forms a mode-I crack (its symmetrical stress field was verified by optical techniques). The other failure mode showed a pure mode-II crack that propagates along the interfacial bonding (a self-similar crack) when the interfacial bonding was weak. However, in case of the strongly bonded polycarbonate specimens, kinking starts away from the crack tip. The crack was observed (during the experiment by optical methods and after failure by observation of the failure surfaces) to originate as a mode II crack and then kink away as a mode I crack. Hence, it is concluded that the intrinsic mode II fracture toughness for polycarbonate specimens is obtained. In case of PMMA, the crack was observed to kink from the crack tip itself. So, a lower bound for the K_{IIC} value is obtained, and not the mode-II fracture toughness, as indicated in Table 2.1. All the four-point bend specimens showed a pure mode-II crack propagating along the interface without any kinking into the bulk material.

The values of K_{IIC} are seen to be equal or slightly more than the values of K_{IC} for the same material types obtained from our previous experimental research (Krishnan and Xu, 2011a). This indicates that there is less friction between the cracked faces obtained in our experiments. The difference in fracture toughness values between short-beam shear tests and four-point bending tests is about 20-25% for all cases. The error is seen to be consistent and can be attributed to size effect. A larger specimen size is required for 4-point bending than for short-beam shear. The short-beam shear approach uses the Iosipescu fixture and its dimensions are determined by the fixture. In case of four-point bending, we use a minimum size of the specimen which is permitted by the four-point loading fixture. Therefore, the two specimen sizes are different. By comparing our approach with four-point bending, we validate our new approach which is much simpler to implement and uses a simpler formula than four-point bending. The short-beam shear approach is also more practical to use in case of composite materials.

Table. 2.1 Experimental results for same-material specimens

		Short-Beam Shear		4-point bending		
Bonded materials	Bond	Crack init load (N)	K_{IIC} (MPa $m^{0.5}$)	Crack init load (N)	K_{IIC} (MPa $m^{0.5}$)	% Difference
Polycarbonate	Weak	417 ± 49	0.9481	1328± 229	0.7508	20
Polycarbonate	Strong	1002 ± 57	2.278	2991 ± 180	1.6911	25
PMMA	Weak	451 ± 100	1.0845	1641 ± 155	0.9278	14.5
PMMA	Strong	975 ± 81	≥2.3445	3118 ± 550	1.7629	24.8

2.3.3 Analysis on crack kinking during pure shear experiment

In general, an initial crack seeks the path of least resistance to propagate (Anderson, 2004). In the present case, a pure mode II crack is needed, rather than a kinked mode I crack. The angle of the crack kinking can be calculated theoretically (Erdogan and Sih, 1963; Williams and Ewing, 1972). The kinking angle has been calculated for a mixed mode case by Bhattacharjee and Knott (1995). A schematic diagram of crack kinking along with the conventions is shown in Fig. 2.7. The criterion for an initial crack to kink along an angle can be expressed as

$$\frac{\partial \sigma_{\theta\theta}}{\partial \theta} = 0 \quad , \quad \frac{\partial^2 \sigma_{\theta\theta}}{\partial \theta^2} < 0 \tag{2.10}$$

Where the shear stress is zero and the hoop stress is maximized. The hoop stress and shear stress close to a crack tip can be expressed in polar coordinates as (Anderson, 2004)

$$\sigma_{\theta\theta} = \frac{K_{II}}{\sqrt{2\pi r}}\left(-\frac{3}{4}\sin\left(\frac{\theta}{2}\right) - \frac{3}{4}\sin\left(\frac{3\theta}{2}\right)\right) \tag{2.11}$$

$$\tau_{r\theta} = \frac{K_{II}}{\sqrt{2\pi r}}\left(\frac{1}{4}\cos\left(\frac{\theta}{2}\right) + \frac{3}{4}\cos\left(\frac{3\theta}{2}\right)\right) \tag{2.12}$$

The condition in equation (2.10) is solved for θ and the predicted angle of the kink is calculated as 19.5^o from the x-axis. This is close to the angle of kink obtained experimentally from polycarbonate and PMMA. It should be noted that the kinking angle is independent of the material used if the T-stress is neglected. The effect of the T-stress before and after crack kinking has been reported by Li and Xu (2007). A typical strongly bonded polycarbonate specimen showing a kinking angle of about 25^o from the x-axis is presented in Fig. 2.8.

In order to predict which failure mode will occur at first, the energy release rates and fracture toughnesses of two failure modes should be compared (Hutchinson and Suo, 1992; Xu and Rosakis, 2003; Xu et al., 2003). The energy release rate of the initial crack is a function of the potential crack path or a function of θ. For the kinked mode-I crack, the energy release rate, $G(\theta=\theta_c)$ should exceed the mode-I fracture toughness of the polymer material Γ_{IC}^{PM}, i.e.,

$$\frac{G(\theta=\theta_c)}{\Gamma_{Ic}^{PM}} \geq 1 \tag{2.13}$$

Where the crack kinking angle θ_c is around 20^o from the x axis based on Erdogan and Sih (1963). For the pure mode-II crack initiation and propagation, the energy release rate, $G(\theta=90^o)$ should exceed the mode-II fracture toughness of the interface Γ_{IIC}^{IT}, i.e.,

$$\frac{G(\theta=90^o)}{\Gamma_{IIc}^{IT}} \geq 1 \tag{2.14}$$

So, the competition of the energy release rate and the fracture toughness leads to different failure modes. Here, if equation (2.13) is satisfied at first, a crack loaded in shear will kink as a mode-I crack. If equation (2.14) is satisfied at first, a crack loaded in shear will propagate as a mode-II crack along the interface.

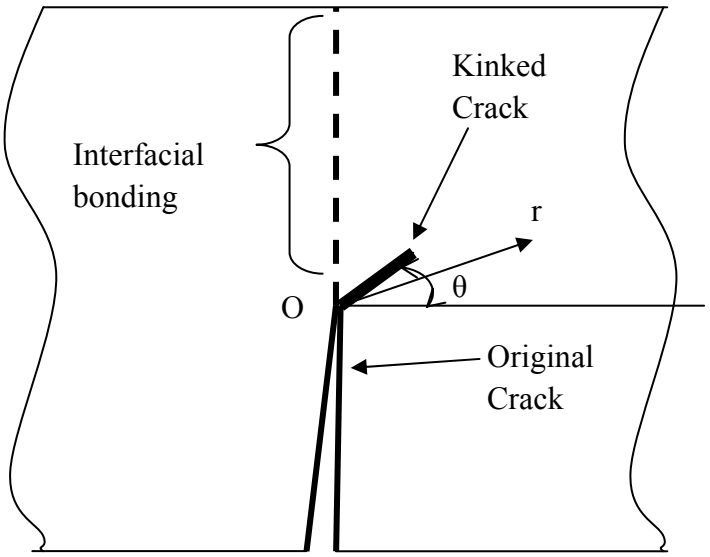

Fig. 2.7 Schematic diagram showing the crack kinking

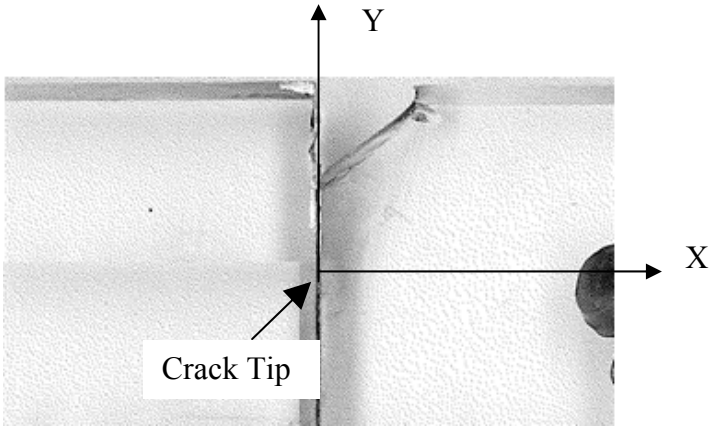

Fig. 2.8 Picture of a typical strongly bonded polycarbonate specimen showing crack kinking from the interface

2.4 Numerical Methods to validate mode-II fracture toughness

2.4.1 Finite element model to compare with formula for same-material specimens

A two-dimensional finite element analysis was conducted using Abaqus® 6.9.1. The mesh is progressively graded in order to reduce computational cost, and is refined

near the crack tip to best capture the stress singularity. Polycarbonate specimens with an elastic modulus of 2.4 GPa and a Poisson's ratio of 0.37 are chosen for the analysis. The dimensions of the model are the similar with the experimental specimens described earlier. The geometry of each individual part is symmetric while the loading on the material is anti-symmetric. The model is assumed to be monolithic with the zero thickness of the adhesive layer.

The loading is applied in the form of loading block on the specimen edges similar to what is observed in reality. In order to incorporate a realistic simulation of the loads on the specimen an iterative procedure is adopted (Xu et al., 2004b; Krishnan and Xu, 2010). The loads in the form of displacements are applied to the movable part of the specimen while the other part is held fixed. After each analysis the reaction forces on the loading edges are checked to see if they are in compression or not, because in experiments, only compressive loading is observed. The constraints are removed from those nodes which showed tensile reaction forces and the analysis is repeated until convergence. The stress intensity factors, K_I and K_{II} are calculated from the finite element analysis and are compared with the results from equation (2.6) to determine the constant $F_{II}^{SBSF}(a/W)$. The results for different values of a/W are presented in Table 2.2. From the analysis, we find K_I is negligibly small in comparison with K_{II} as expected from the theoretical results presented earlier. The values of K_{II} obtained from the numerical analysis are used to determine the value of the constant F_{II}^{SBSF} which is also indicated in Table 2.2. The variation of F_{II}^{SBSF} as a function of a/W is presented in Fig. 2.9 for four-point bending (Suresh et al., 1990) and for short-beam shear.

Table 2.2. Calculation of F_{II}^{SBS} for same-material polycarbonate specimen at different a/W ratios.

a/W	Finite Element Analysis		Formula	
	Load (N)	K_{II} (MPa $m^{0.5}$)	K_{II}/F_{II}^{SBSF}	F_{II}^{SBSF}
0.3	252	0.3067	0.4160	0.7372
0.4	250	0.4332	0.4119	1.0517
0.5	245	0.5581	0.4046	1.3790
0.6	239	0.6735	0.3941	1.7082
0.7	230	0.7874	0.3787	2.0792

A snapshot of the deformed mesh near the crack tip at failure load is presented in Fig. 2.10. It can be seen that there is no crack surface separation (opening mode-I), and only sliding along the crack face (shear mode-II). This confirms that there is no mode I component from our finite element analysis. The shear and normal stresses along the interface at a failure load of 1000 N are plotted in Fig. 2.11. The graph demonstrates the singularity of the stresses at the crack tip. Also, there is no contact between the crack lips indicating that there is little friction involved during experiments. Fig. 2.12 shows a comparison of shear stresses along the crack faces for different loading cases. These values are seen to be close to zero even at higher loads (beyond failure loads) demonstrating the absence of friction between the crack faces.

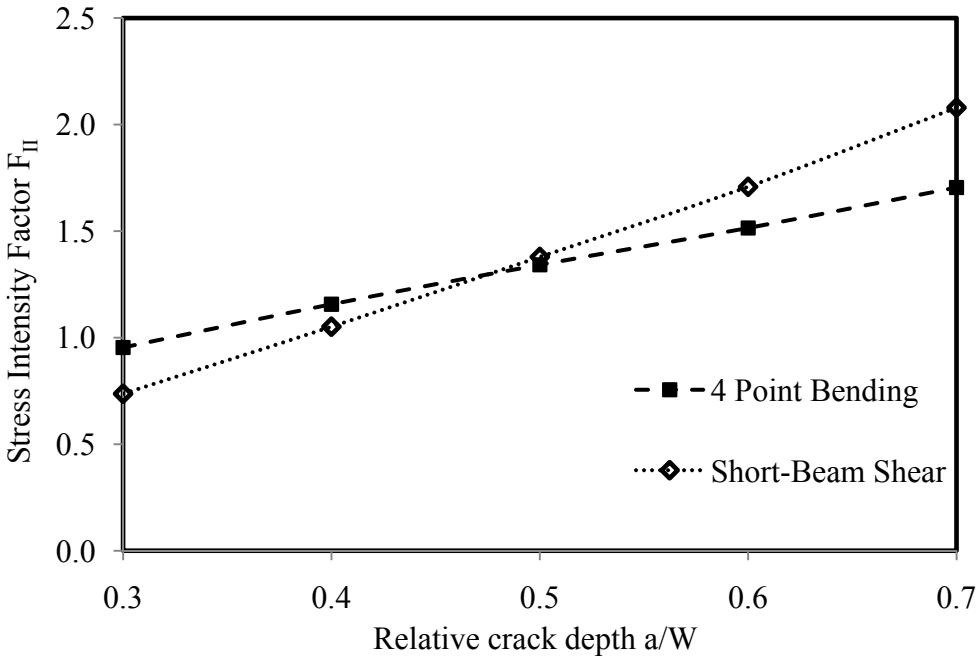

Fig. 2.9 Variation of dimensionless stress intensity factor F_{II} with relative crack depth for 4-point bending (Suresh et al., 1990) and short-beam shear.

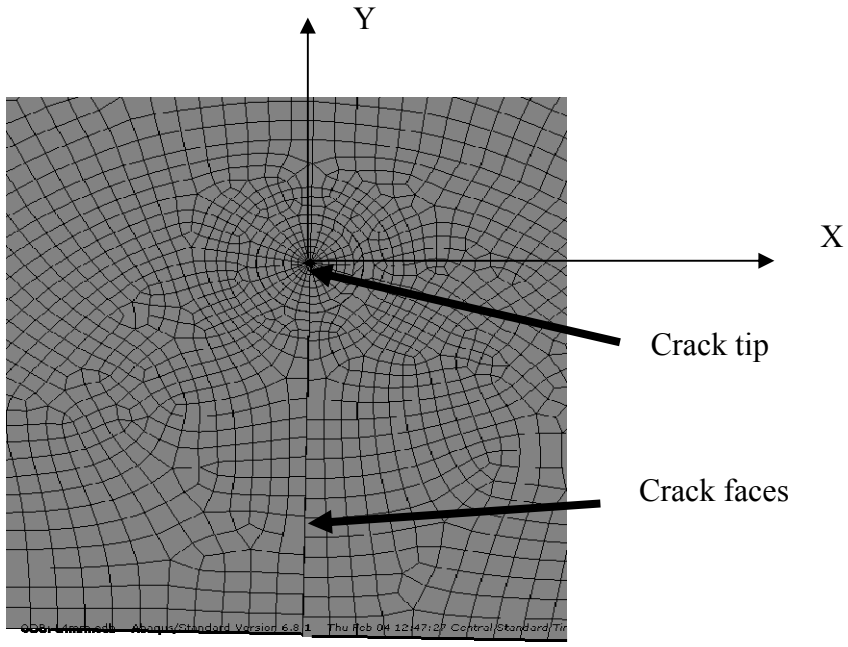

Fig. 2.10 Snapshot of deformed mesh (near the crack tip) at failure load. This mesh is used for modeling short-beam shear specimen.

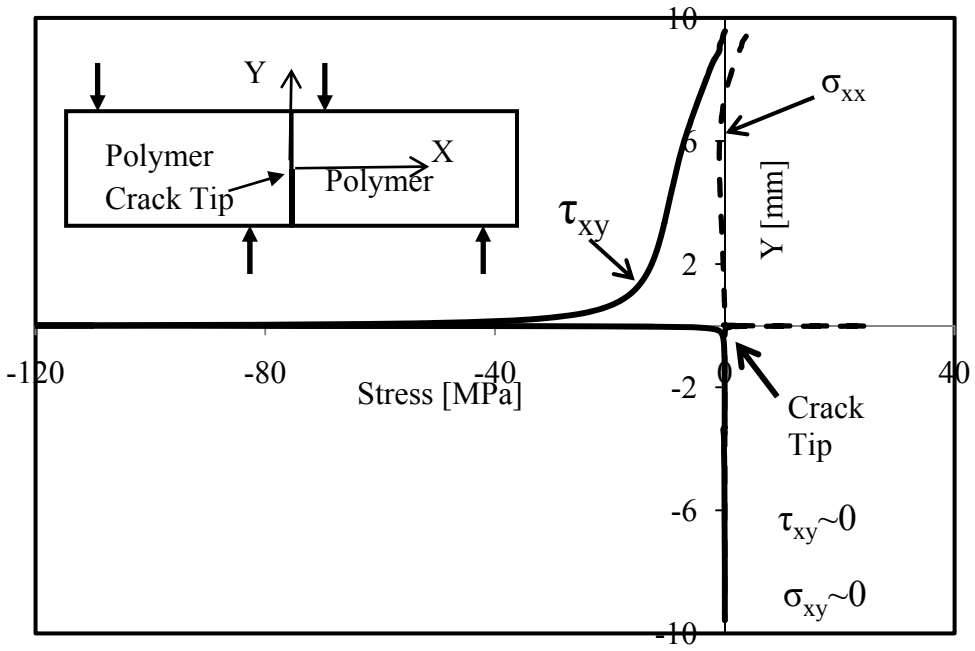

Fig. 2.11 Variation of shear stress and normal stress along the interface for polycarbonate same-material bonding at a failure load of 1000 N.

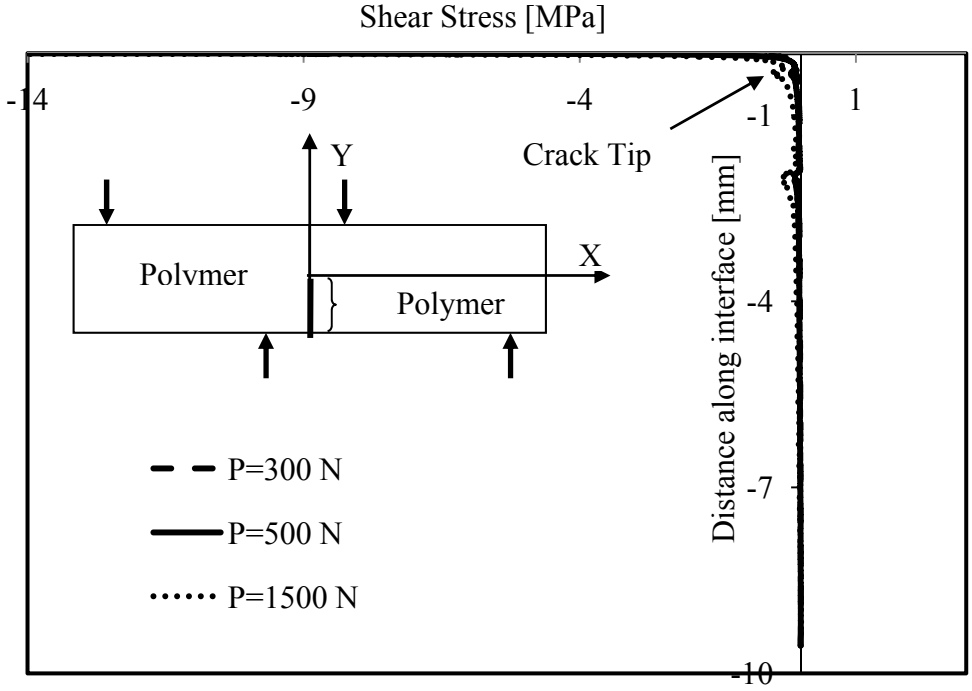

Fig. 2.12 Variation of shear stresses along the interface for polycarbonate same-material bonding with increase in applied loading.

2.4.2 Numerical modeling for composites

A similar model as described in above is made for composite materials with fiber direction along the y-direction as shown in Fig. 2.5. This type of unidirectional composite materials ensures that the mode-II crack will not kink and will propagate along the fiber-matrix interface due to strong constraint of the fiber. Three kinds of typical composite material data are chosen from Daniel and Ishai (2005) to conduct the numerical analysis (Table 2.3).

However, in case of orthotropic unidirectional composite materials, we do not have the graph of F_{II} which has been provided for same-material specimens by Suresh et al. (1990) and for bi-material specimens by O'Dowd et al. (1992). Hence, the plot of F_{II} as a function of a/W is calculated for three different types of composite materials, viz. E-Glass/Epoxy (55 % volume percent of fibers, unidirectional GFRP), Kevlar 49/Epoxy (60% volume percent of fibers, unidirectional KFRP) and AS4/3501-6 Carbon/Epoxy (63% volume percent of fibers, unidirectional CFRP). The plot of F_{II} as a function of a/W is presented in Fig. 2.13. It is seen that this plot is almost constant for these three types of typical composites. While calculating the mode II stress intensity factors for composites, this chart becomes necessary to use the current approach and is complementary to the one presented in Suresh et al. (1990). Also, the numerically calculated values of K_I, K_{II} and F_{II} at different values of a/W ratios are presented in Table 2.5 for the three typical composite types chosen. The ratio of K_I/K_{II} remains negligibly small indicating that the crack is indeed a pure mode II crack in unidirectional composites. The applied loads on each composite specimen (corresponding to a fixed applied displacement of 0.5 mm) are also presented in Table 2.4. The different types of composites take different loads (in

spite of a fixed applied displacement) due to their different elastic properties. However, the dimensionless stress intensity factor, F_{II}, remains very similar for the different kinds of composites.

Table 2.3 Properties for three typical composites (Daniel and Ishai, 2005)

Materials	Fiber volume percent (%)	E_{11} (Gpa)	E_{22} (Gpa)	G_{12} (Gpa)	G_{23} (Gpa)	ν_{12}	ν_{23}
Carbon/Epoxy	63	147	10.3	7	3.7	0.27	0.54
E-Glass/Epoxy	55	41	10.4	4.3	3.5	0.28	0.5
Kevlar/Epoxy	60	80	5.5	2.2	1.8	0.34	0.4

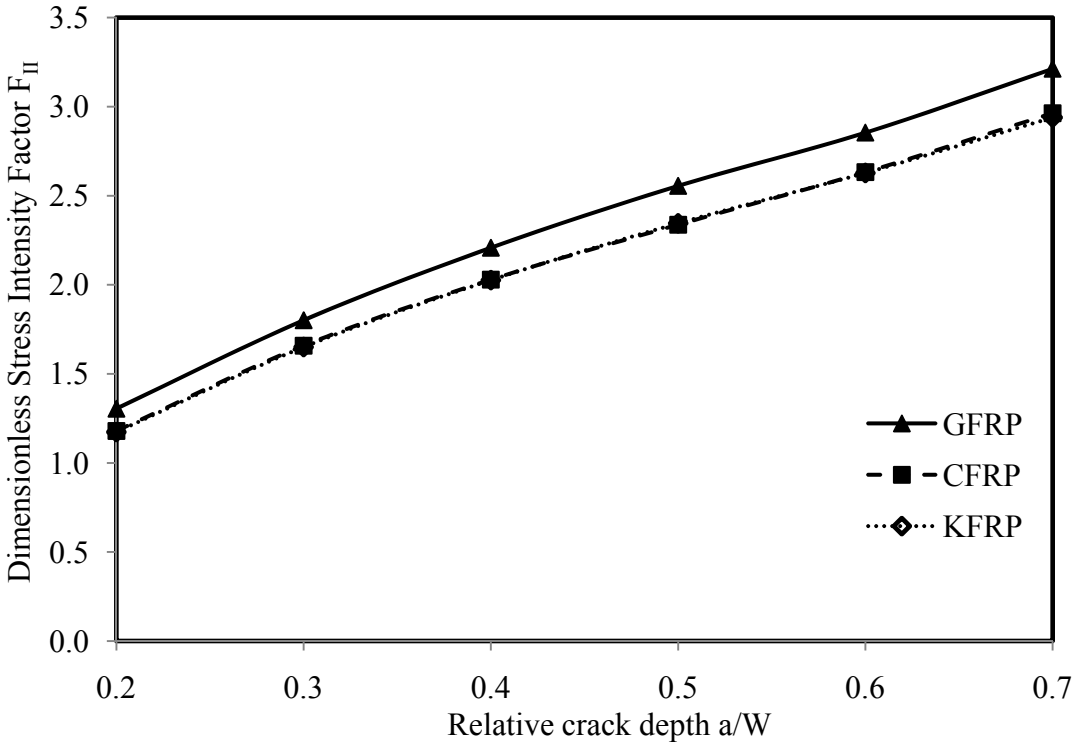

Fig. 2.13 Variation of dimensionless stress intensity factor F_{II} with relative crack depth for different types of composites.

Table 2.4 Variation of F_{II} with a/W for different types of composites. K_I and K_{II} are expressed in MPa $m^{1/2}$

CFRP

a/W	Load (N)	K_I (Mpa $m^{1/2}$)	K_{II} (Mpa $m^{1/2}$)	K_{II}/K_I	F_{II}
0.2	1009	0.0124	1.2412	0.0099	1.1796
0.3	1008	0.0090	2.1345	0.0042	1.6580
0.4	1004	0.0026	3.0042	0.0009	2.0289
0.5	1001	0.0006	3.8580	0.0001	2.3375
0.6	991	0.0083	4.7118	0.0018	2.6323
0.7	979	0.0146	5.6605	0.0026	2.9637

GFRP

a/W	Load (N)	K_I (Mpa $m^{1/2}$)	K_{II} (Mpa $m^{1/2}$)	K_{II}/K_I	F_{II}
0.2	709	0.0405	0.9645	0.0419	1.3045
0.3	708	0.0281	1.6286	0.0173	1.8010
0.4	704	0.0072	2.2927	0.0031	2.2083
0.5	698	0.0095	2.9410	0.0032	2.5554
0.6	687	0.0263	3.5418	0.0075	2.8543
0.7	671	0.0361	4.2058	0.0086	3.2128

KFRP

a/W	Load (N)	K_I (Mpa $m^{1/2}$)	K_{II} (Mpa $m^{1/2}$)	K_{II}/K_I	F_{II}
0.2	420	0.0058	0.5139	0.0113	1.1733
0.3	420	0.0039	0.8854	0.0044	1.6506
0.4	418	0.0006	1.2491	0.0005	2.0263
0.5	417	0.0004	1.6128	0.0003	2.3457
0.6	413	0.0043	1.9606	0.0022	2.6283
0.7	408	0.0063	2.3401	0.0027	2.9399

2.4.3 Cohesive element simulation of shear fracture

In order to simulate the experimental load-displacement curves and the failure load, a cohesive element analysis is employed. Cohesive elements are exclusively used along the bonded interface in order to model the failure process, mainly mode-I or mixed-mode cracks in the previous efforts. Therefore, our modeling is probably among very few efforts to simulate the mode-II crack. Cohesive elements with zero thickness are used in the model. A bi-linear cohesive law is considered for this case and a representative law for strongly bonded polycarbonate is shown in Fig. 2.14. Such types of cohesive laws have been used successfully in the past to model mixed mode failure in brittle materials (Camacho and Ortiz, 1996; Ruiz et al., 2001). The four types of specimens in Table 2.1 are modeled using a similar bilinear cohesive law but with different values of constants (shown in Fig. 2.14). The value of fracture toughness, G_{IIC}, obtained from the current experimental results (Table 2.1) is used here and equals the total area enclosed by the cohesive law. The elastic modulus of the bulk material is used as the slope of the initial linear part of the traction separation law. The maximum value of traction (τ) is obtained from our previous measurements for interfacial shear strengths of bonded polycarbonate systems (Krishnan and Xu, 2011a). The critical opening displacement (δ_c) can then be calculated from these known values. The finite element model used is similar to the one described in the previous sections except in the inclusion of the cohesive elements. Loads are then applied to the finite element model as described previously. The simulated load-displacement curves are plotted along with the experimental load-displacement curves in Fig. 2.15. Three different experimental curves are shown to depict the variation in the experiments. The cohesive element model is seen to capture the initial slope of the

experimental load-displacement curves. There is only a reasonable amount of error for the value of the final failure load as shown by the cohesive element model. A similar analysis, albeit with a different cohesive law, is carried out for weakly bonded polycarbonate specimens and the corresponding results are shown in Fig. 2.16. Different values of fracture toughness and maximum traction are used in this case and these data were from our previous measurement for the same material system. This model predicts the crack initiation load and failure displacement with a reasonable amount of error. The graphs in Figs. 2.15 and 2.16 are plotted on the same scale to allow for a fair comparison between the crack initiation loading of the same specimens with strong and the weak bonds.

The load-displacement curves obtained from the proposed SBSF approach show a sudden and clear drop as seen in Figs. 2.15 and 2.16. The crack initiation and the final failure loads almost coincide. This is very accurate in finding the crack initiation load and is a major advantage of our new SBSF approach. For other methods involving thin composite beam bending such as the end-notched flexure test, the exact crack initiation load was hard to record since the beam compliance change involving a very short crack initiation/propagation was quite small (Xu and Kou, 1994). This is a major reason for overestimation of the mode II fracture toughness of composite materials of current approaches. Previous approaches cannot get a clear estimate of when the beam compliance changes clearly, and hence the load recorded will be much higher than the actual crack initiation load. However, our approach gets the exact crack initiation load and hence a more accurate value of fracture toughness. Future work will involve extending this approach to measure the fracture toughness of unidirectional composites.

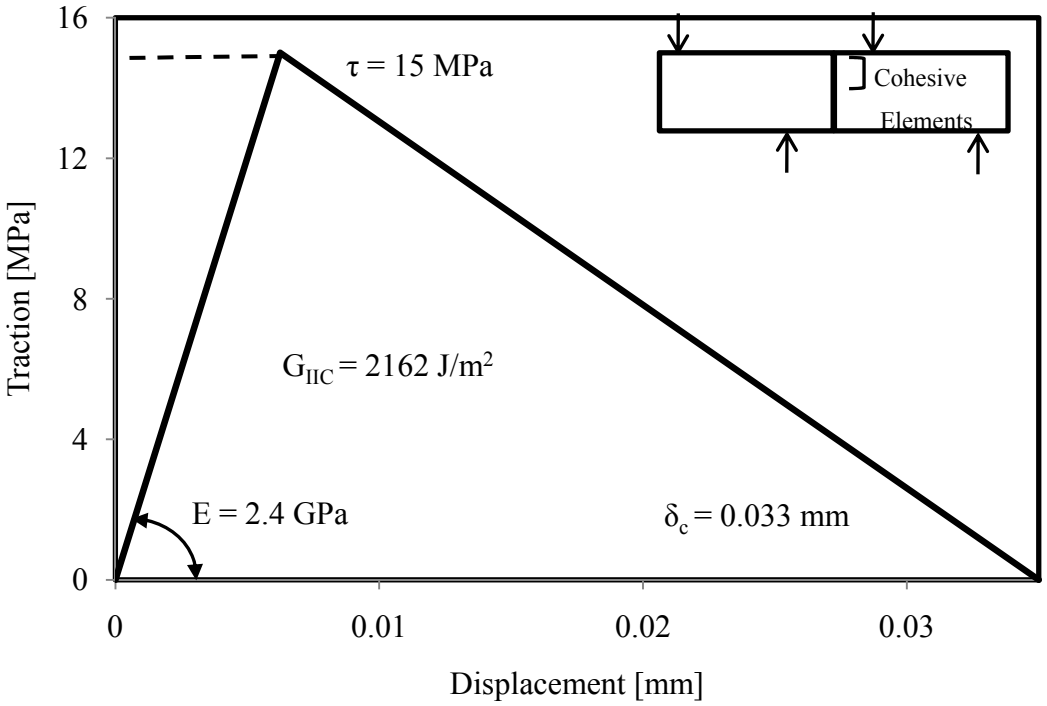

Fig. 2.14 Traction-Separation law used for strongly bonded Polycarbonate

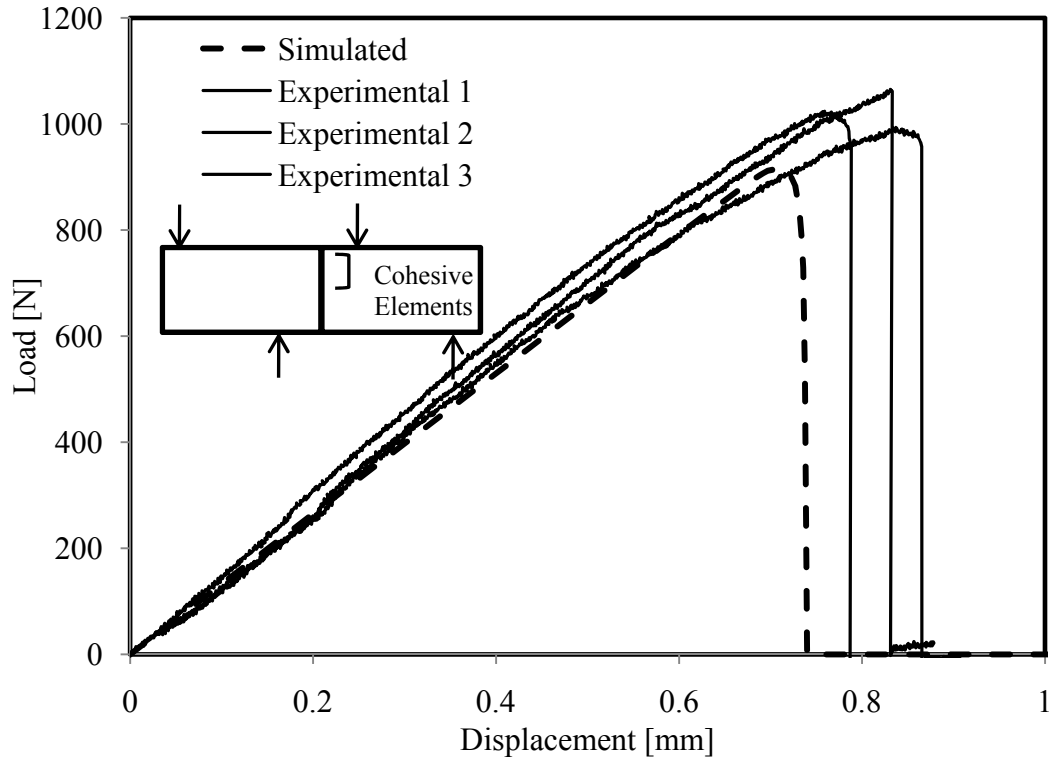

Fig. 2.15 Simulated and experimental load-displacement graphs for strongly bonded polycarbonate systems.

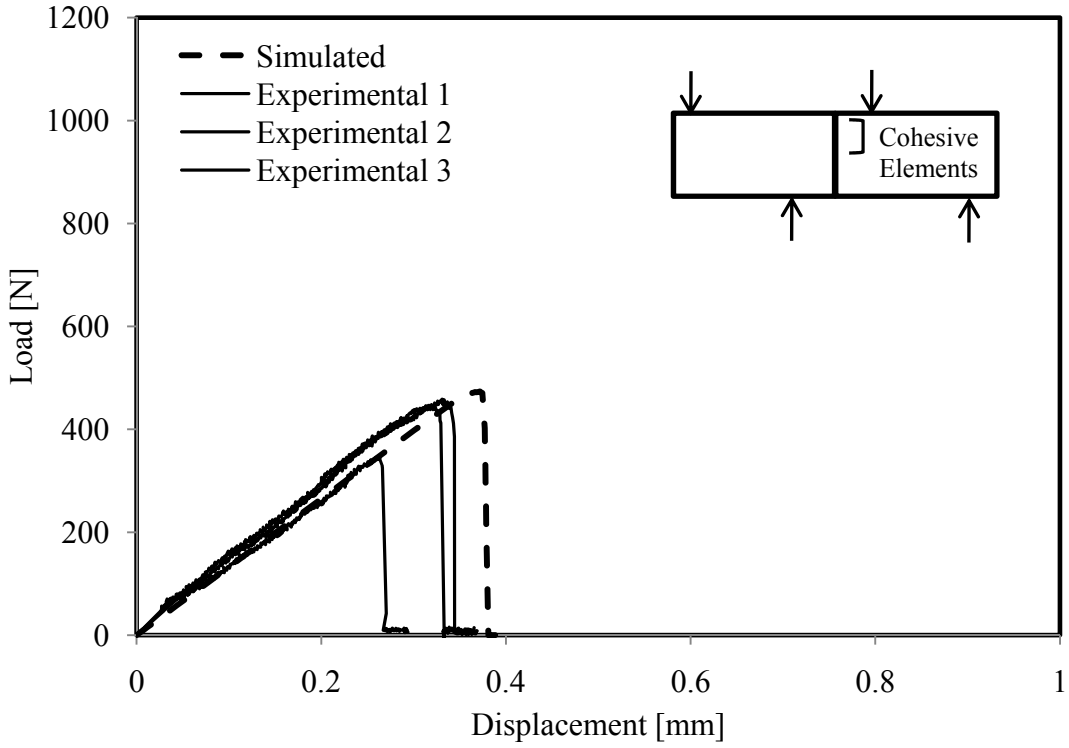

Fig. 2.16 Simulated and experimental load-displacement graphs for weakly bonded polycarbonate systems.

2.5 Measurement of Mode-I Fracture Toughness

2.5.1 Principles on fracture toughness measurements

In addition to measuring mode-II fracture toughness, this chapter describes the measurement of mode-I fracture toughness for a variety of bonded polymers. These data are included for the sake of completeness. Edge-notched fracture specimens were used to measure the mode I fracture toughness. The specimens were designed and tested to the following dimensions: specimen width W=38 mm, specimen thickness B=5.4 mm and initial crack length a=19 mm. All specimens had an initial crack with a/W =0.5 made before bonding by using scotch tape. All of the fracture specimens were tested in three-

point bending (Suresh et al., 1990). The length of the initial crack in a bi-material specimen in such a case would have to be chosen carefully to enable fracture in a single mode (mode I). The mode I fracture toughness K_{IC} for same-material joints was calculated using equation (2.15) (Anderson, 2004).

$$K_{IC} = \left(\frac{P_Q S}{BW^{3/2}} \right) f(x) \quad 0 < x = a/W < 1$$
$$f(x) = \frac{3}{2}\sqrt{x}\frac{[1.99 - x(1-x)(2.15 - 3.93x + 2.7x^2)]}{(1+2x)(1-x)^{3/2}} \tag{2.15}$$

where P_Q is the maximum load from the load-displacement plot, S is the support span, f(x) accounts for the correction due to the specimen geometry. In case of bi-materials, the calculation of fracture toughness becomes very different. First, the asymptotic stress field of an interfacial crack in a bi-material specimen, σ_{ij} can be expressed as (Rice, 1988)

$$\sigma_{ij} = \frac{1}{\sqrt{2\pi r}}[\mathrm{Re}\{K r^{i\varepsilon}\}\sigma_{ij}^{-I}(\theta;\varepsilon) + \mathrm{Im}\{K r^{i\varepsilon}\}\sigma_{ij}^{-II}(\theta;\varepsilon)] \tag{2.16}$$

where $K=K_1+iK_2$ is the complex stress intensity factor, σ_{ij}^{I} and σ_{ij}^{II} are the stresses in mode I and mode II, and ε is a function of Dundur's parameters β and is given by

$$\varepsilon = \frac{1}{2\pi}\ln\{\frac{1-\beta}{1+\beta}\} \tag{2.17}$$

The elastic properties of aluminum include a Young's modulus of E=71 Gpa, a shear modulus μ=26.7 Gpa and a Poisson's ratio of ν=0.33. Corresponding elastic properties for polycarbonate used in this calculation are E=2.4 Gpa, μ=0.9 Gpa, ν=0.34. Hence, the two Dundur's parameters for the material combination of polycarbonate and aluminum are calculated as α=0.93 and β=0.31. It should be noted here that PMMA, although

chemically different, has similar elastic properties as polycarbonate. Therefore, the Dundur's parameters for PMMA/aluminum are also the same as in above. A schematic of our bi-material specimen used to obtain the fracture toughness value is illustrated in Fig. 2.17.

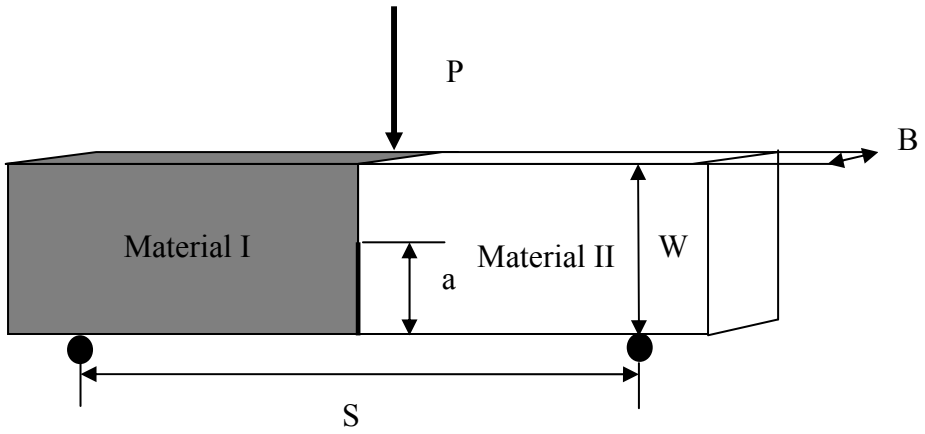

Figure 2.17 Bi-material specimen for mode-I fracture toughness measurement (a/W=0.5)

A general form for the stress intensity factor for a bi-material specimen is given as (O'Dowd et al., 1992)

$$K = YT\sqrt{a}\,a^{-i\varepsilon}e^{i\psi} \tag{2.18}$$

where $T=P(3B/W^2)$, Y and ψ are calibrating factors which depend on *a/W*, *B/W* and the Dundur's parameters. Then the stress intensity factor in mode I can be expressed as

$$K_I = \mathrm{Re}\{Ka^{i\varepsilon}\} \tag{2.19}$$

Using equations (2.18) and (2.19), the bi-material fracture toughness K_{IC} is calculated as

$$K_{IC} = \frac{3P_Q S}{BW^2} Y\sqrt{a}\cos(\psi) \tag{2.20}$$

Here, Y=2.4 and ψ=7.8 degrees, the fitting parameters are obtained from (O'Dowd et al., 1992) for β=α/3 as is in our case.

2.5.2 Results of Mode-I fracture toughness experiments

The material systems and their measured K_{IC} values are presented in Table 2.5. During experiments, the load required to completely break the specimen under three-point bending was recorded and the value of K_{IC} was calculated using equation (2.15) for same-material joints and using equation (2.20) for bi-material systems. It was observed that Weldon-10 bonding shows a higher value of K_{IC} than Loctite 384 bonding for most material systems. Only polycarbonate/384/aluminum shows a decrease of 10% in fracture toughness from the corresponding weak bond. Generally bi-material fracture specimens show a small difference of K_{IC} values between the two types of strong and weak adhesives. Similar to its tensile and shear bonding strengths, PMMA shows a better bonding with the two types of adhesives and hence a greater value of fracture toughness is obtained for bonded PMMA specimens. Bi-material specimens consistently show a lower value of mode I fracture toughness than same-material specimens.

Homalite/polyester/Homalite material systems show lower fracture toughness than other strong adhesive systems used in conjunction with Homalite: Weldon-10 and Loctite 330. It should be noted that polyester provides the highest tensile and shear bonding strengths. Therefore, strength and fracture toughness are very different parameters and should be measured for every new material system. The fracture

toughnesses of other adhesive systems show a trend similar to the bonding strengths of the same- material joints, i.e., bonding strengths increase with fracture toughnesses from weak bonding to strong bonding.

Table 2.5. Measured Mode-I fracture toughness for same and bi-material joints

Material/adhesive/material	Mean K_{IC} (MPa $m^{1/2}$)	Difference (%)
	Same-Material Bond	
Polycarbonate/384/Polycarbonate	0.64	+36 %
Polycarbonate/W10/Polycarbonate	0.86	
PMMA/384/PMMA	0.71	+147 %
PMMA/W10/PMMA	1.74	
	Bi-Material Bond	
Polycarbonate/384/Aluminum	0.1	-10 %
Polycarbonate/W10/Aluminum	0.09	
PMMA/384/Aluminum	0.12	+17 %
PMMA/W10/Aluminum	0.14	

2.6 Conclusions

The mode II fracture toughness of materials with preferred interfaces can be measured by using the proposed short-beam shear approach as has been documented in Krishnan and Xu (2011b). The amount of friction between the cracked surfaces behind the crack tip is negligible, and hence an intrinsic value of the pure mode-II fracture toughness is obtained. Another feature of our new approach is the accurate measurement of crack initiation load which is not available in previous techniques. The current method is justified by the use of numerical techniques (finite element analysis and cohesive

element analysis), and comparison with experimental data. This method can also be extended to unidirectional composite materials. Additionally, the mode-I fracture toughness for bonded same-material and bi-material joints is presented for the sake of completeness.

CHAPTER III

STUDY OF NOTCH AND INTERFACE INTERACTIONS IN BONDED MATERIALS

3.1 Introduction

Failure prediction has often either involved a strength approach or a fracture toughness approach. The stress intensity factor approach based on linear elastic fracture mechanics has been popularly used in case of cracks starting with the seminal paper by Williams (1952). A universal stress singularity with an order of λ-1 is shown to exist in the region around a sharp notch. However, proposed failure criterions like the Griffith criterion (Griffith, 1921) and the Irwin modification (1957) can be used only for sharp cracks and not in case of sharp notches. Qian and Fatemi (1996) present a literature survey of failure criterions in case of mixed mode fatigue cracks. The maximum tangential stress criterion proposed by Erdogan and Sih (1963) is one of the widely used criterions for mixed mode crack growth. Other failure criterions used to predict crack growth include the maximum strain energy criterion (Sih, 1974), J-criterion (Hellen and Blackburn, 1975), dilatational strain energy density criterion (Theocaris and Andrianopoulos, 1982) and many others. However, a crack is indeed only a special case of a notch with a notch opening angle of 0^o. Notches and sharp re-entrant corners are formed in many real-life situations. Experiments on composite laminates as described in this dissertation in Chapter 4 have indicated that impact-induced delamination will propagate under compressive loading. This delamination front is a notch and not a mathematically sharp crack (as shown in Fig. 3.1). Williams (1952) describes the

problem of fracture for a notch with an opening angle of β. Yet, fracture from cracks has received more attention than fracture from notches. Fracture in brittle materials with V-notches has been investigated by some researchers including Dunn et al. (1997a, 1997b), Leguillon (2002), Leguillon and Yosibash (2003), Seweryn (2004), Yosibash et al. (2004, 2006) and Priel et al. (2007). Inspite of the several experimental and numerical investigations involving notches, there are no reliable failure criterions which have been widely accepted. More importantly, only few experimental results are available to verify newer failure criterions for crack initiation from notches.

The problem of crack onset at a notched interface is still an open problem and few criterions have been proposed (Dunn et al., 1997a, 1997b; Leguillon, 2002) to address this issue. A novel approach involving a combination of the strength and the toughness conditions has been proposed by Leguillon (2002). Leguillon (2002) further argues that both (and neither one not the other) of the energy and strength criterions are essential for prediction of crack initiation from a notch tip. Yosibash et al. (2006) discuss a failure criterion for predicting failure in brittle materials with mixed-mode loading. Carpinteri (1987) presents a detailed set of experiments on determining critical stress intensity factors at a re-entrant sharp corner using PMMA beams of varying notch angles and sizes. Dunn et al. (1997b) use a critical stress intensity approach to determine the stress state at the notch tip using a combined experimental and numerical approach. However, existing experimental research has not considered the presence of an interface combined with a notch. The inclusion of a weak bonded interface in brittle materials forces the crack to initiate along the interface direction instead of progressing along the bulk

material. Developing a generalized notch-interface failure criterion is very important for the field of fracture mechanics from a fundamental standpoint.

This chapter presents an experimental approach to measure the crack initiation load in notched brittle-material specimens with an interface. The artificially induced interface is weaker than the bulk material and leads to crack initiation along the interface. This leads to the two interesting problems of crack initiation and crack propagation. The experimental data from crack initiation is used to verify the fracture criterion proposed by Leguillon (2002). The specimens are designed such that there is mode mixity at the crack tip. In the current investigation, a specimen as shown in Fig. 3.2 is designed and tested to determine the crack initiation load. This is used to compare with theoretical predictions developed by Leguillon (2002). The angle of the notch (β), the loading point (S), the interfacial adhesive and the materials (polycarbonate and PMMA) are used as variables to understand their effect on the crack initiation load. Further, the experiments are designed to include the effect of stiffness mismatch by considering bi-material specimens. The experimental results in this chapter present a rich amount of data including load data, experimental load-displacement curves, pictures of fringe patterns, crack path data and crack path pictures which will be used as benchmark for future numerical simulation tools.

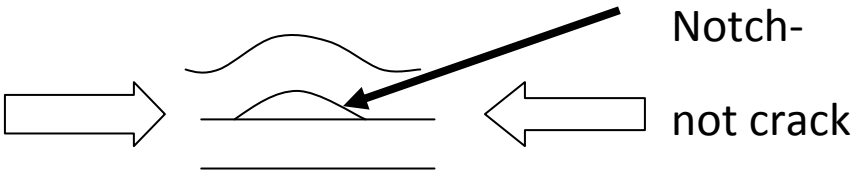

Fig. 3.1 Impact-induced delamination will propagate under compression load during CAI experiments. The delamination front is a notch, not a mathematically sharp crack

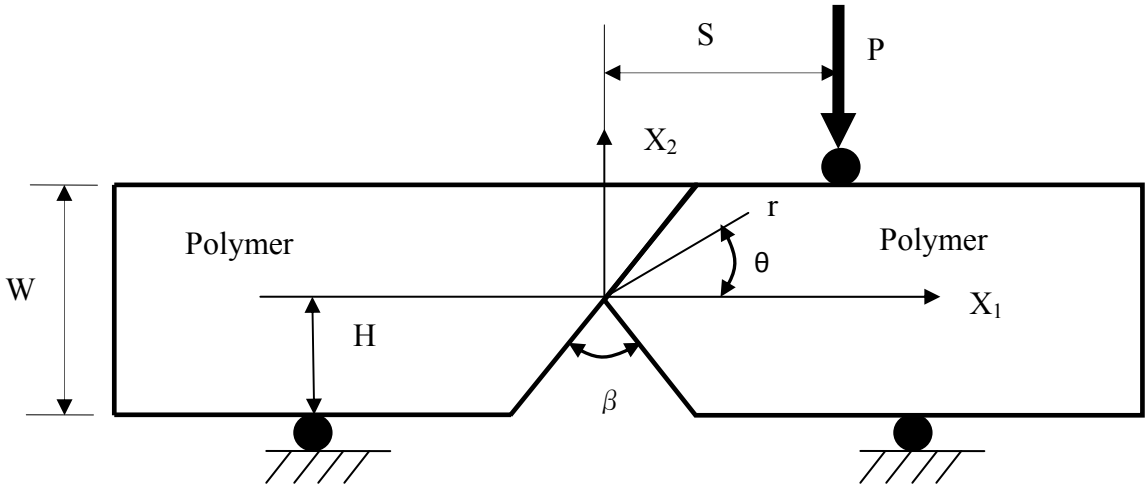

Fig. 3.2 Schematic diagram representing same-material notch-interface specimens

3.2 Theoretical background

In case of same-material geometries with a notch but without any interface, a crack will initiate from the notch tip and propagate along the centre line of the specimen if the specimen is subject to symmetrical loading. Theoretical results from Leguillon (2002) indicate that there should be an exponential increase in the value of crack initiation load with increase in the notch angle based on the author's novel crack initiation criterion. A generalized stress intensity factor (GSIF) approach is used since the

stress at the notch tip is singular. At the crack initiation, the GSIF will exceed a critical material parameter which can be represented by including both the strength and the fracture toughness:

$$k \geq k_c^L = \left(\frac{G_{Ic}}{A} \right)^{1-\lambda} \sigma_c^{2\lambda-1} \tag{3.1}$$

where G_{IC} is the material mode-I fracture energy; A is a function of the notch angle and the crack direction, σ_c is the material tensile strength, and λ-1 is the stress singularity order of the notch. For a crack (notch angle is zero): λ=0.5, this criterion becomes a typical fracture mechanics criterion proposed by Irwin (Anderson, 2004). If the notch angle is 180 degrees (a straight bar): λ=1.0, then this criterion becomes a typical tensile strength criterion in mechanics of materials. This criterion showed very good agreements with experimental results (Leguillon, 2002).

However, the presence of an interface makes the problem complicated. The criterion shown by equation (3.1) is modified to explain the crack initiation in such a case. Interfaces are always present in composite materials and determining their properties is of much importance in determining the properties of the structure (Krishnan and Xu, 2010). In the current investigation, the interaction between the interface (as shown in Fig. 3.2) and the notch can make the problem different (from a notch alone) in the following ways: The interface being connected with the notch tip can cause a crack to initiate from the interface rather than the from the bulk materials. Also, the location of the loading point is made a variable and hence the stress field at the notch tip will change from the symmetrical stress state to unsymmetrical stress states. Finally, a mixed-mode crack, rather than a pure mode-I crack, will initiate from the interface.

The new factors described as in above necessitate a new failure criterion. In order to predict the initiation of the interfacial crack, a more general stress state with normal and shear stresses acting along the interface should be used. We start from a basic William's expansion (1952) for the elastic displacement (U) and stress (σ) field at the notch tip which can be expressed in terms of polar coordinates as

$$\begin{aligned} U(r,\theta) &= R + k_1 r^{\lambda_1} u(\theta) + \ldots \\ \sigma(r,\theta) &= k_1 r^{\lambda_1 - 1} s(\theta) + \ldots \end{aligned} \tag{3.2}$$

Here u(θ) and s(θ) are angular shape functions for the displacement and stress fields respectively. Also, the exponent λ_1 is the order of the notch tip singularity and must be positive for a finite energy solution. The parameter k_1 is the generalized stress intensity factor (GSIF) and is proportional to the applied load. The exponent λ_1 can be real or complex and can also be simple or multiple. Leguillon's criterion for the case of simple real eigenvalue with $1/2 \le \lambda_1 < 1 \le \lambda_2$ can be expressed as

$$k_1 \ge k_c = \left(\frac{G_c}{A(\phi)} \right)^{1-\lambda_1} \left(\frac{\sigma_c}{s(\phi)} \right)^{2\lambda_1 - 1} \tag{3.3}$$

For the cases of two real eigenvalues with $1/2 \le \lambda_1 \le \lambda_2 < 1$, Leguillon's criterion can be extended as

$$k_1 > k_c = \left(\frac{G_c}{A_{11}(\phi) + 2m(l_c)A_{12}(\phi) + m(l_c)^2 A_{22}(\phi)} \right)^{1-\lambda_1} \left(\frac{\sigma_c}{s_1(\phi) + m(l_c)s_2(\phi)} \right)^{2\lambda_1 - 1} \tag{3.4}$$

where the critical length l_c is obtained by solving this equation

$$l_c = \frac{G_c}{A_{11}(\phi) + 2m(l_c)A_{12}(\phi) + m(l_c)^2 A_{22}(\phi)} \left(\frac{s_1(\phi) + m(l_c)s_2(\phi)}{\sigma_c} \right)^2 \tag{3.5a}$$

$$\text{with } m(r) = \frac{k_2}{k_1} r^{\lambda_2 - \lambda_1} \tag{3.5b}$$

The critical length l_c gives an estimate of the distance from the notch tip where the stresses can be compared as the notch tip stresses tend to be singular. For the case of complex exponent of $\lambda \pm i\varepsilon$ with complex GSIF $k = k_1 + ik_2$, Leguillon's criterion is extended as

$$|k| > k_c = \left(\frac{G_c}{2\,\mathrm{Re}(B(\phi) + m(l_c)B'(\phi))} \right)^{1-\lambda} \left(\frac{\sigma_c}{|s_1(\phi) + m(l_c)s_2(\phi)|} \right)^{2\lambda - 1} \tag{3.6}$$

And the critical length l_c can be obtained by solving this equation

$$l_c = \frac{G_c}{2\,\mathrm{Re}(B(\phi) + m(l_c)B'(\phi))} \left(\frac{|s_1(\phi) + m(l_c)s_2(\phi)|}{\sigma_c} \right)^2 \tag{3.7a}$$

$$\text{with } m'(r) = \frac{\overline{K}}{K} r^{-2i\varepsilon} \tag{3.7b}$$

The co-efficients A, A_{11}, A_{12}, A_{22}, B and B' strongly depend on the cracking direction ϕ (which can be along the interface or in the bulk material). They can be determined from the "inner problem" (Yosibash et al., 2006) for all loading cases.

In order to consider the interfacial tensile and shear strengths, and to support a general strength criterion we need to consider a criterion for the stress as follows

$$\sqrt{\left(\frac{\sigma_{\theta\theta}}{\sigma_c} \right)^2 + \left(\frac{\sigma_{r\theta}}{\tau_c} \right)^2} \geq 1 \tag{3.8}$$

Here, $\sigma_{\theta\theta}$ and $\sigma_{r\theta}$ are the normal stress and shear stress acting at the interface in polar co-ordinate systems and σ_c and τ_c are the interfacial normal and shear strengths. From the energy release rate viewpoint, the interfacial crack is a mixed mode crack so the fracture

toughness of the interface G_c is a function of the mode mixity ψ. In this investigation, at least two expressions for G_c will be employed based on Hutchinson and Suo (1992):

$$G_c = G_{IC}\left(1 + (1-\lambda)\tan^2\psi\right)$$
$$G_c = G_{IC}\left(1 + \tan^2(1-\lambda)\psi\right) \tag{3.9b}$$

where the parameter λ adjusts the influence of the mode II contribution at the crack initiation. There are several ways to define the mode mixity angle ψ. For example, as suggested by Rice (1988), the mode mixity can be defined as

$$\psi = \tan^{-1}\frac{\sigma_{r\theta}}{\sigma_{rr}}\left(r = \bar{l}\right) \tag{3.10}$$

where $\bar{l}$ is a characteristic length and $\bar{l} = 100\mu m$ is used for brittle interface crack.

A brief approach of the numerical solution to the notch problem is explained here. Given the material properties and notch angle, the singularity problem is used to determine the value of the singularities λ_1, and λ_2. Only two values between 0 and 1 are chosen as singularities using asymptotic expansions for the stresses and displacements. An exterior problem is then used to calculate the value of the GSIF for unit load. This problem makes use of finite elements on the specimen level and uses three-point bending boundary conditions. An interior problem (Yosibash et al., 2006) is then used to calculate the shape function $A(\omega,\phi)$ using the critical length l_c.

3.3 Experimental methods

In order to study the influence of a bonded interface on a sharp notch, specimens as shown in Fig. 3.2 were tested in three-point bending and the crack initiation load was

recorded. In this section, material properties of the constituents and details of experimental methods are discussed. Polycarbonate (Piedmont Plastics, TN) and PMMA (Piedmont Plastics, TN) were chosen as materials to make notched specimens as shown in Fig. 3.2. Material properties of polycarbonate and PMMA are provided in Table 1. PMMA has a higher elastic modulus than polycarbonate by about 60%. However polycarbonate has a higher mode-I fracture toughness than PMMA by about three times. Each specimen is made of two individual parts which are bonded together using an adhesive to form a sharp notch. Two types of adhesives were used in the bonding process. While Weldon-10 was used as a strong adhesive, Loctite 384 was used as the weak adhesive. The adhesives were chosen such that their elastic properties are close to bulk polycarbonate such that we can model the interface as a line without any thickness but with different bonding strength and fracture toughness (Krishnan and Xu, 2010). Material properties of the various combinations of bonded interface are provided in Krishnan and Xu (2011a). The specimens were bonded together using a fixture and were cured for a period of 24 hours. Each specimen had the following dimensions: total length of 254 mm, width (W) of 50.8 mm and thickness of 5.4 mm. The height of the notch tip in every specimen was fixed at 19.05 mm from the bottom in order to allow for a fair comparison between specimens of varying notch angles. In this study, three different notch angles (β) of 30^o, 90^o and 120^o were chosen.

A sharp notch tip is essential as otherwise the presence of a finite tip radius may alter the determination of the crack initiation load. Many previous researchers have studied specimens that have been machined with a V-notch (Carpinteri, 1987; Strandberg, 2002; Gomez and Elices, 2003; to name a few). This poses a disadvantage in

that the notch tip may have a finite root radius and thereby weaken the notch tip singularity. The measured crack initiation load will be higher if the notch tip is not sharp. The influence of notch tip radius on the validity of fracture toughness data is discussed in Strandberg (2002) and Fett (2005). This problem is overcome in our case by bonding together two individual halves and thereby eliminating the need for machining a notch. The excess adhesive at the notch tip was removed prior to curing.

All the specimens were tested in three-point bending using a standard fixture mounted on a MTS 810 machine. The experimental set-up consists of three parts including a mechanical system to load the specimen, an optical system to develop fringe patterns and an imaging system to record the fringe patterns (further details in Krishnan and Xu, 2010). The loading point S was varied from 0 mm (center) to 30 mm and -30 mm (on either side of center line) on the top of the specimen as shown in Fig. 3.2. A loading span length of 60 mm was chosen. The crack initiation load P_i is recorded either from the load-displacement curve or by observation from in-situ optical techniques.

The fringe patterns developed only in case of the transparent Polycarbonate specimens, and the isochromatic fringe patterns are the contours of the maximum in-plane shear stress (Kobayashi, 1987):

$$\tau_{\max} = \frac{(\sigma_1 - \sigma_2)}{2} = \frac{Nf_\sigma}{2h} \tag{3.11}$$

where σ_1 and σ_2 are the in-plane principal stresses, N is the fringe order, f_σ is the stress-fringe constant, and h is the thickness of the specimen.

Table 3.1 Material properties for polycarbonate (PC), PMMA and aluminum

	Polycarbonate	PMMA	Aluminum
Density (kg/m^3)	1200	1190	2700
Elastic Modulus (GPa)	2.378	3.79	70
Poisson's Ratio	0.37	0.37	0.35
Tensile Strength (MPa)	62	79	400 (Yield)
Shear Strength	41	40	220 (Yield, approx.)
Mode-I Fracture Toughness (MPa $m^{1/2}$)	3.53	1.15	36

3.4 Results for same-material systems

Results from experiments involving same-materials are presented in this section. The first part describes the effect of the notch angle β on the crack initiation load. The second part describes the effect of the loading point S on the crack initiation load. Within each section, the differences between strong and weak bond are highlighted. Also, the results for the two different material types (PMMA and polycarbonate) are presented under each sub-section. The crack initiation loads from the experimental testing are provided in Table 3.2 for polycarbonate specimens and in Table 3.3 for PMMA specimens. Every data point in Tables 3.2 and 3.3 represents an average value of crack

initiation load from atleast three experiments. The bonding tensile and shear strength and mode-I fracture toughness of each type of bond is further presented in Tables 3.2 and 3.3. The crack initiation load for each type of notch angle and loading point is presented in the Tables systematically.

Table 3.2 Average crack initiation loads for same-material polycarbonate specimens

Notch Angle / Bonding	S (mm)	30^0 (N)	90^0 (N)	120^0 (N)	Bonding Tensile strength (MPa)	Bonding Shear Strength (MPa)	K_{IC} (MPa $m^{1/2}$)
Weak	0	222	329	378	6.06	10.99	0.64
	30	393	477	906			
	-30	536	964	1100			
Strong	0	337	718	1036	12.93	15.52	0.86
	30	1515	1358	1677			
	-30	1275	2857	2980			

Table 3.3 Average crack initiation loads for same-material PMMA specimens

Notch Angle / Bonding	S (mm)	30^0 (N)	90^0 (N)	120^0 (N)	Bonding Tensile strength (MPa)	Bonding Shear Strength (MPa)	K_{IC} (MPa $m^{1/2}$)
Weak	0	277	352	455	12.66	11.58	0.71
	30	522	747	941			
	-30	666	1341	1498			
Strong	0	941	1304	1882	20.87	25.35	1.74
	30	2642	2772	3465			
	-30	2586	3388	X			

3.4.1 Effect of notch angle on crack initiation load

The angle of the notch has a pronounced effect on crack initiation. A smaller notch angle is similar to a crack and hence is expected to show a much lower crack initiation load than a large notch angle. A crack is indeed a special case of a notch, with notch angle of 0^o. On the other extreme, a straight edged bar represents a notch angle of 180^o when there is no notch. In order to study the influence of the notch angle on the crack initiation load, three diverse notch angles of 30^o, 90^o and 120^o were used. Notch angles of more than 120^o were not considered due to their very high bending load and corresponding uncertainty in their load data. The load was fixed at the center of the specimen (S=0) for all cases in this sub-section (3.4.1) alone in order to allow for a fair comparison.

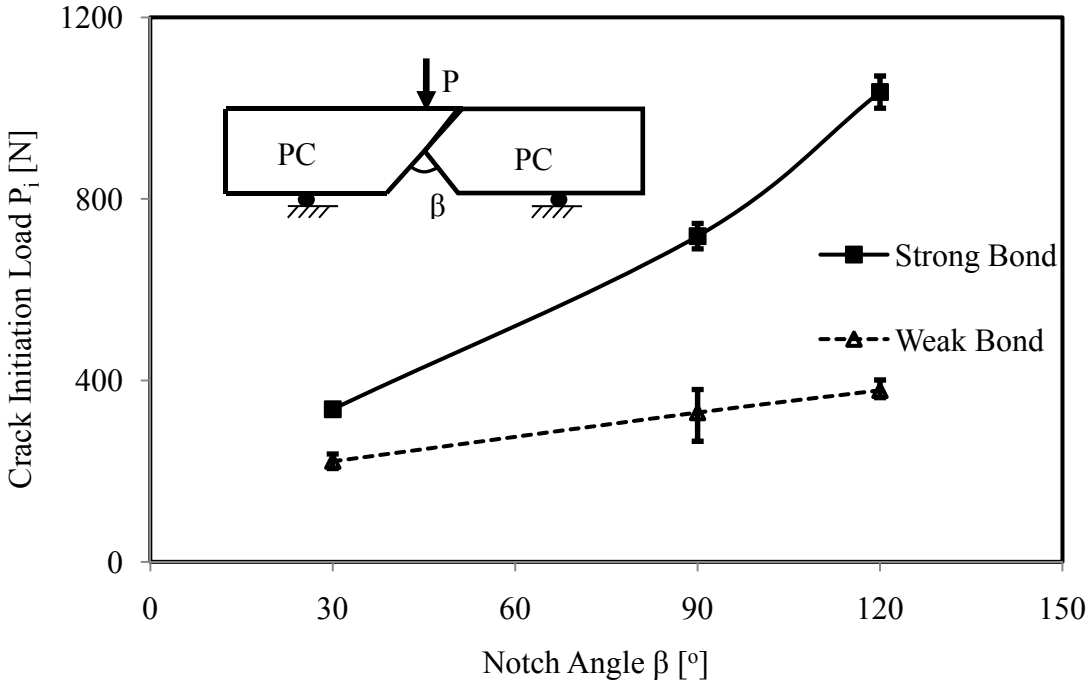

Fig. 3.3 Effect of notch angle on crack initiation load on same-material polycarbonate systems for S=0.

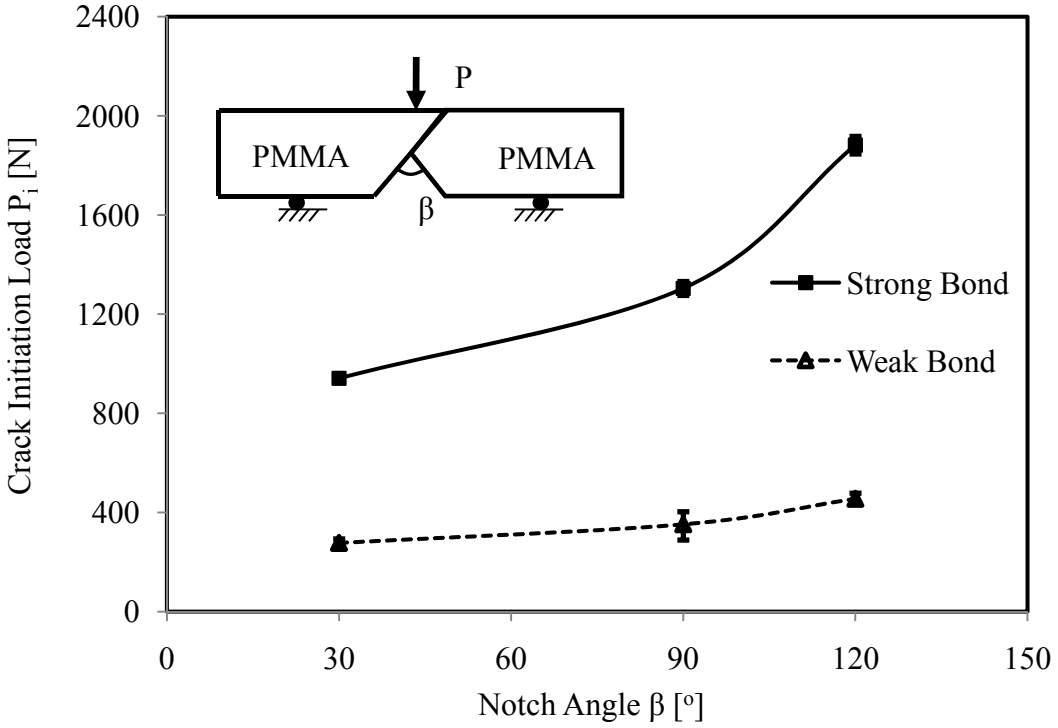

Fig. 3.4 Effect of notch angle on crack initiation load on same-material PMMA systems for S=0.

The crack initiation load shows an increase with notch angle as shown in Fig. 3.3 for both the strongly and weakly bonded polycarbonate specimens. A similar trend is depicted by PMMA specimens as shown in Fig. 3.4. The weakly bonded specimens always show a lower crack initiation load than the strongly bonded specimens. This is true for both polycarbonate and PMMA specimens and is due to the difference in strength of these bonded materials with the different adhesives (Krishnan and Xu, 2011a). While the increase in crack initiation load is sharp in case of strong bond, it is almost linear for the weakly bonded specimens. This increase can be explained using a simple stress transfer diagram as shown in Fig. 3.5(a). Consider a schematic specimen as shown in Fig.

3.5(a) with a general notch angle β. The Cartesian and radial coordinates are as indicated in the figure. The stress transformation from Cartesian coordinates to radial coordinates can be represented by the following equations

$$\begin{aligned}\sigma_{rr} &= \sigma_{xx}\cos^2\theta + \sigma_{yy}\sin^2\theta + 2\sigma_{xy}\sin\theta\cos\theta \\ \sigma_{\theta\theta} &= \sigma_{xx}\sin^2\theta + \sigma_{yy}\cos^2\theta - 2\sigma_{xy}\sin\theta\cos\theta \\ \sigma_{r\theta} &= -\sigma_{xx}\sin\theta\cos\theta + \sigma_{yy}\sin\theta\cos\theta + \sigma_{xy}(\cos^2\theta - \sin^2\theta)\end{aligned} \tag{3.12}$$

At a point along the interface and close to the notch tip, the stresses under a point load at the center in the yy and xy directions will be zero. Therefore σ_{yy} will be approximately 0 and σ_{xy} will be 0. Therefore the stresses in radial coordinates can be expressed as

$$\begin{aligned}\sigma_{rr} &= \sigma_{xx}\cos^2\theta \\ \sigma_{\theta\theta} &= \sigma_{xx}\sin^2\theta \\ \sigma_{r\theta} &= -\sigma_{xx}\sin\theta\cos\theta\end{aligned} \tag{3.13}$$

The ratio of shear stress to normal stress in polar coordinates then becomes

$$\frac{\sigma_{\theta\theta}}{\sigma_{r\theta}} = -\tan\theta \tag{3.14}$$

And in terms of notch angle β, this is equivalent to

$$\frac{\sigma_{\theta\theta}}{\sigma_{r\theta}} = -\tan(90 - \frac{\beta}{2}) = -\cot(\frac{\beta}{2}) \tag{3.15}$$

A graph of the magnitude of the ratio of normal to shear stresses as a function of notch angle is provided in Fig. 3.5(b). This graph illustrates an increase in shear stress in comparison with normal stress in case of larger notch angles. This leads to an increase in crack initiation load with notch angle.

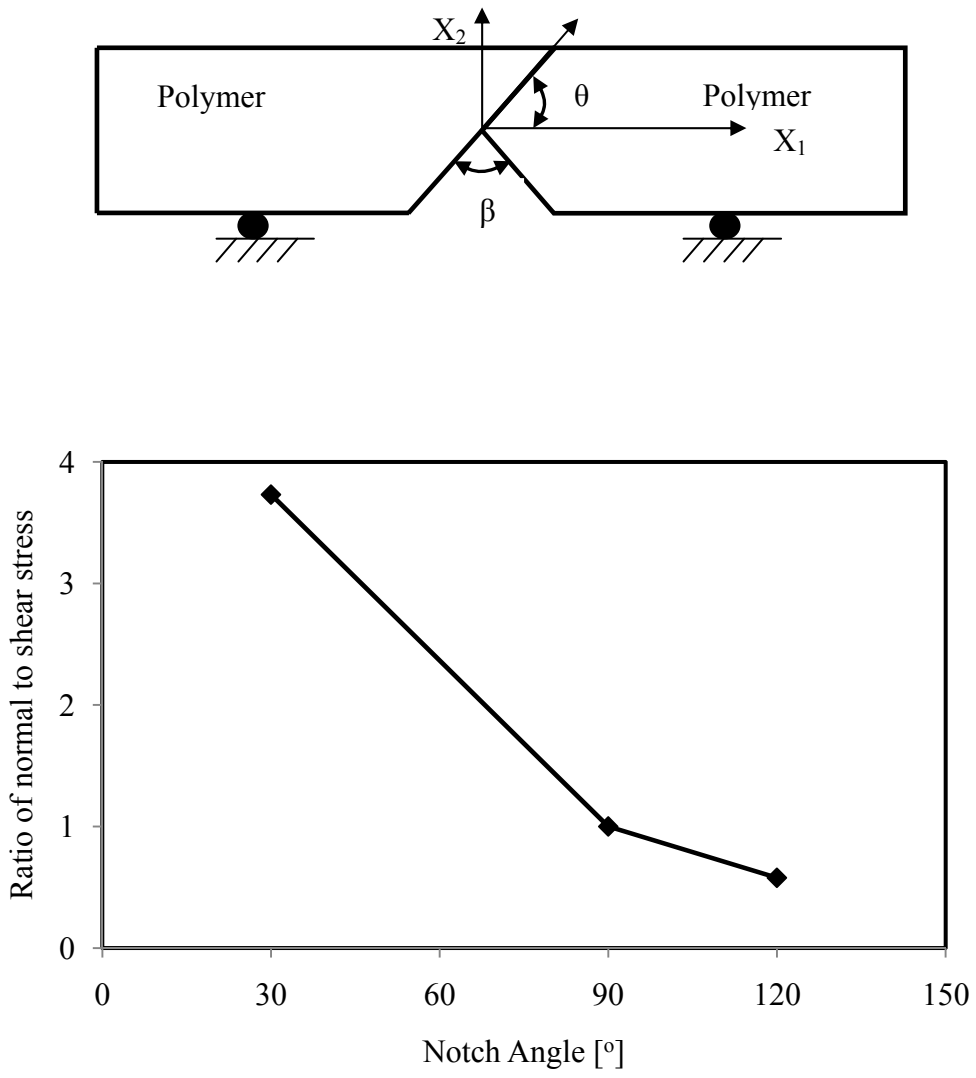

Fig. 3.5 (a) Stress transfer diagram for notch-interface specimens **(b)** Variation of ratio of normal/shear stress ratio with notch angle

Typical failure patterns of strongly bonded polycarbonate specimens with increasing notch angle are shown in Fig. 3.6. The crack always initiated from the notch and propagated along the interface. The presence of an artificially weak bonded interface forces the crack to always initiate along this bonded line. In case of a notch angle of 30^{o}

the crack propagation continues along the interface while notch angles of 90^o and 120^o show crack kinking into the bulk polycarbonate. The kinking patterns are consistent and are always towards the loading point. PMMA specimens also showed similar and consistent failure patterns except in case of $\beta=30^o$. In case of notch angle of 30^o, PMMA specimens show crack kinking into bulk polymer. This phenomenon was repeatable as shown by the pictures in Fig. 3.7 for strongly PMMA specimens with $\beta=30^o$. The crack paths of the specimens shown in Fig. 3.7 are digitized and represented as a graph in Fig. 3.8 (data in Table 3.3). It is seen that the three specimens have very close crack paths and ensure that our tests are repeatable. The fracture surfaces in case of the kinked crack were observed to be smooth indicating a strong mode-I component. The kinking tends to start from closer to the notch tip (along the interface) when the notch angle is increased as can be seen in Fig. 3.6. However, in sharp contrast with strong bond, weakly bonded specimens of polycarbonate and PMMA always failed along the interface. Fig. 3.9 shows PMMA specimens with notch angles of 30^o and 90^o showing failure along the interface without any crack kinking into the bulk material. There was no crack kinking, even for higher notch angles, observed in case of weakly bonded specimens.

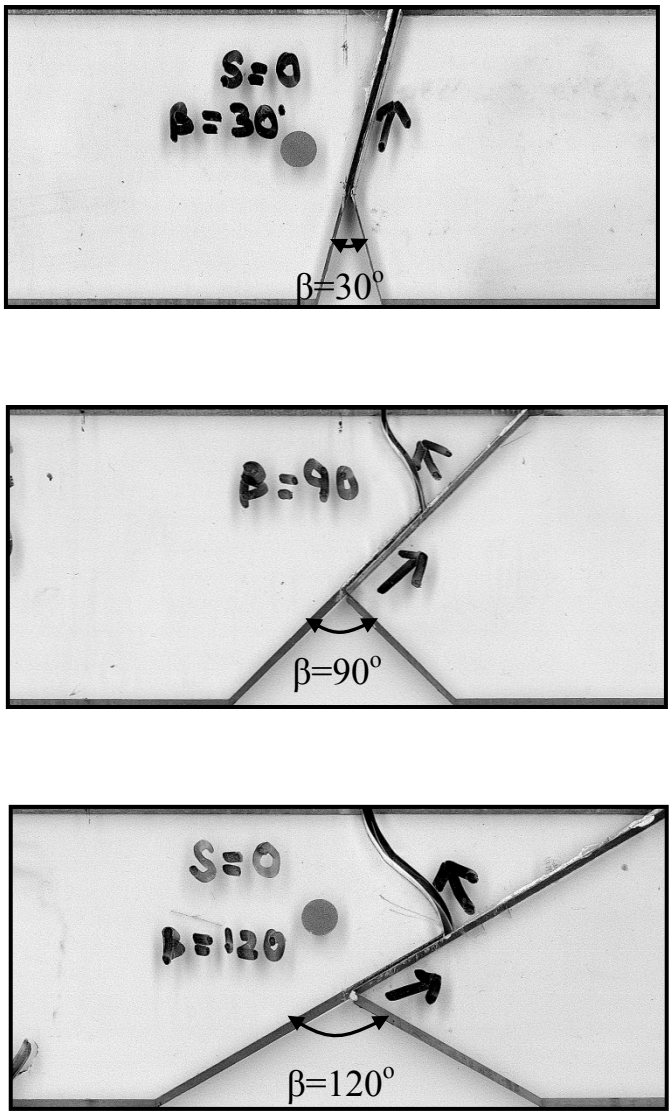

Fig. 3.6 Failure patterns for strongly bonded same-material polycarbonate (PC) specimens with S=0. Notch angles are illustrated in the pictures. (Circular dot is a mark of diameter 6.35 mm)

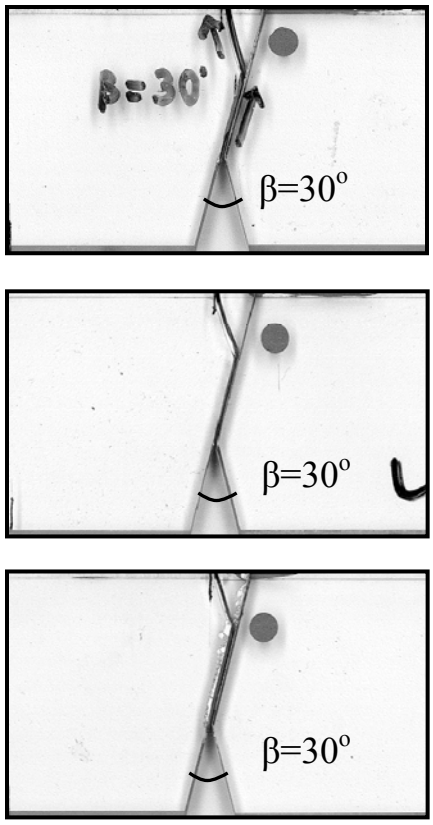

Fig. 3.7 Consistent kinking patterns for three different specimens of strongly bonded PMMA specimens with notch angle of 30° and loading at S=0 mm.

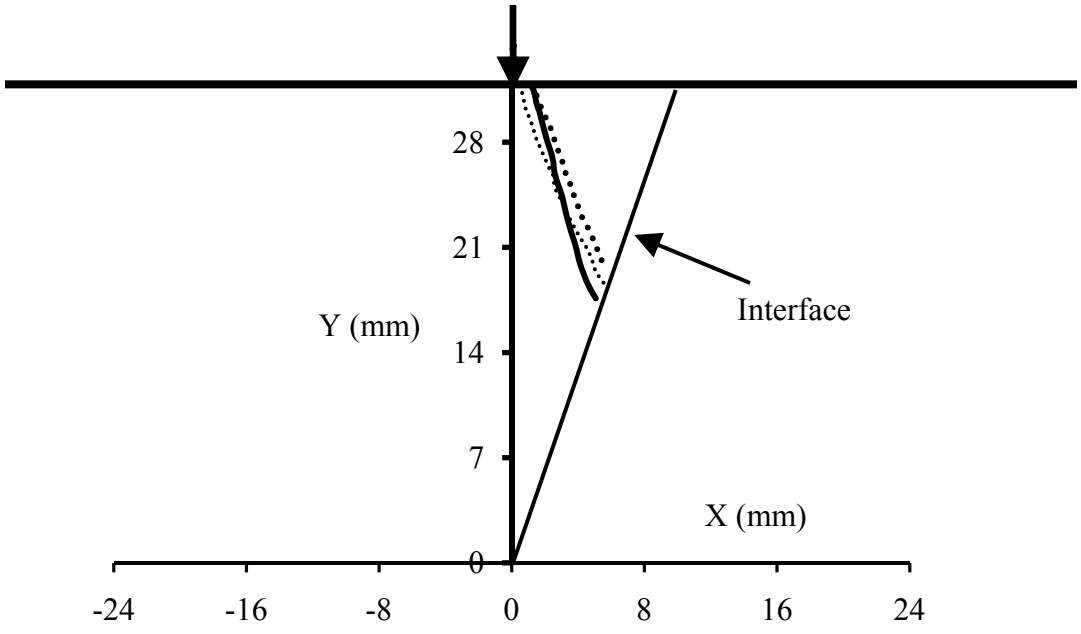

Fig. 3.8 Kinked crack paths for strongly bonded PMMA with notch angle of 30°.

Table 3.4 Crack path co-ordinates for PMMA specimens (shown in Fig. 3.8) with notch angle of 30^o and S=0 mm

Specimen 1		Specimen 2		Specimen 3	
X	Y	X	Y	X	Y
1.30168	50.4521	5.28328	38.1527	1.26824	50.7125
1.50299	49.5822	5.07058	38.7469	1.52439	50.0661
1.70615	48.8863	5.02911	39.1289	1.73743	49.6351
1.90701	47.9729	4.94428	39.426	1.90872	49.0749
1.94127	47.2336	4.6877	39.8079	2.16522	48.3422
2.14305	46.4072	4.39	40.6567	2.33686	47.6959
2.26384	45.8853	4.38827	40.2323	2.5937	46.8771
2.50772	45.0589	4.17593	40.9114	2.80777	46.1876
2.71088	44.363	3.87754	41.5904	3.06358	45.6273
2.82798	43.4932	3.70648	41.845	3.31992	44.9377
3.07232	42.7103	3.62182	42.1846	3.40702	44.2914
3.27318	41.7969	3.23894	43.2456	3.6637	43.5157
3.51798	41.0575	3.2367	42.6938	3.87673	43.0847
3.75818	39.8832	2.98236	43.6275	4.00524	42.6538
4.12747	38.9699	2.81234	44.1368	4.13341	42.309
4.48983	37.4041	2.59896	44.5612	4.34713	41.7057
4.94103	36.2733	2.38541	44.9432	4.56017	41.2747
		2.34445	45.4525	4.73146	40.7145
		2.08805	45.8769	5.07249	39.9817
		1.96157	46.5136	5.37142	39.206
		1.79121	46.938	5.66985	38.5595
		1.49316	47.7019		
		1.32315	48.2112		
		1.19615	48.7205		
		0.982771	49.1449		
		0.814135	49.9938		
		0.771631	50.1211		
		0.558247	50.5455		

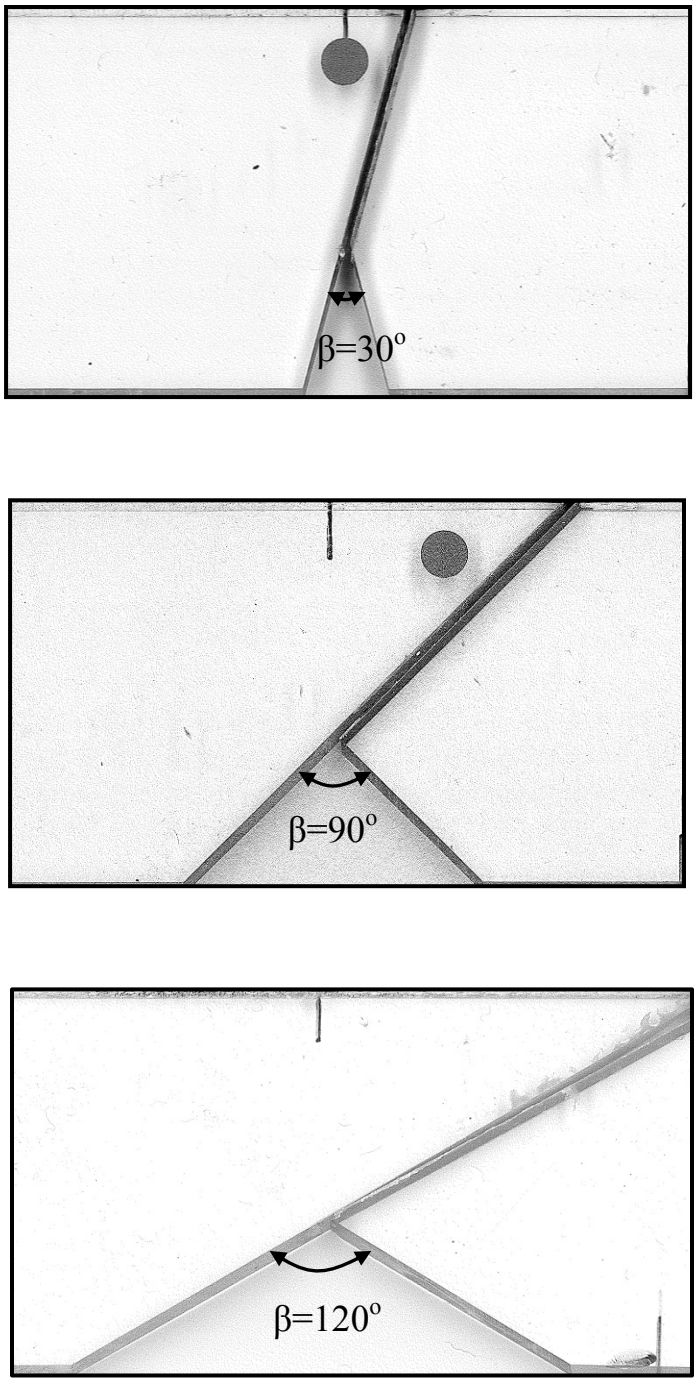

Fig. 3.9 Crack path along the interface for weakly bonded PMMA specimens with load at S=0.

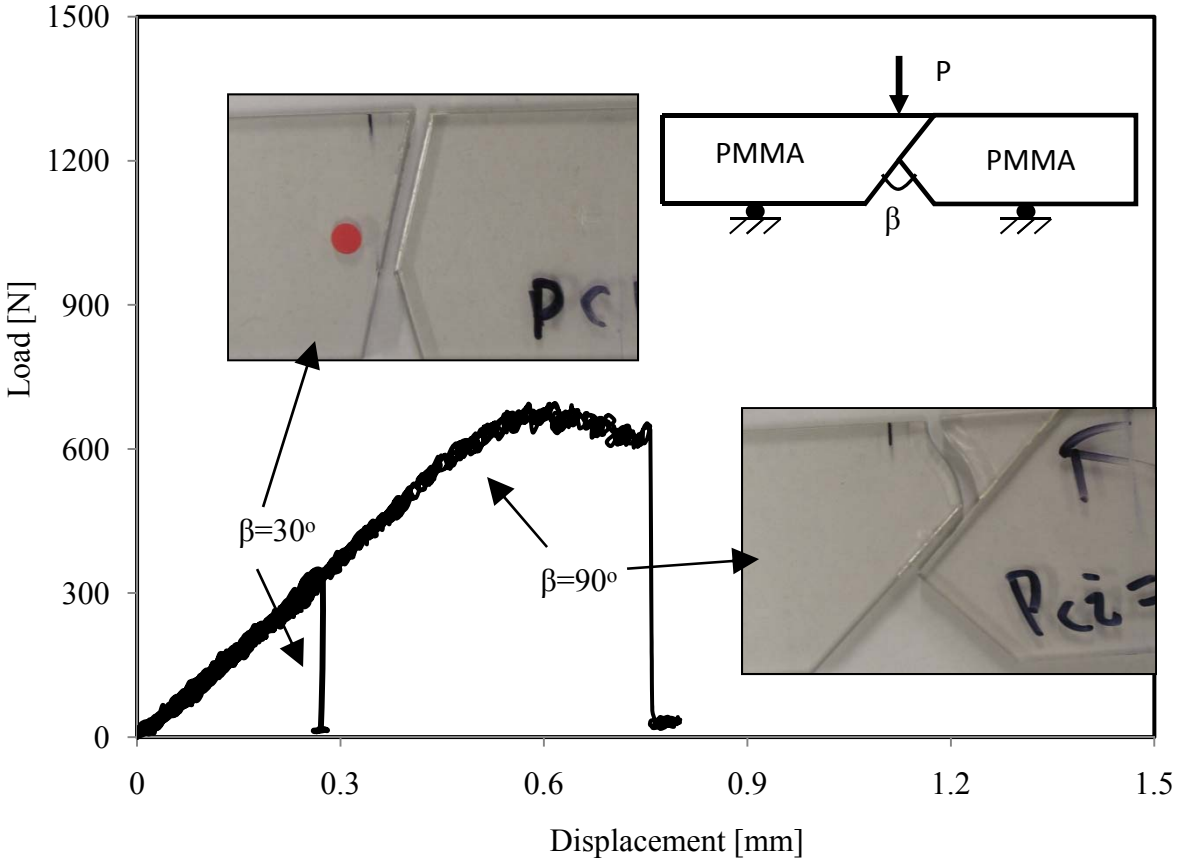

Fig. 3.10 Typical load-displacement plot for a strong bonded same-material polycarbonate specimen with a notch angle 30° and S=0 and notch angle 90°.

Typical load-displacement curves for strongly bonded polycarbonate specimens with notch angles of 30° and 90° are presented in Fig. 3.10 and for notch angle of 120° in Fig. 3.11. These two graphs are plotted on the same axes in order to allow for fair comparison. Specimens with β=30° and β=90° show a linear load-displacement curve with sudden failure at peak load. However, β=90° shows a very different failure pattern. There are two distinct kinks observed in the load-displacement curve before final failure. This shows that there is a clear difference between the crack initiation and the ultimate failure load. The load recorded in this case is the crack initiation load which is obtained clearly from the load-displacement plot.

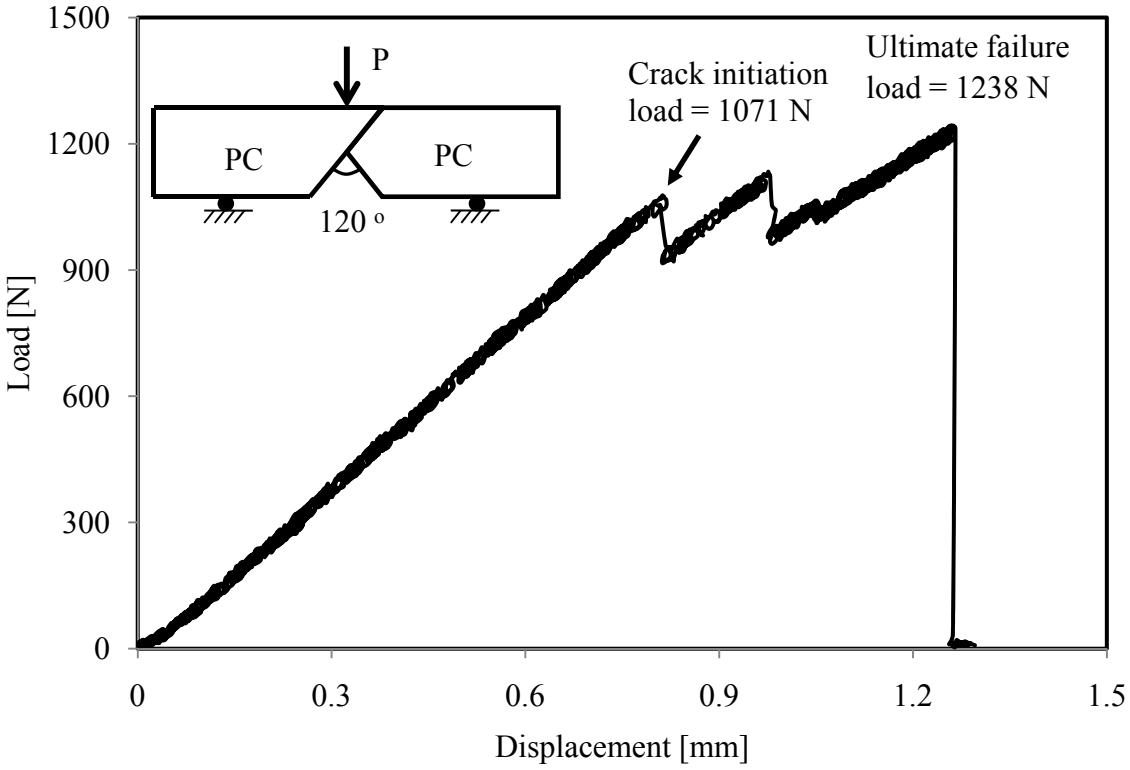

Fig. 3.11 Typical load-displacement plot for a strong bonded same-material polycarbonate specimen with a notch angle 120^o and S=0.

The difference in load-displacement plot between weakly and strongly bonded polycarbonate specimens with the same notch angle is highlighted in Figs. 3.12 and 3.13 respectively. Fig. 3.12 shows that weakly bonded polycarbonate specimen with $\beta=90^o$ shows crack initiation followed by a load drop. But the specimen continues to take load due to friction between the now debonded halves. Therefore, the specimen continues to take load until the displacement reaches a very high value followed by failure. This is in sharp contrast with a strongly bonded polycarbonate specimen with a same notch angle of 90^o. The failure in this case is sudden and explosive.

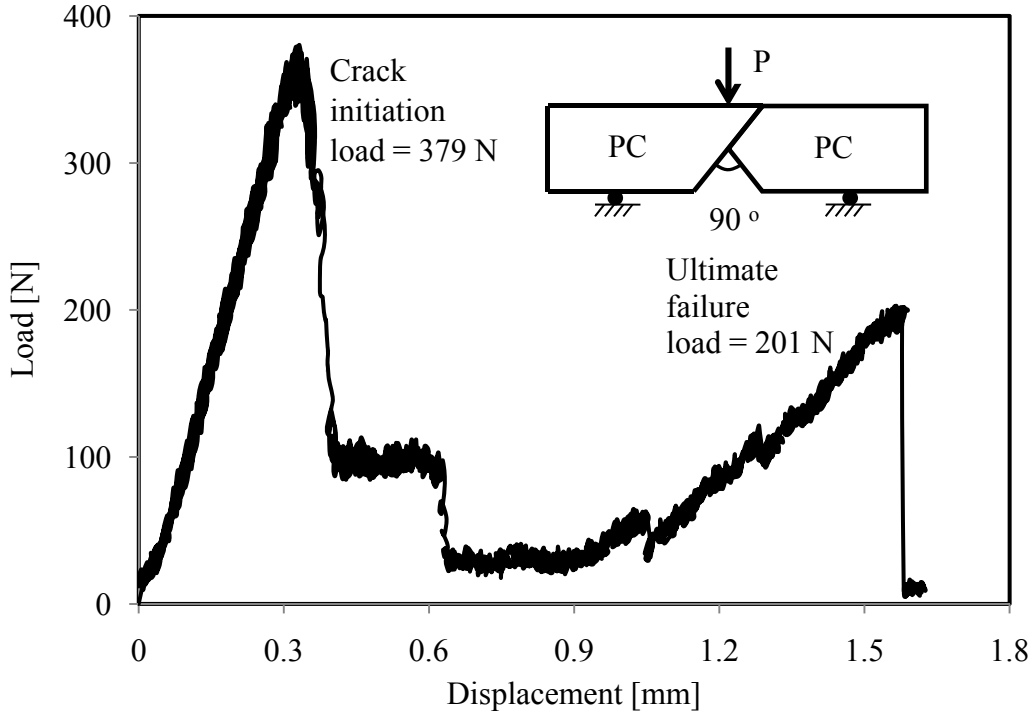

Fig. 3.12 Typical load-displacement plot for a weakly bonded same-material polycarbonate specimen with notch angle of 90^{o} and load at S=0.

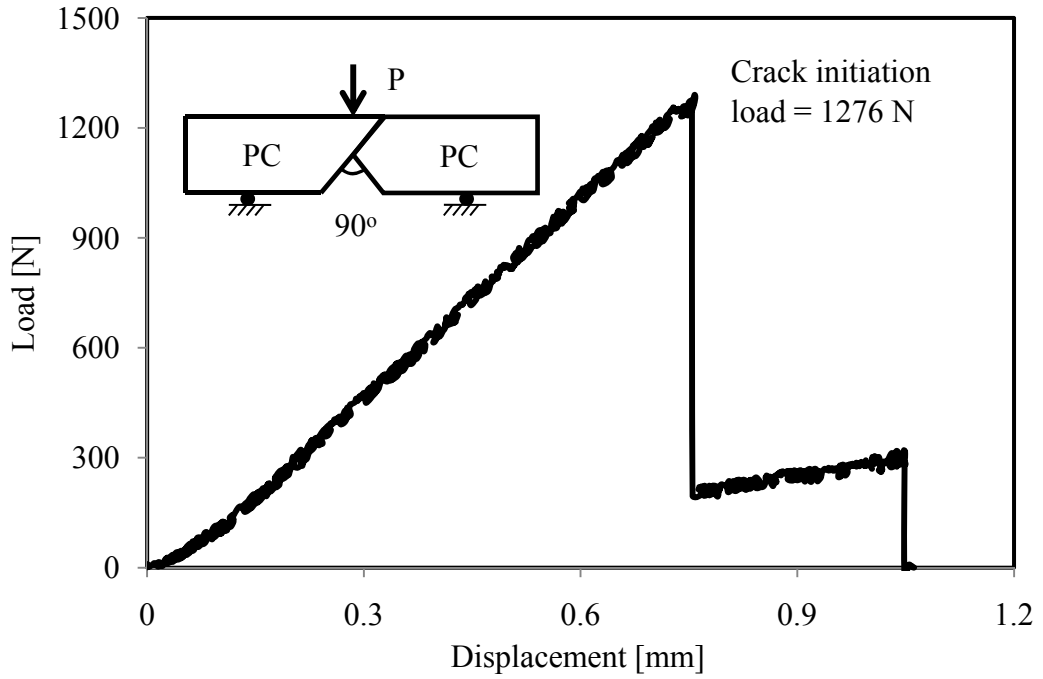

Fig. 3.13 Typical load-displacement plot for a strongly bonded same-material polycarbonate specimen with notch angle of 90^{o} and load at S=0.

The difference in case of strong and weak bonds is illustrated in Fig. 3.14 for PMMA specimens. The two load-displacement plots are presented in the same graph in order to illustrate the same initial stiffness until crack initiation. The choice of adhesive with a material only changes the point at which crack initiation occurs while maintaining the same initial stiffness. In Fig. 3.14 the strongly and weakly bonded specimens are of PMMA material type and have a notch angle of 120^o. The strongly bonded specimens show a linear increase in load followed by a sudden crack initiation and immediate failure. This is different in case of weakly bonded specimen where there is crack initiation and a region of interfacial friction.

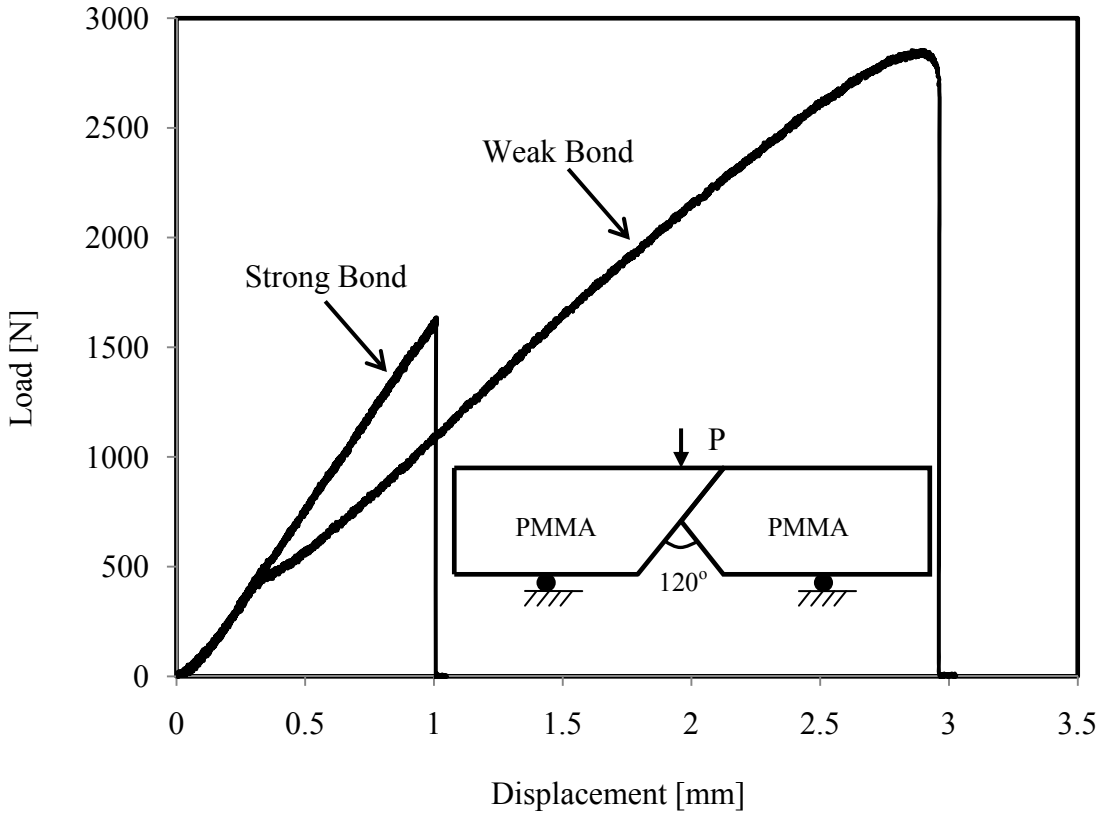

Fig. 3.14 Comparison of load-displacement plots for strong and weak bond PMMA specimens with notch angle of 120^o and load at S=0.

3.4.2 Variation of crack initiation load with loading point S

This sub-section describes the variation in crack initiation load when the loading point is shifted from the center. The offset of the loading point (S) is measured from the center line as indicated in Fig. 3.2. The offset is varied from S=0 to S=-30 and S=30 (all in mm) in order to vary the mode mixity at the notch tip. Suresh et al. (1990) describe an experimental technique involving the variation in mode-mixity with the offset in loading point. While Suresh et al. (1990) describe four-point bending, our experiments concentrate on three-point bending for notched specimens with an interface. The crack initiation load is found to increase when the loading point (S) is shifted away from the center. Figs. 3.15 and 3.16 illustrates the variation in crack initiation load for the three different loading points for strongly bonded polycarbonate and PMMA systems respectively.

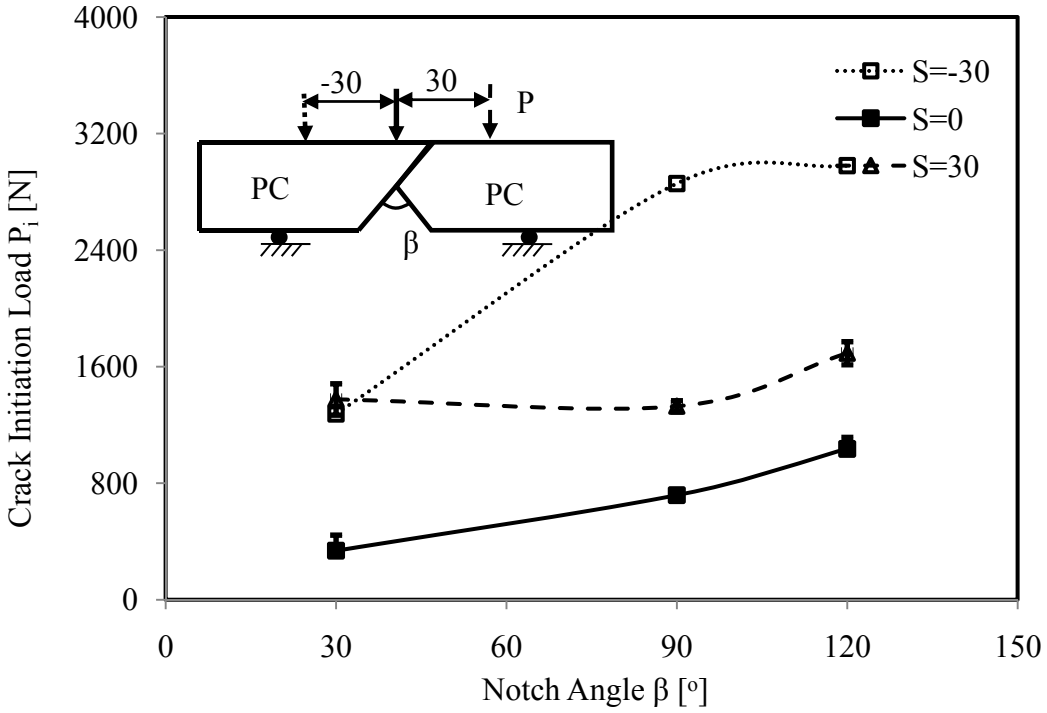

Fig. 3.15 Variation of crack initiation loads with notch angle for different loading points (S) for polycarbonate same-material strongly bonded systems.

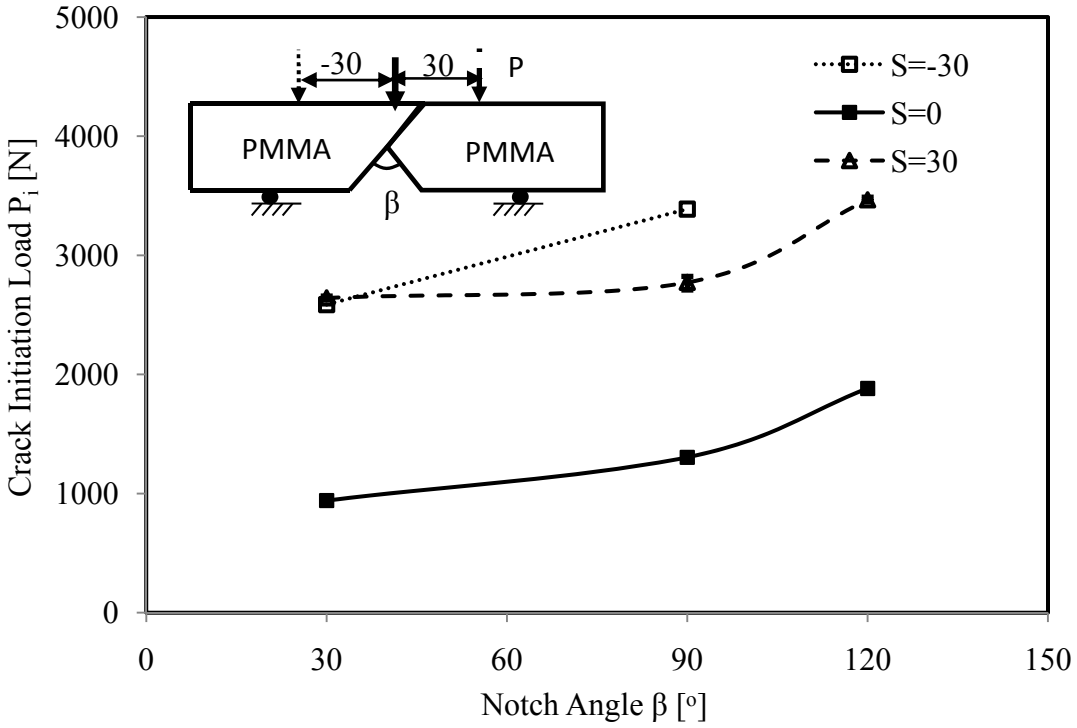

Fig. 3.16 Variation of crack initiation loads with notch angle for different loading points (S) for PMMA same-material strongly bonded systems.

When S is 0, the system is almost symmetric and is similar to mode I cracking. The presence of mode II component is limited in this case. However, moving the loading point to either S=30 mm or S=-30 mm brings about a significant mode II component which causes an increase in the load required to cause interfacial debonding. The failure pattern is also significantly different in the three cases with crack kinking dominating over interfacial debonding as the loading point is varied. This effect is especially pronounced in case of $\beta=120^{o}$ and the corresponding failure patterns are as indicated in Fig. 3.17. There is consistent crack kinking for all three specimens towards the loading point. The kinking angles and kinking lengths seem to vary with the point of applied load. The failure patterns have also been digitized for the cases presented in Fig. 3.17 and

the corresponding crack path is depicted in Table 3.4. Each data set represents the x and y point of the crack path relative to the crack tip. Fig. 3.18 shows the three digitized crack paths variation with varying loading points.

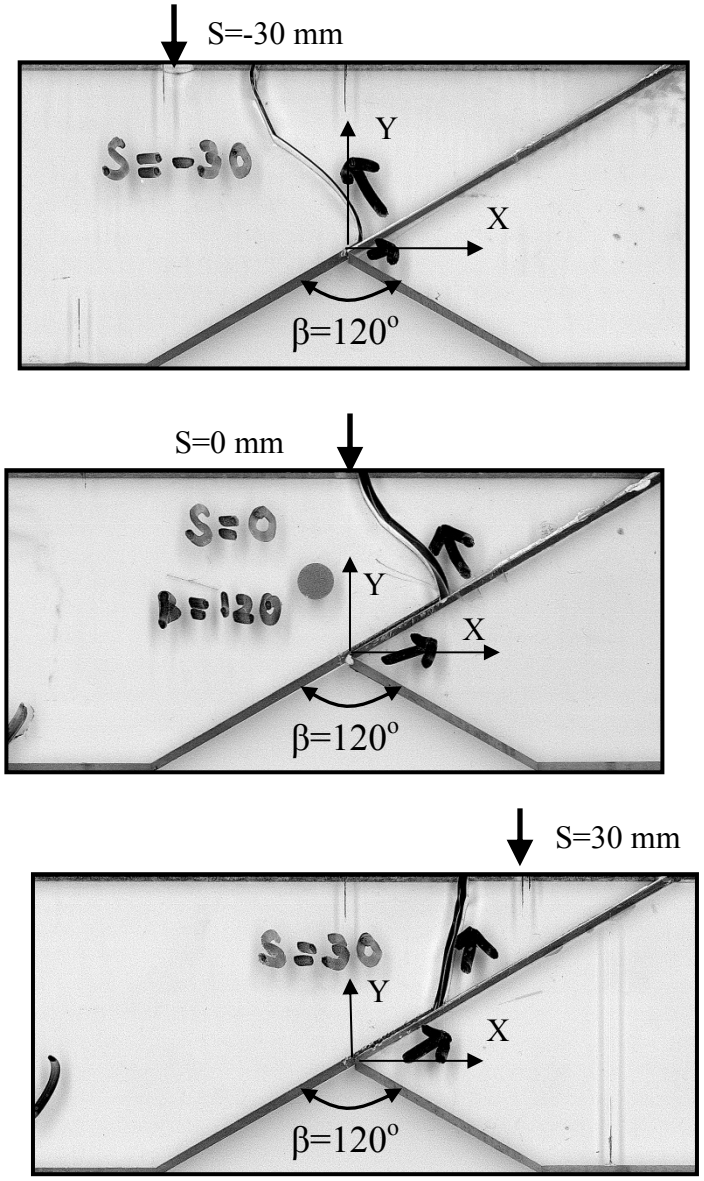

Fig. 3.17 A comparison of the typical failure patterns for same-material polycarbonate specimens with $\beta=120^{o}$ and with variation in S.

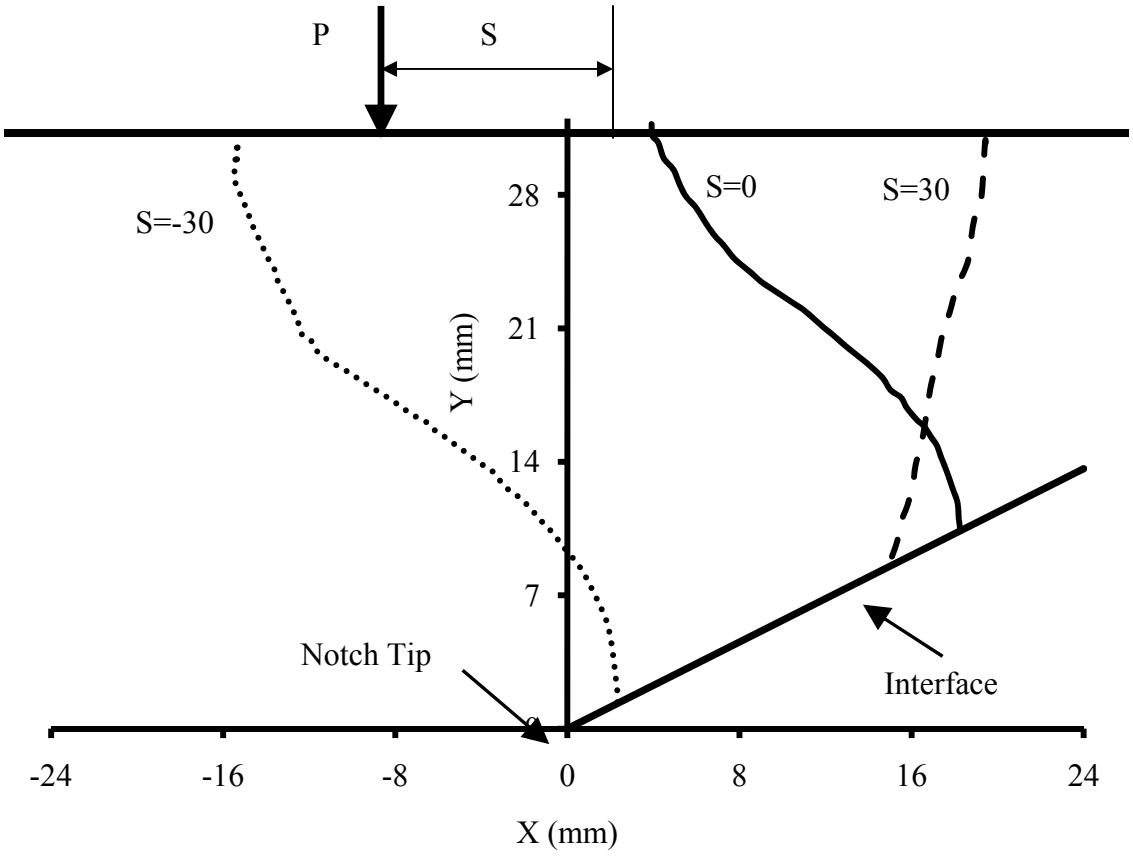

Fig. 3.18 Kinked crack paths for strongly bonded polycarbonate with notch angle of 120^{o} and for different values of loading point. Origin is at notch tip. Data is presented in Table 3.4.

Table 3.5 Crack path co-ordinates for notch angle of 120^{o} and S=-30 mm

S= -30 mm		S=30 mm		S=0 mm	
X (mm)	Y (mm)	X (mm)	Y (mm)	X (mm)	Y (mm)
-15.36	29.87	15.09	9.03	3.91	31.71
-15.33	30.77	15.34	9.86	3.95	31.09
-15.48	28.97	15.47	10.73	4.22	30.74
-15.21	28.03	15.81	11.72	4.48	29.91
-14.9	27.21	16.07	12.89	4.92	29.34
-14.64	26.40	16.19	13.84	5.18	28.64
-14.24	25.46	16.45	14.93	5.49	27.94
-13.93	24.69	16.62	15.97	5.97	27.34
-13.58	24.00	16.75	16.97	6.41	26.55

-13.43	23.36	16.92	18.09	6.85	25.85
-13.11	22.76	17.21	19.40	7.25	25.37
-12.84	22.11	17.43	20.66	7.78	24.63
-12.56	21.48	17.77	21.83	8.48	23.97
-12.38	20.74	18.11	23.17	9.01	23.44
-11.92	20.36	18.62	24.51	9.58	23.01
-11.56	19.68	18.83	26.21	10.28	22.48
-11.11	19.33	19	27.08	11.03	21.92
-10.74	19.07	19.25	27.89	11.69	21.26
-10.03	18.60	19.42	30.80	12.3	20.69
-9.66	18.30	19.47	30.06	12.87	20.13
-9.12	17.91			13.35	19.69
-8.5	17.48			13.88	19.21
-7.88	17.01			14.28	18.81
-7.18	16.45			14.67	18.38
-6.64	16.15			15.02	17.76
-6.15	15.64			15.51	17.37
-5.74	15.34			15.77	16.84
-5.08	14.78			16.25	16.19
-4.5	14.31			16.56	15.89
-3.88	13.79			16.87	15.36
-3.39	13.41			17.18	14.84
-2.94	12.72			17.35	14.31
-2.45	12.33			17.62	13.53
-1.79	11.65			17.92	12.56
-1.31	11.01			18.14	11.83
-0.86	10.49			18.19	11.04
-0.54	10.06			18.27	10.38
-0.17	9.51				
0.35	8.82				
0.83	8.01				
1.7	5.99				
1.96	5.01				
2.13	3.81				
2.22	2.91				
2.32	1.96				
2.32	1.32				

The three-point bend experiments are also consistent as shown in Fig. 3.19 for three different polycarbonate specimens with a notch angle β of 90^o and a loading point at S=-30 mm. The crack paths are digitized and the corresponding patterns are presented on a same graph as shown in Fig. 3.20.

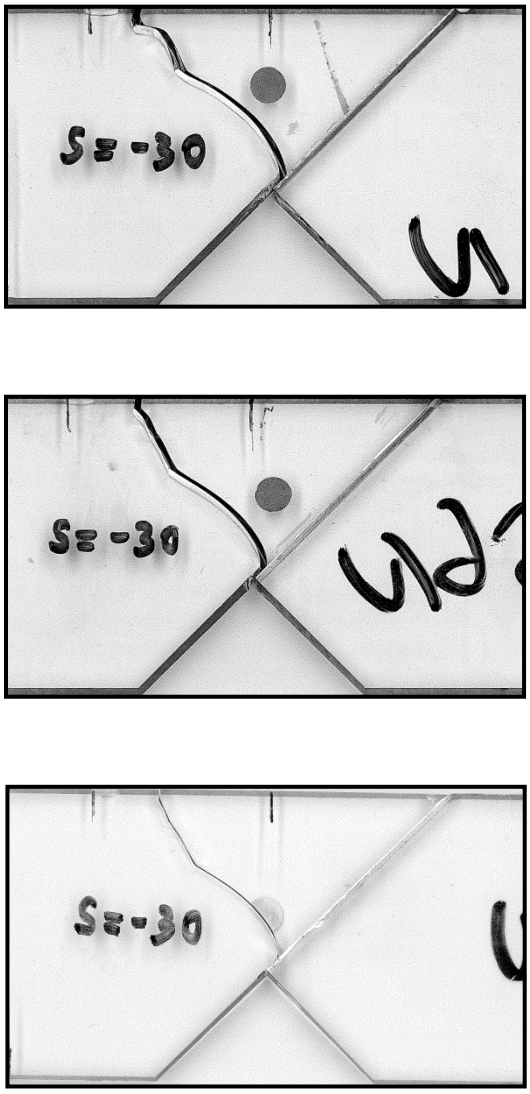

Fig. 3.19 Consistent crack paths shown for polycarbonate same-material specimens with notch angle of 90^o and loading point at S=-30 mm.

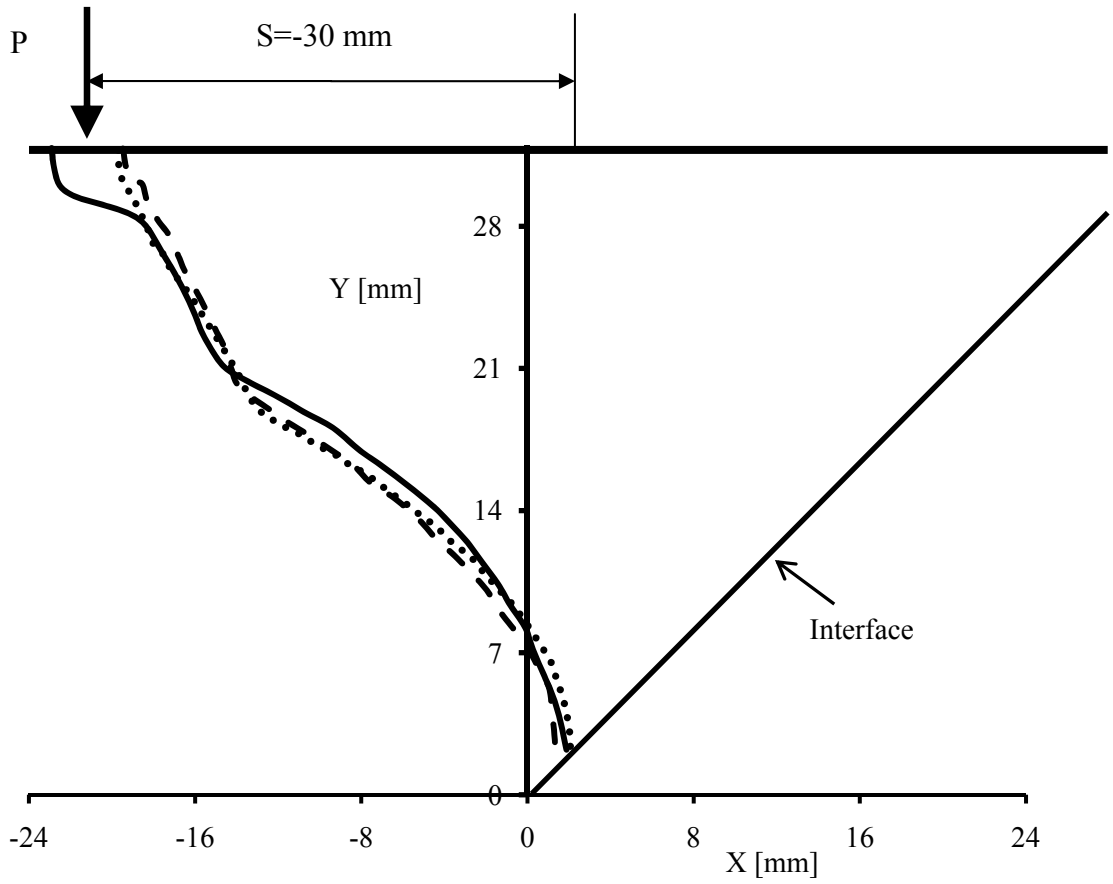

Fig. 3.20 Kinked crack paths for strongly bonded polycarbonate with notch angle of $90^{o}$and loading at S=-30 mm. Origin is at notch tip.

The loading points of S=30 mm and S=-30 mm are relatively symmetric with respect to the center of the geometry. In case of same-material systems, the materials also have the symmetry. This is as shown in Fig. 3.21 for polycarbonate and in Fig. 3.22 for PMMA, both of which compare the three loading conditions for a notch angle of 30^{o}. The S=0 mm loading point gives rise to a mode I component and hence has a lower load as discussed above. The S=-30 mm case has a higher initiation load than the S=30 mm case. This could be due a greater mode II component induced by the former. The load point

corresponding to S=-30mm is further away from the interface than S=30. Therefore, it induces more friction in the form of interfacial contact along the interface and hence produces a greater load. A similar trend is observed in case of notch angles of 90^o and 120^o. Also, the weak bond specimens exhibit a similar curve as the strong bond specimens albeit with a lower load. The loading point has a strong influence on the crack initiation load in case of notch-interface specimens. The mode mixity is influenced to a large extent by the loading point. Applying the load at the center or close to the center induces a strong mode I component. Moving away from the center induces a mode II component along with the existing mode I component and increases the crack initiation load. Fringe patterns corresponding to a notch angle of 120^o with loading conditions of S=0, -30 and 30 are presented in Fig. 3.23 for various loading cases. The difference in fringes at the notch tip can be clearly seen. There is a loss in symmetry when the loading is shifted from S=0 mm to S=30 mm. There is a resolution error which is caused due to the time lag in observation of the fringe and the recording the load. This error could be of the order of 50-100 N and depends on how accurately the load from the MTS machine and the fringe observed from the digital camera (as discussed in the section on experimental methods) are correlated.

It should be noted that all of the specimens involve crack initiation from the notch and not from anywhere else in the bulk material. Also, the crack always propagated along the interface in every single case. In some of the cases as described above crack kinking then occurs into the bulk material.

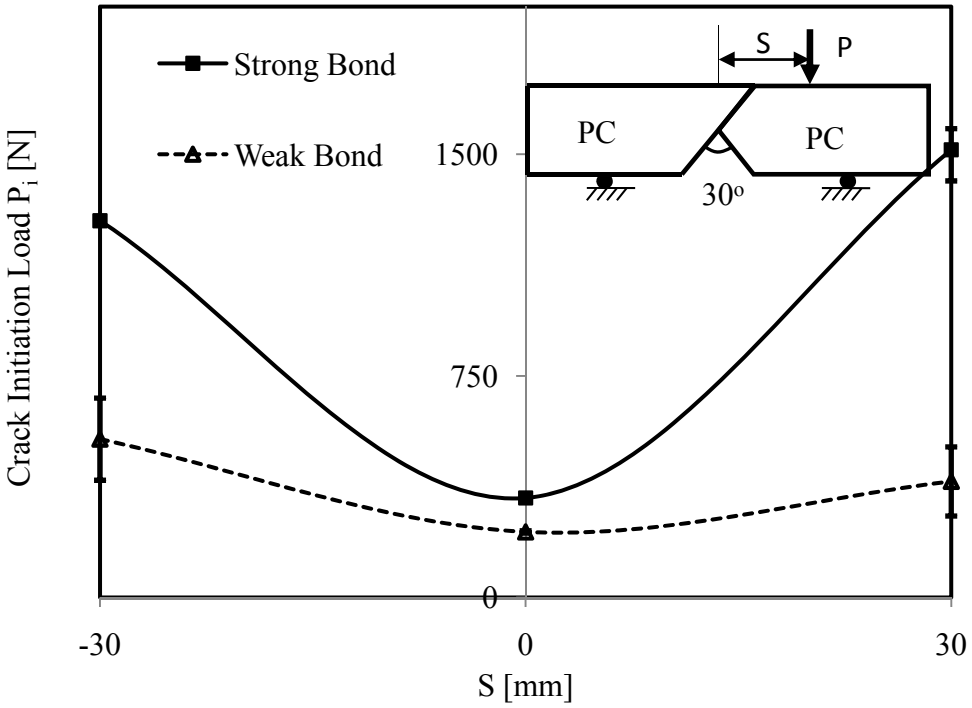

Fig. 3.21 Crack initiation loads loading points (S) for Polycarbonate same-material systems with a notch angle of 30°

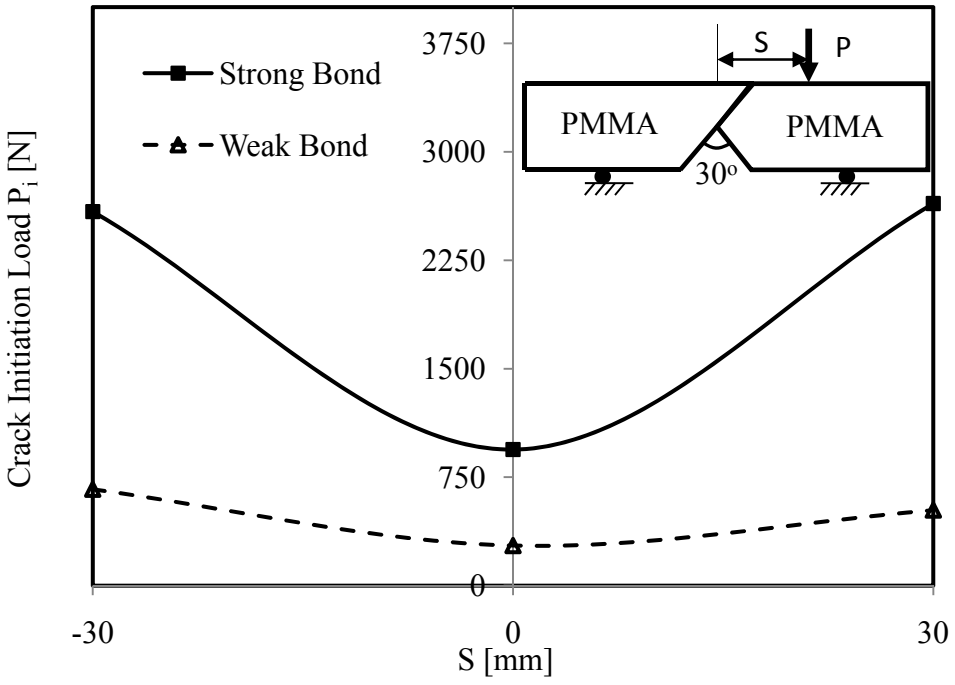

Fig. 3.22 Crack initiation loads loading points (S) for same-material PMMA systems with a notch angle of 30°

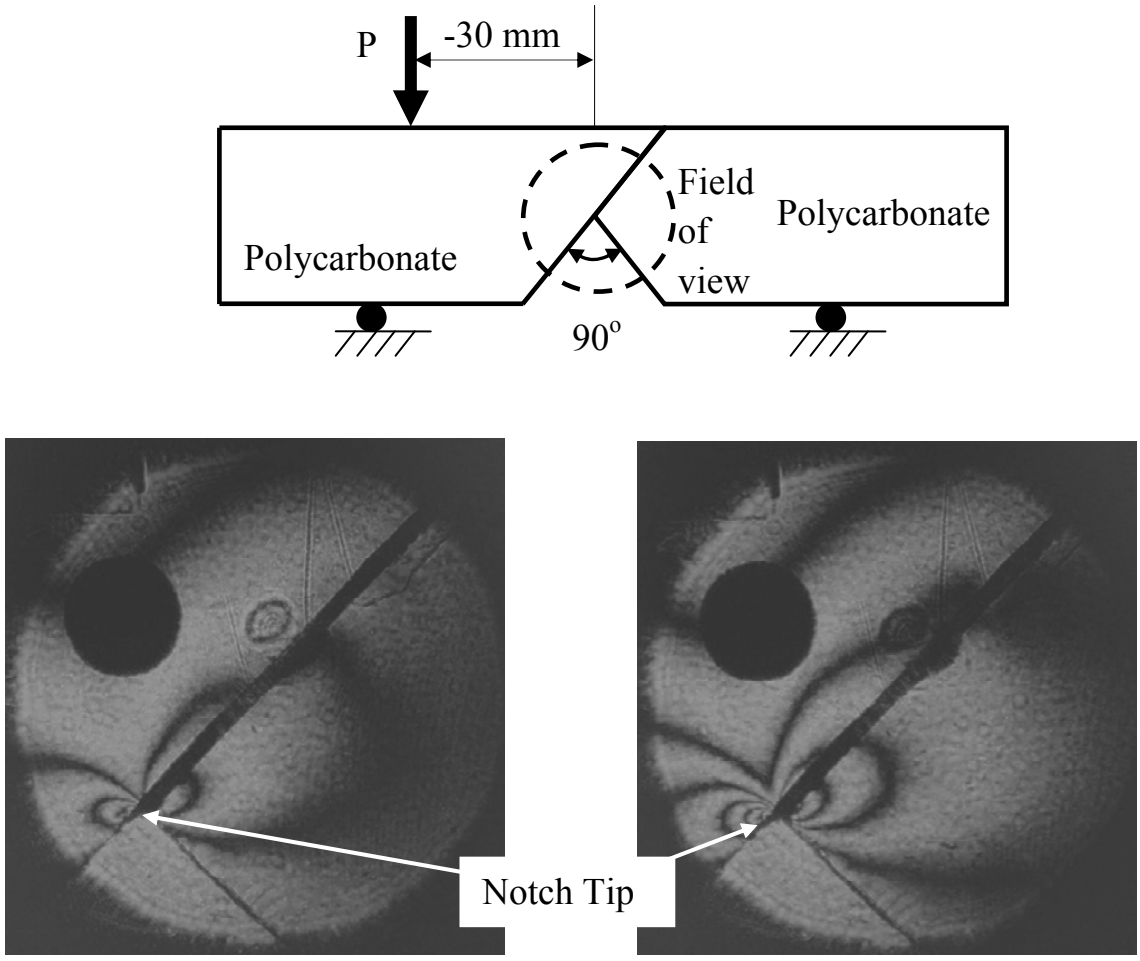

Fig. 3.23 Simulated (finite element) fringe patterns for same-material polycarbonate specimens with a notch angle of 90^{o} and load at S=-30 mm.

3.5 Results for bi-material systems

Bi-material systems have large stiffness mismatch due to the huge difference in elastic properties of the two components. Bi-material systems find applications in fiber reinforced composites, adhesive joints, micro-electronic devices with layered structures and others structures (Xu and Tippur, 1995). The presence of the oscillatory singularity (Sih and Rice, 1965; Comninou, 1977) makes this problem very different from the same-

material case. The Leguillon criterion can still be used to predict failure from notches for the bi-material case. This section presents results from experiments involving bi-materials. Similar to the previous section, the first part of this section describes the effect of the notch angle β on the crack initiation load. The second part describes the effect of the loading point S on the crack initiation load. The third part describes bi-material experiments with aluminum and polymer halves switched. Within each section, the differences between strong and weak bond are highlighted. Also, the results for the two different material types (PMMA and polycarbonate) are presented under each sub-section. The crack initiation loads from the experimental testing are provided in Table 3.6 for polycarbonate/aluminum specimens and in Table 3.7 for PMMA/aluminum specimens. Every data point in Tables 3.6 and 3.7 represents an average value from atleast three experiments.

Table 3.6 Average crack initiation loads for bi-material Polycarbonate/Aluminum specimens

Notch Angle / Bonding	S [mm]	30^0 [N]	90^0 [N]	120^0 [N]	Bonding tensile strength [MPa]	Bonding shear Strength [MPa]	K_{IC} [MPa $m^{1/2}$]
Weak	0	305	341	363	9.57	6.18	0.1
	30	877	809	837			
	-30	693	1113	1325			
Strong	0	439	362	553	11.35	10.18	0.09
	30	1205	671	932			
	-30	749	1151	2067			

Table 3.7 Average crack initiation loads for bi-material PMMA/Aluminum specimens

Notch Angle / Bonding	S [mm]	30^0 [N]	90^0 [N]	120^0 [N]	Bonding tensile strength [MPa]	Bonding Shear Strength [MPa]	K_{IC} [MPa $m^{1/2}$]
Weak	0	350	436	454	10.01	8.63	0.12
	30	775	834	918			
	-30	800	1209	1963			
Strong	0	479	335	522	12.85	10.16	0.14
	30	1152.5	830	1028			
	-30	610	1128	2335.5			

3.5.1 Design of bi-material systems

Bi-material systems made of polymer (PMMA or polycarbonate) and Aluminum were also made as shown in Fig. 3.24. The dimensions of these specimens are the same as the same-material specimens with the only change being the polycarbonate part being replaced by a stiffer aluminum part. The experimental preparation and testing of the bi-material specimens were identical to what has been discussed earlier in case of same-material specimens. The bonding strengths (tensile and shear) in case of bi-material specimens is lower than that in case of same-material specimens due to a mismatch in elastic properties in the constituent materials (aluminum and polymer). The ratio of the elastic moduli of aluminum to polymer is of the order of 17-24. This mismatch causes lower bonding strength and fracture toughnessess in case of bi-material systems. This creates a lower crack initiation load in bi-materials in comparison with same-material specimens.

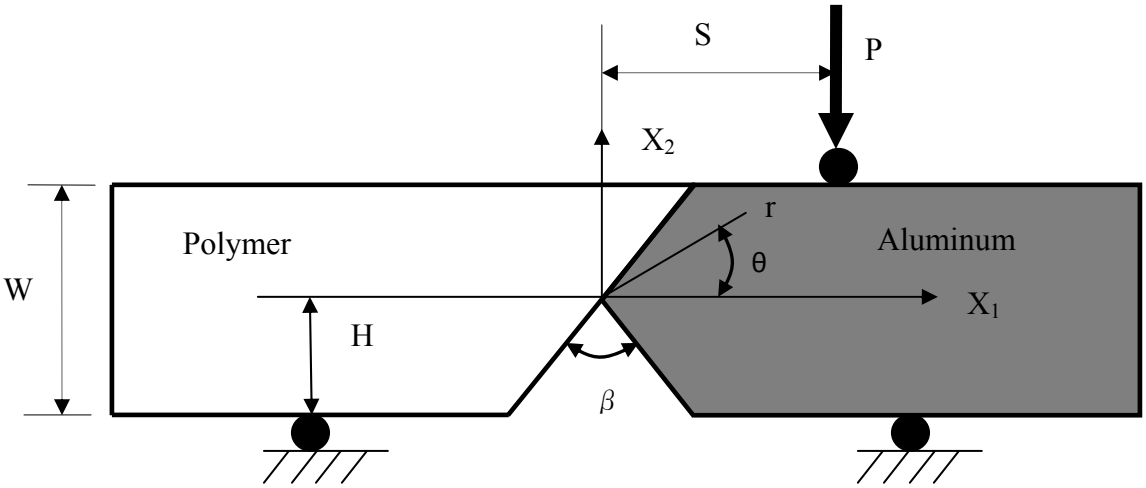

Fig.3.24 Schematic diagram representing bi-material notch-interface specimens

3.5.2 Effect of notch angle on bi-material crack initiation

The effect of the notch angle β on the crack initiation load P_i is shown in Fig. 3.25 for polycarbonate/aluminum and in Fig. 3.26 for PMMA/aluminum. The strongly bonded specimens show a higher load than the weakly bonded specimens as in case of same-material specimens for both material systems. The crack initiation load also increases with notch angle in both cases. But in case of notch angle of 90^o the initiation load always shows a decrease. This is observed in case of polycarbonate and PMMA specimens. The ratio of the shear stress to the normal stress can be calculated in radial coordinates for a given notch angle. This ratio is equal to 1 in case of notch angle of 90^o and is a possible reason for a decrease in load in case of bi-materials. The shear component becomes very high in case of a notch angle of 90^o and can cause a corresponding decrease in crack initiation load.

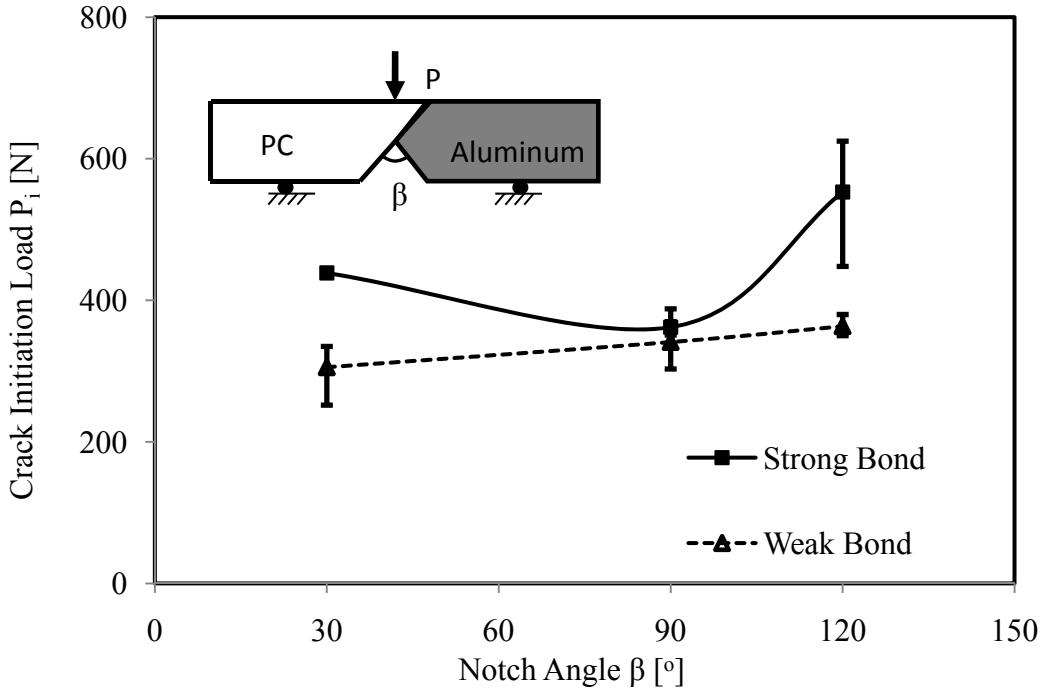

Fig. 3.25 Effect of notch angle on crack initiation load on bi-material polycarbonate/aluminum systems for S=0.

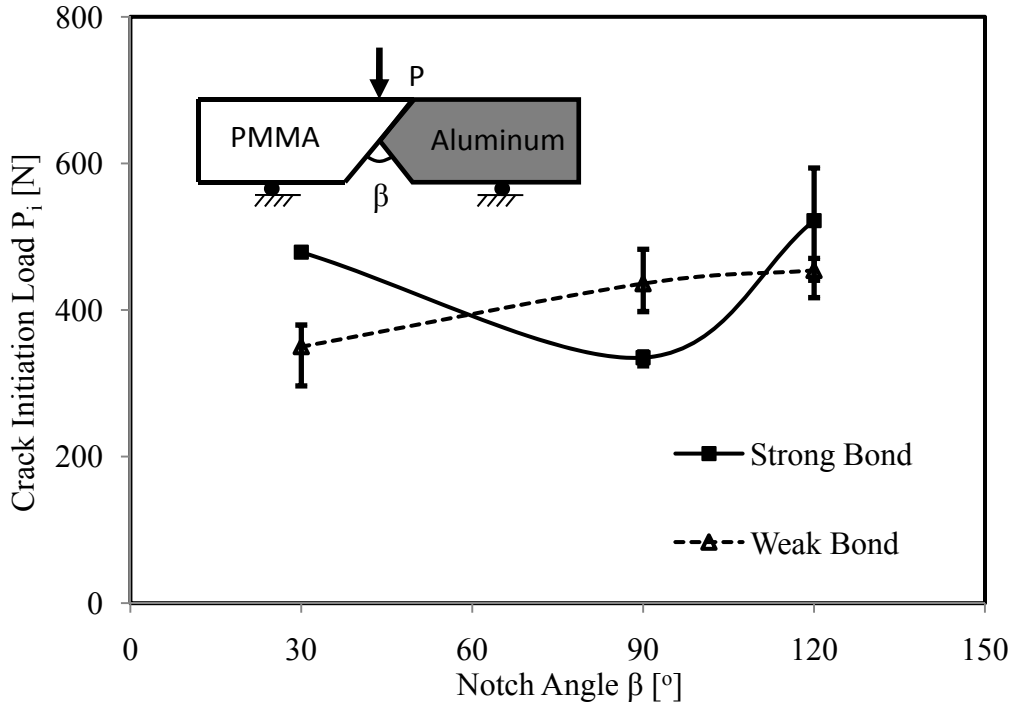

Fig. 3.26 Effect of notch angle on crack initiation load on bi-material PMMA/aluminum systems for S=0.

The crack propagation is very different for the different notch angles for strongly bonded PMMA/aluminum as shown in Fig. 3.27. While notch angles of 30^o and 90^o show crack propagation along the interface, notch angle of 120^o shows crack kinking into the bulk PMMA. The weakly bonded specimens for all cases show no crack kinking and the propagation is always along the interface. The failure is sudden and explosive in case of bi-material specimens. There were no frictional effects observed in case of the weakly bonded specimens.

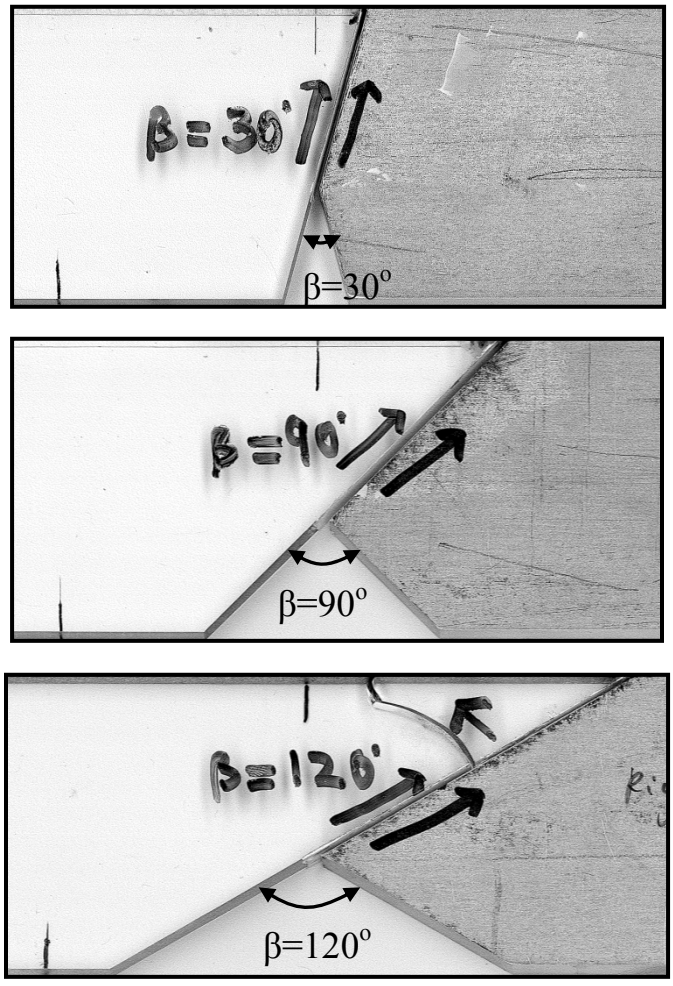

Fig. 3.27 Failure patterns for bi-material PMMA/aluminum specimens with S=0. Notch angles are illustrated in the pictures.

A typical load-displacement plot for a strongly bonded bi-material polycarbonate/aluminum specimen with a notch angle of 120^o and load at S=0 is shown in Fig. 3.28. The crack initiates along the interface at a load of about 600 N while the final failure happens only at a load of 2758 N.

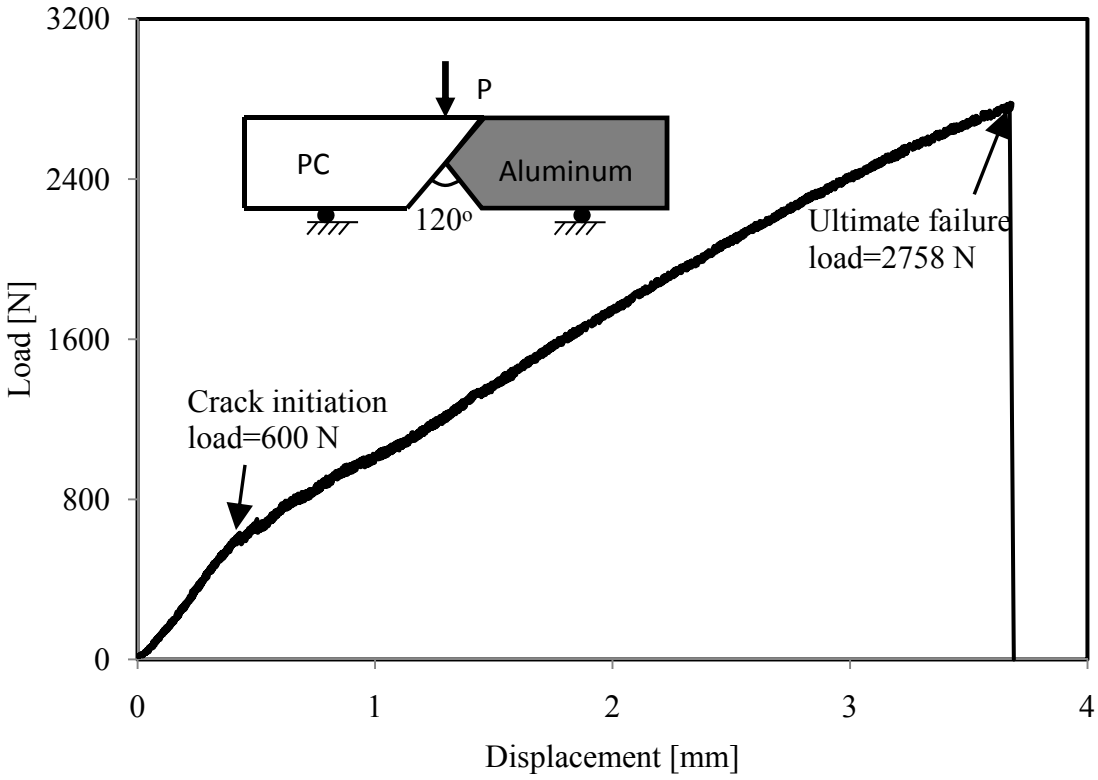

Fig. 3.28 Typical load-displacement plot for a strong bonded bi-material polycarbonate/aluminum specimen with a notch angle 120^o and S=0.

3.5.3 Effect of loading point on crack initiation loads

The loading point is varied from S=-30 to S=0 to S=30 (all in mm) for bi-material as well. The variation in crack initiation load with notch angle for the three different types of loading cases is shown for strongly bonded polycarbonate/aluminum specimens in Fig. 3.21 and for strongly bonded PMMA/aluminum specimens in Fig. 3.22.

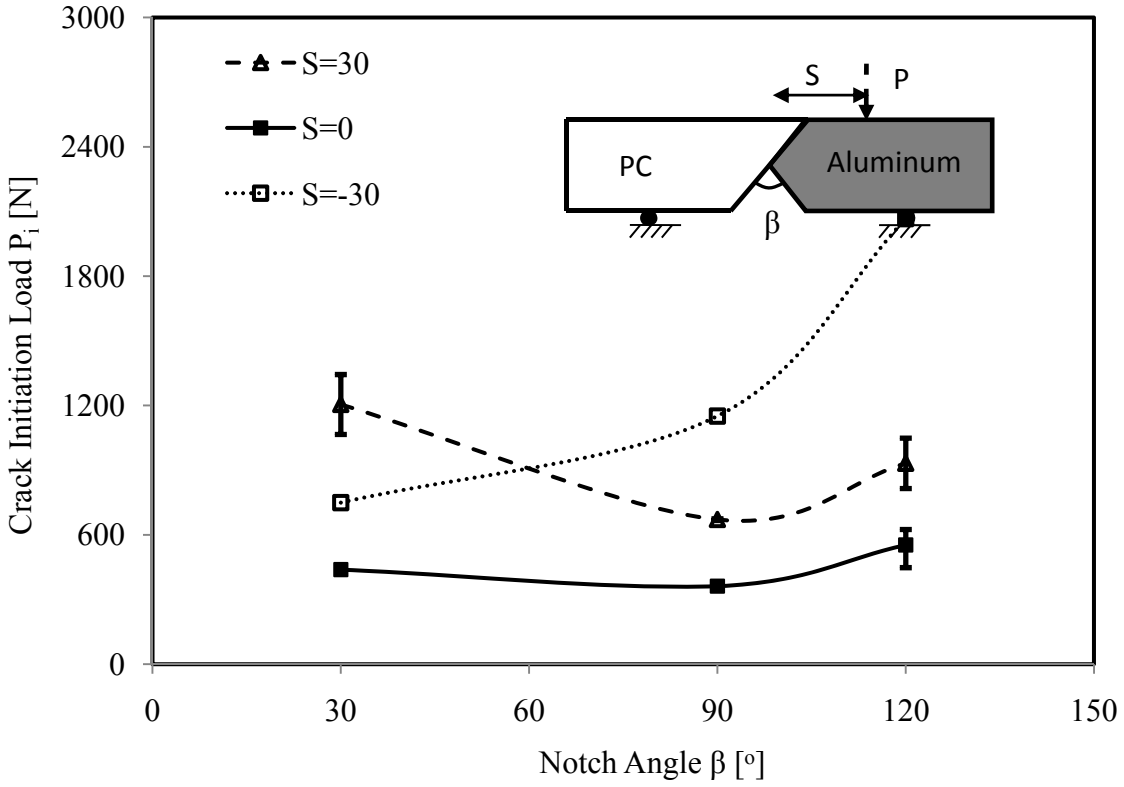

Fig. 3.29 Variation of crack initiation loads with notch angle for different loading points (S) for polycarbonate/aluminum bi-material strongly bonded systems.

It is seen that the changing the polymer from polycarbonate to PMMA does not have much effect on the crack initiation loads. Shifting the loading point away from the interface tends to produce the predicted effect. There is an increase in crack initiation load on moving the loading point from S=0 to either S=30 mm or S=-30 mm. There is also an increase in crack initiation load on increasing the notch angle. A notch angle of 90^o however shows little increase in the crack initiation load. It should be noted that the loading point is very close to the interface in case of this notch angle.

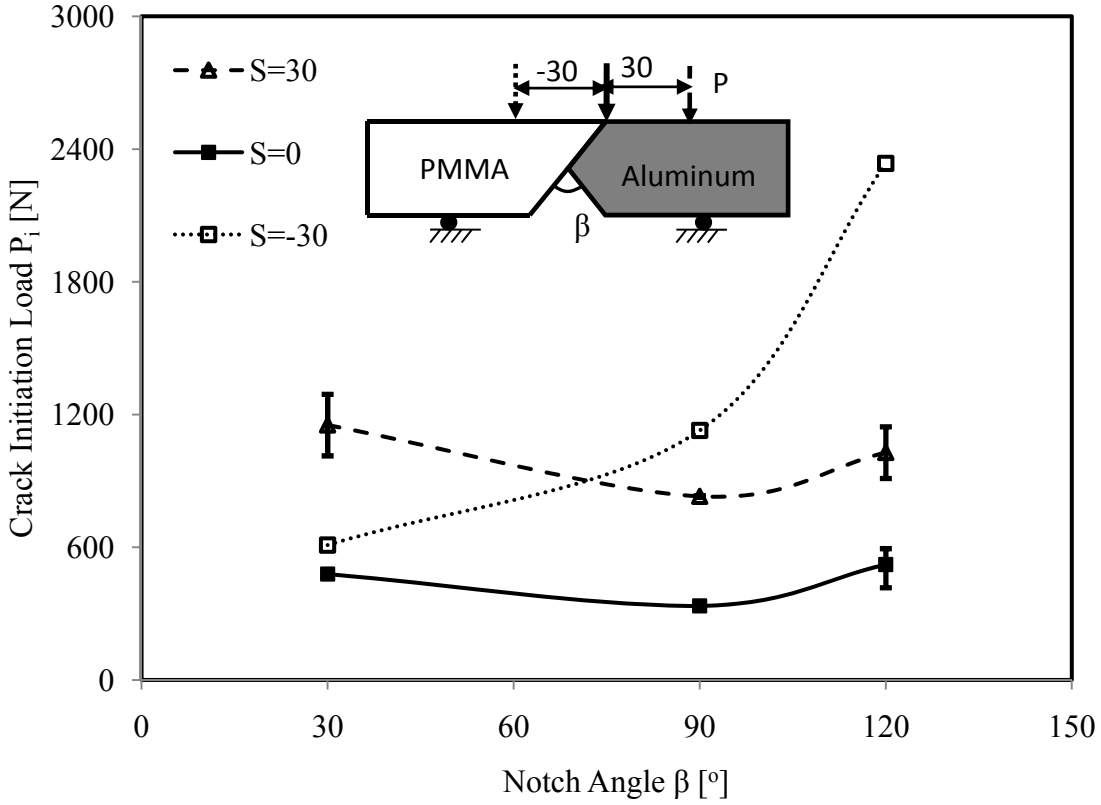

Fig. 3.30 Variation of crack initiation loads with notch angle for different loading points (S) for PMMA/aluminum bi-material strongly bonded systems.

3.5.4 Fringe patterns for bi-material systems

Fringe patterns were developed for strongly bonded polycarbonate/aluminum specimens with notch angle of 90^o and load at S=0 are shown in Fig. 3.31. The figure shows a series of pictures depicting the crack propagation from the notch tip. Since aluminum is not photoelastic, it appears opaque to the laser light. The final picture shows that the crack has propagated and there is a visible crack. This optical technique also allows for obtaining the correct crack initiation load which may not be got from the load-

displacement curve. The corresponding load-displacement curve for this same specimen is shown in Fig. 3.32.

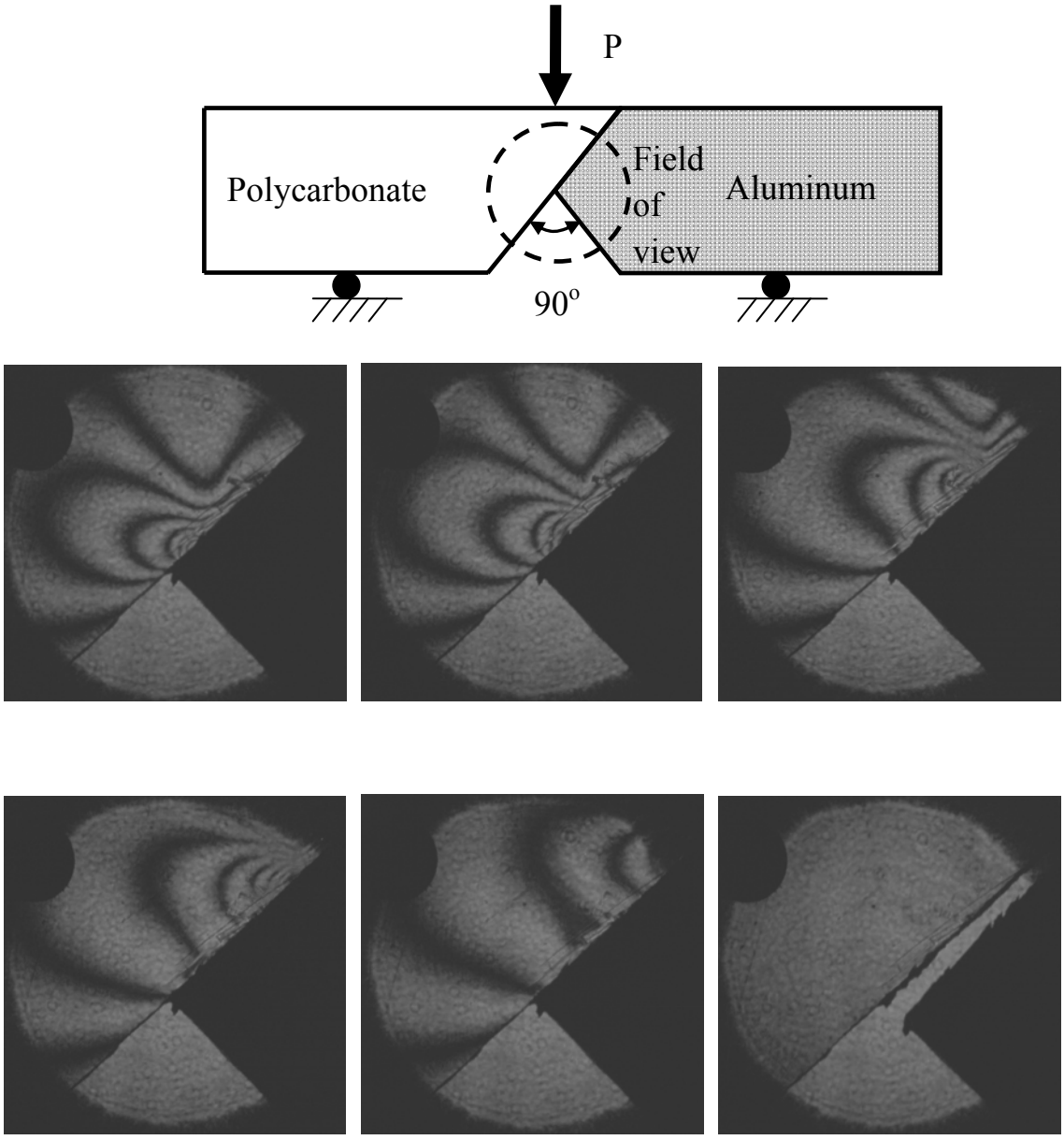

Fig. 3.31 Series of fringe pattern pictures showing crack propagation along the interface for weakly bonded bi-material polycarbonate/aluminum specimen with notch angle of 90^{o} and load at S=0.

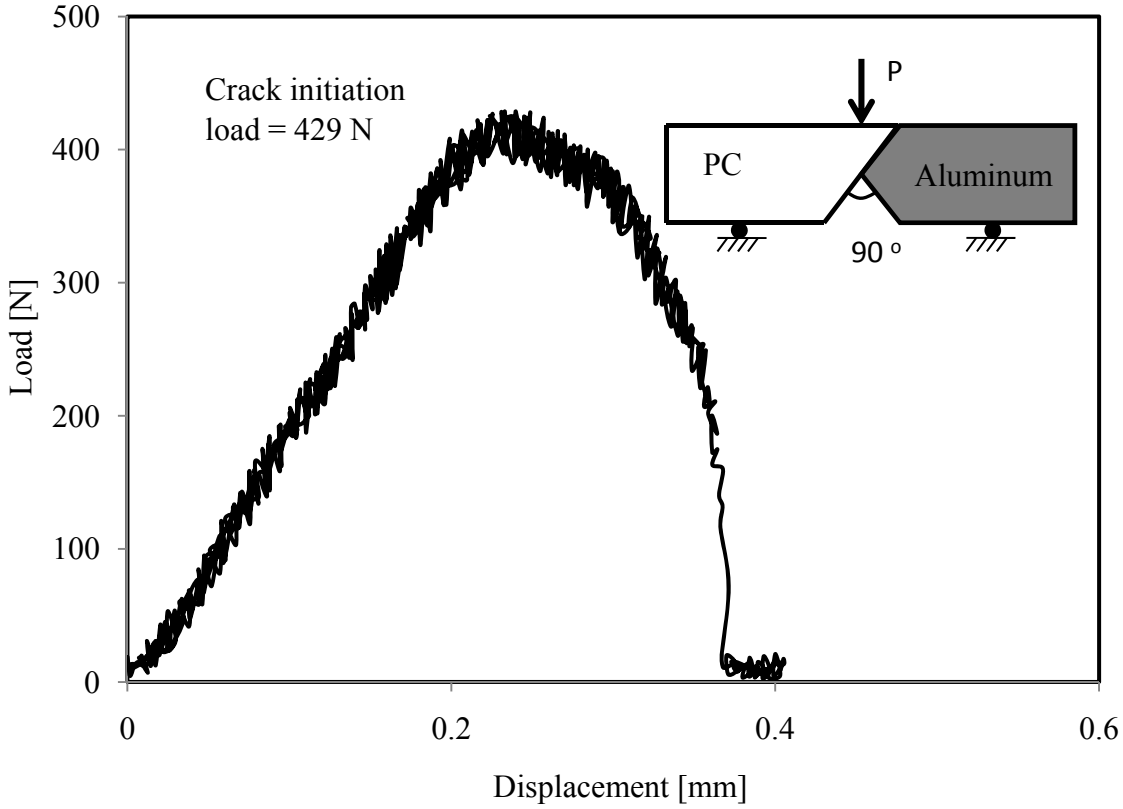

Fig. 3.32 Load-displacement plot for weakly bonded polycarbonate/aluminum specimen with notch angle of 90^{o} and loading at S=0. The fringe images are shown in Fig. 3.31 for this specimen.

3.5.5 Results for bi-material systems with aluminum/polycarbonate combination

Bi-material systems with a combination of aluminum/polycarbonate was tested in a similar three point bending experiment. The results for strongly and weakly bonded aluminum/polycarbonate with load at S=0 is presented in Fig. 3.25. The same is depicted in Fig. 3.26 but with the loading point shifted to S=30.

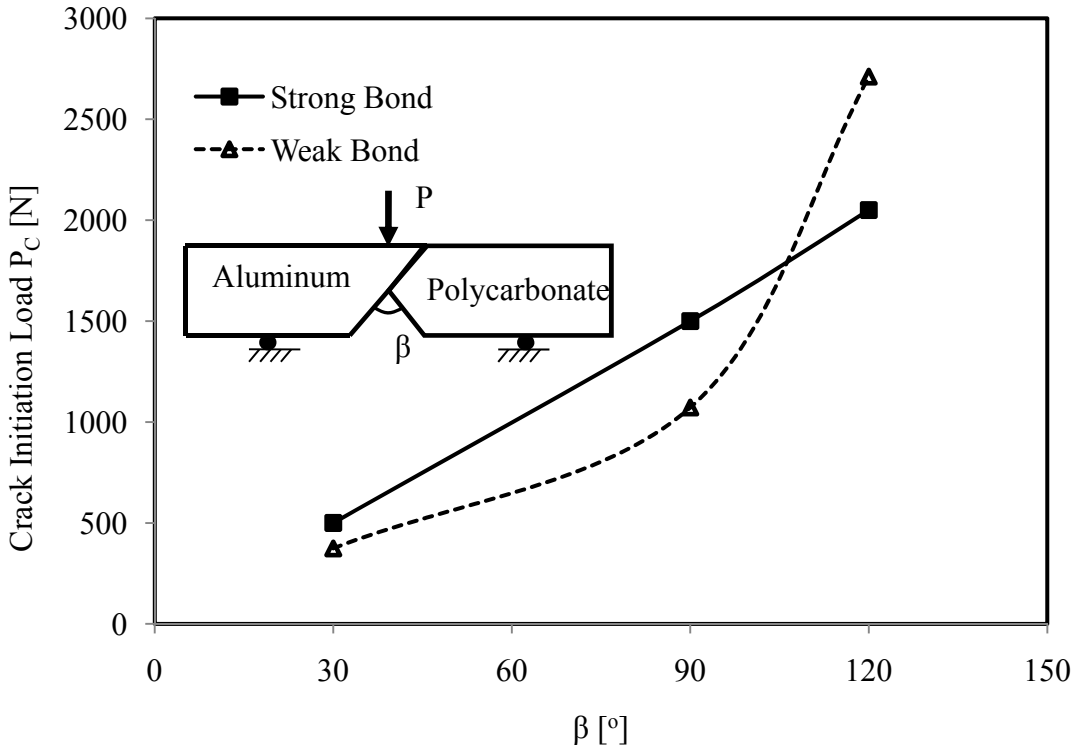

Fig. 3.33 Effect of notch angle on crack initiation load on bi-material aluminum/polycarbonate systems with load at S=0.

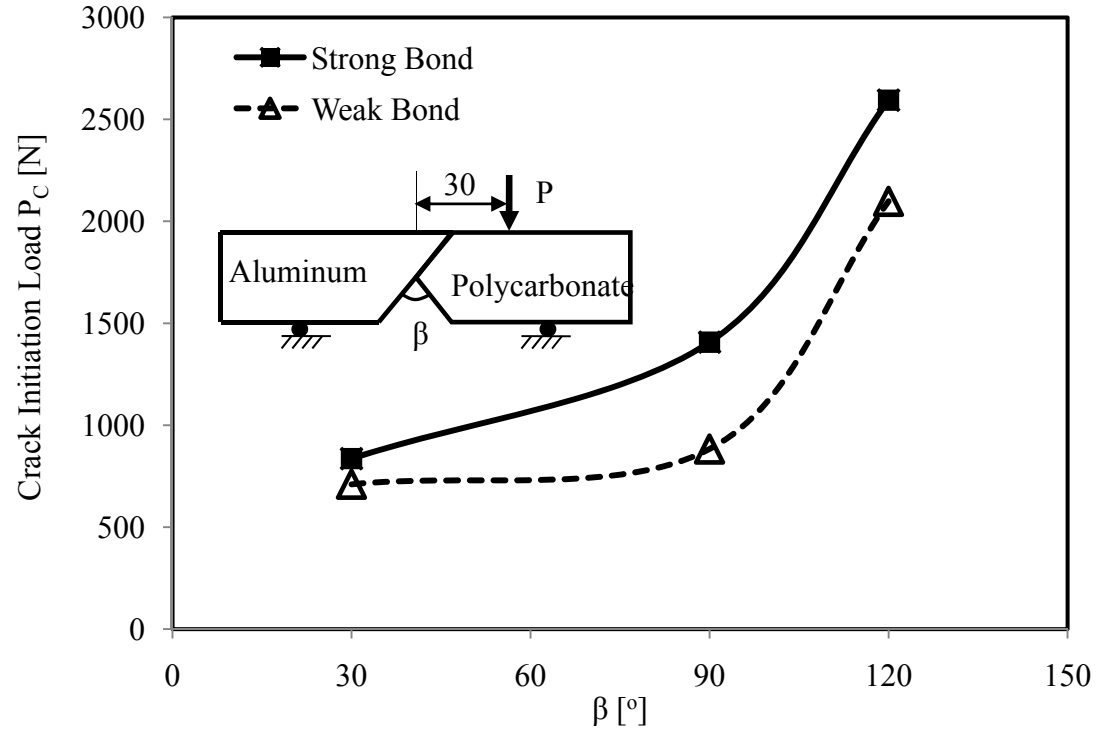

Fig. 3.34 Effect of notch angle on crack initiation load on bi-material aluminum/polycarbonate systems with load at S=30.

3.6 Conclusions

Systematic experiments were conducted to study the influence of an interface on notched specimens. These novel designs for notch interface specimens allow for validation with theoretical criterions. It was found that the notch angle and the loading point dominate the notch tip mode mixity and thereby control the crack initiation load. This was found to be true for both similar and dissimilar bonded materials. It was also found that higher bonding strengths lead to higher crack initiation loads. A systematic report of experimental results which will be useful for future computational simulations is presented (Krishnan and Xu, 2011c).

CHAPTER IV

EVALUATION OF DURABILITY AND DYNAMIC FAILURE OF MARINE COMPOSITES

4.1 Introduction

Polymer based composites are being used in naval construction and in underwater structures due to their higher stiffness and strength per unit weight in comparison with aluminum and titanium alloys (ONR fact sheet). Advanced defense platforms often require the use of light weight structures due to their increased mobility and lower fuel cost (Baucom et al., 2006). Polymer composites with glass reinforcements (Glass reinforced composites or GRP) are being increasingly used in marine structures including radomes, submarine casings, sonar casings, propellers, masts and shafts (Mouritz and Mathys, 1999). Vinyl ester and other types of polyesters are preferred over epoxy for use as matrix materials due to their low cost and ease of processing (Karbhari and Zhang, 2003). Similarly, E-Glass fibers are used in preference to carbon fibers due to the low cost and higher achievable ultimate strain levels. These two factors make E-glass fibers a better choice for naval composites despite their reduced tolerance to aqueous environments in comparison with carbon fibers (Karbhari and Zhang, 2003). The marine environment is very unique due to dynamic tidal loading and moisture which makes it very challenging to design composites. Constant exposure to moisture prone environments makes durability and dynamic failure properties critical for naval composite ships. It is important to ensure that marine composites do not degrade under constant exposure to sea water. But fiber composites with vinyl ester matrices have been

shown to lose interfacial mechanical properties due to hydrolysis reaction of unsaturated groups within the matrix resin (Kootsookos and Mouritz, 2004). However, many previous approaches and measurements have significantly underestimated the actual durability of a composite structure inside seawater. For a composite ship as shown in Fig. 4.1, a rectangular composite specimen, which is a part of an "infinite" large panel, only has one external face exposed to seawater.

During an underwater explosion, this front surface alone is subjected to shock loading first. It is only the front surface of a composite panel that will be directly exposed to seawater during the entire life time of the composite ship. Therefore, property degradation and damage from the front surface will be a major issue to determine the durability and life of the composite ship structure. However, almost all previous experiments have ignored this "single-surface environment effect". For example, Karasek et al. (1995) have evaluated the influence of temperature and moisture on the impact resistance of epoxy/graphite fiber composites. They found that only at elevated temperatures did moisture have a significant effect on damage initiation energy and that the energy required to initiate damage was found to decrease with temperature. Impact damage resistance and tolerance of two high performance polymeric systems was studied after exposure to environmental aging. For cross-ply laminates, the post-impact tensile strength values fell significantly (by maximum 70–75% of original composite strength) depending on ageing time, environment and impact velocity. Sala (2000) found that barely visible impact damage, due to the impact of 1 J/mm (for 2.2-mm laminate thickness) increased the moisture saturation level from 4.8% to 6% for aramid fiber-reinforced laminates and enhanced the absorption rate. Very recently, Imielinska and

Guillaumat (2004) investigated two different woven glass–aramid-fiber/epoxy laminates subjected to water immersion ageing followed by instrumented low velocity impact testing. The impacted plates were retested statically in compression to determine residual strength for assessment of damage tolerance. The delamination threshold load and impact energy absorption were not significantly affected by the absorbed water. Due to low fiber–matrix adhesion, the prevailing failure modes at low impact energy were fiber/matrix debonding and interfacial cracking. The compression strength suffered significant reductions with water absorbed (28%) and impact (maximum 42%). In addition to impact experiments, other mechanical experiments related to seawater durability also reported similar approaches using fully immersed composite specimens (Smith and Weitsman, 1996; Strait et al., 1992; Wood and Bradley, 1997; Weitsman and Elahi, 2000). In these previous specimens, property degradation such as matrix cracks in two vertical edges occurred, while these cracks never had the chance to initiate in a closed-edge, "infinite large" composite ship hull. Therefore, the previous data significantly underestimated the actual durability of composite structures inside seawater. Hence, a new "composite fish tank" approach is developed which will provide more accurate measurements for composite durability.

This chapter presents a combined experimental and numerical to evaluate the durability of marine composites. A novel experimental approach is developed to expose glass fiber/vinyl ester composites to sea water. The variation of compression-after-impact (CAI) strength is obtained as a function of time for 28 months. The impact induced damage in the composite is discussed. The damage mechanism in the vinyl ester composite due to sea water aging is explained using a reduced order multiscale

computational model. The experimental variation of CAI strength is captured using our numerical model.

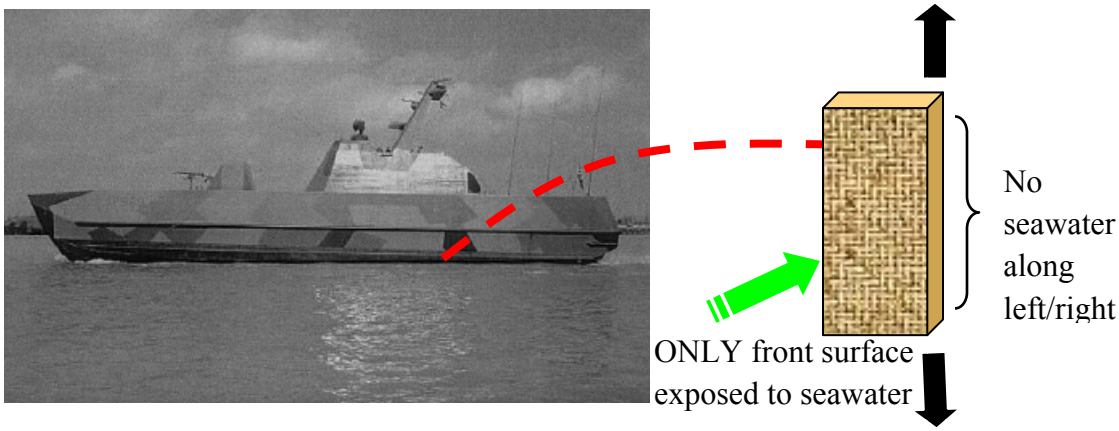

Fig. 4.1 A composite sample from a composite ship should represent the actual material and loading conditions--- its left/right sides and back surface are not exposed to seawater

4.2 Experimental investigations

4.2.1 Materials and sample preparation

Glass fiber reinforced vinyl ester (glass/VE) panels were produced using vacuum assisted resin transfer molding (VARTM) (Pillay et al., 2005). Eight layers of plain weave glass fabric (CWR 2400/50 plain weave, Composites One, LLC) were used to produce the panels with approximately 5 mm thickness which is required by ASTM D 7137 (Standard Test Method for Compressive Residual Strength Properties of Damaged Polymer Matrix Composite Plates). The fiber fraction of the panels was found to be 54% vol. after burn off testing was conducted. Compression after impact (CAI) testing samples with a dimension of 101.6 mm x 152.4 mm (4" x 6") were cut and machined to meet the strict dimension requirement specified in ASTM D 7137. The thickness of the

specimens had an average of 5 mm. Vinyl Ester is an alternative to polyester and epoxy materials in the making of composites and shows mechanical properties in between the other two. However, vinyl ester shows very good corrosion resistance to sea water and is a preferred choice for marine composites. Another advantage in using vinyl ester is the increased crack resistance during flexure of the naval structure.

Silicone rubber as an aquarium sealant (Perfecto Manufacturing, Noblesville, IN) was applied to the four slots of a base PMMA plate to bond the four composite specimens in the form of a fish tank. The sealant was also applied to the sides of the composite specimens to prevent any leakage of sea water. PMMA was chosen as the base plate as it has very little chemical reaction with seawater. Silicone rubber is used as a sealant since it provides enough bonding strength under water pressure, while at the same time, is not too strong to cause significant damage in the composite samples when the tank structure is dismantled for impact experiments. After one week of the construction of this tank (after full bonding strength is achieved), it was filled with synthetic seawater (Ricca Chemical Co., TX). Artificial seawater has a salinity content of about 2.9% and has a variety of salt constituents according to ASTM D1141 (Standard Practice for the Preparation of Substitute Ocean Water). The synthetic sea water is replaced at regular intervals of time and the water level (tank is filled to brim) inside each tank is maintained throughout the testing period. This tank is disassembled at specific time periods (at intervals of three to four months) to conduct impact and compression experiments (as shown in Fig. 4.3). Impact experiments were conducted on the dry specimens and on the wet specimens at regular intervals of time.

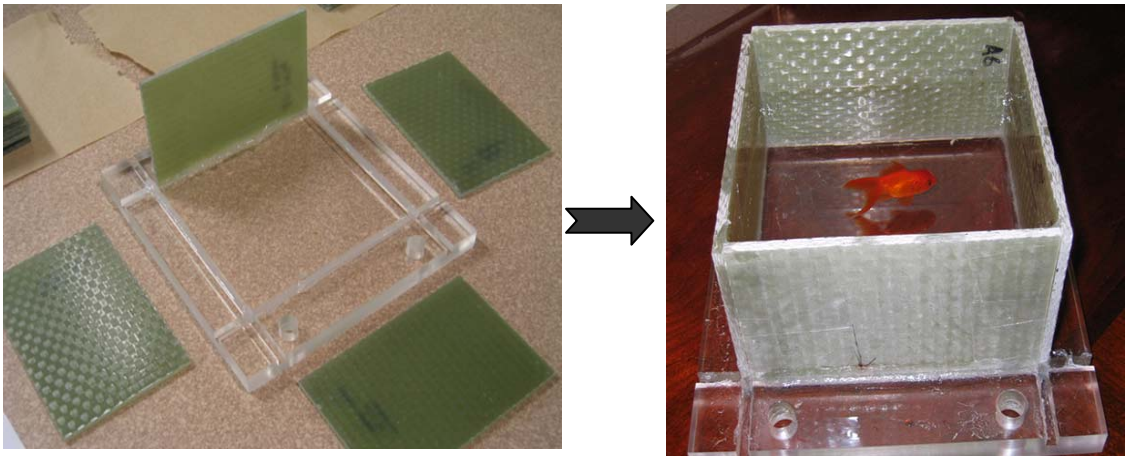

Fig. 4.2 A composite tank before construction (left) and after construction with seawater inside (right)

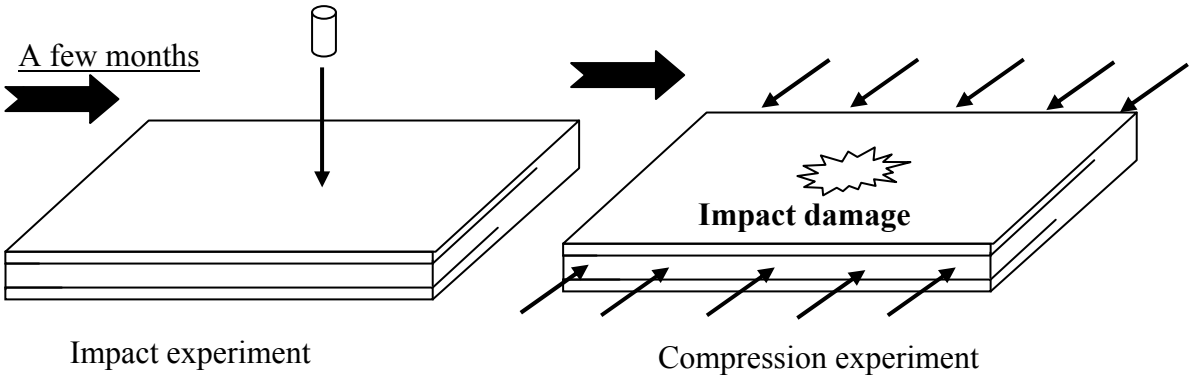

Fig. 4.3 Layered composite specimens subjected to out-of-plane impact and compression

4.2.2 Experimental methods involving impact tests

Impact damage was introduced using a drop tower setup (Ulven and Vaidya, 2006). All samples (fixed four edges) were subjected to an impact (60 joules impact energy) using a 16 mm (5/8") diameter hemisphere impactor. Damage zones of the impacted samples are clearly seen in Fig. 4.4(a), (b). For the front surface directly

subjected to impact, dark areas represent internal delamination, with possible several delaminations at the different interfaces. As discussed by Xu and Rosakis (2002), these delaminations are mainly shear-dominated so the interlaminar shear strength is an important parameter for delamination resistance characterization. Delaminations were nearly circular in shape with largest radius of 17.6 ± 1 mm observed between the back plies.

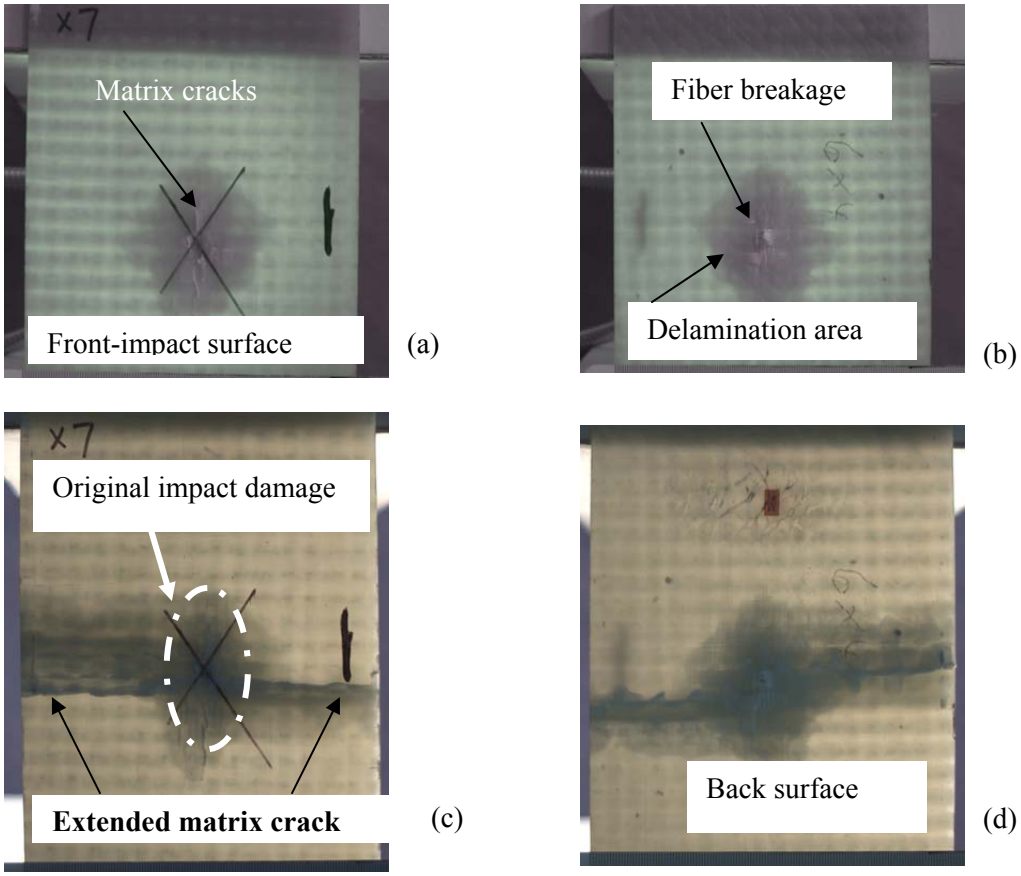

Fig 4.4. Typical impact damage on the front and back surfaces, (a) and (b), and typical compression failure of the impacted specimen (c) and (d)

Also, two major matrix cracks were observed near the impact site (as shown by two dark mark lines). One matrix crack was along the horizontal direction (35.8 mm ± 1

mm) and the other one was along the vertical direction (35.1 mm ± 1 mm). Immediately behind the drop weight impact site, fiber breakage was observed and this failure mode contributed to impact energy absorption. Significant kink banding was not observed in the experiments. Fiber/matrix debonding appeared as white thin lines on the back surface of the impacted specimens. These four major failure modes indeed make different contributions to the composite impact resistance (Abrate, 1998), and fiber breakage and delamination seem to play a major role in absorbing impact energy.

4.2.3 Compression tests for impacted specimens

Impacted samples were mounted in a compression-after-impact fixture. Strain gages were attached on the sample back and front surfaces to monitor the strain variations at both surfaces during compression. The reason to use strain monitoring is to avoid any global laminate buckling during compression because buckling failure leads to positive and negative strain readings from both surfaces, while a valid compression failure should lead to the same negative strains of both sides of the specimen. A loading rate of 1 mm/min was used. The progressive compression failure started from the impact damage as shown in Fig. 4.4. Initially, as the compression load increased, delamination from the previous impact propagated in a local buckling form (see more details by Kadomateas, 1999). Unlike impact-induced delamination, its propagation is mainly opening-dominated. It should be noted that delamination also appeared along the horizontal matrix crack and this matrix crack extended to the two edges as the compressive loading increased, as seen in Fig. 4.4. A shear crack near the horizontal matrix crack was observed as seen in Fig. 4.5. An inclined angle around 30-45 degrees (with respect to the compressive loading direction) was observed from the two vertical edges of the failed

specimen. These results are similar to previous compressive failure results by Tsai and Sun (2004), and Oguni and Ravichandran (2001). The final failure is controlled by sublaminate matrix buckling. A load-displacement curve is illustrated in Fig. 4.5 for a compressive experiment of an impacted specimen. The initial non-linear part is caused by the initial gap of the compressive fixture. Then a long linear load-displacement part was recorded. The failure mode starts from the opening delamination from the impacted-induced delamination (shear-dominated), followed by a sudden propagation of the longitudinal matrix crack and a final shear crack appeared along the specimen edge based on the recorded high-definition video. No significant kink-banding was observed in any of the specimens.

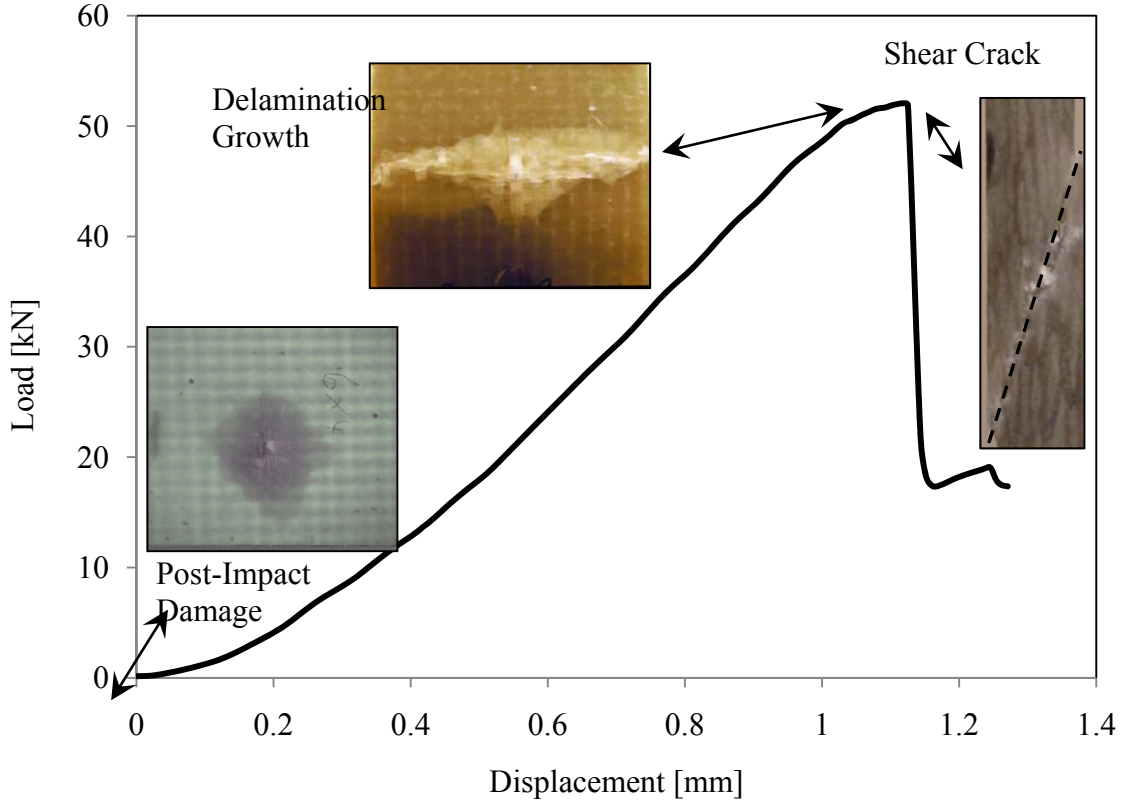

Fig. 4.5. A schematic load-displacement curve of an impacted marine composite laminate in compression

4.2.4 Results from experimental investigation

The results from the compression-after-impact (CAI) testing are presented in Table 4.1. The table shows the variation in CAI strength as a function of time for a time period of almost 30 months. Each compression-after-impact strength value is an average from 4-10 tested samples. The dry specimen strength of 133 MPa was used as a baseline for comparison. Since the CAI strength combines the effects of the seawater exposure and impact damage, it is very convenient to be used as a durability property plus the dynamic failure behavior. From the table, it is seen that the CAI strength reduction is less than 10% after one-year seawater exposure. This is much lesser than 40% as reported by Imielinska and Guillaumat (2004) on the same CAI experiments with similar composite materials. This comparison confirms that our new approach produces more reasonable data as our experiments simulate the right material conditions. The variation of CAI strength as a function of time is plotted in Fig. 4.6. The standard deviation from the measured values is also shown in the figure. A slight increase in CAI strength for the specimen after four-month seawater exposure is due to the specimen size effect. The average thickness of this set of specimens is at least 10 percent higher than other specimens. The CAI strength is not a material property as it is sensitive to the specimen size especially the specimen thickness (Kootsookos and Mouritz, 2004). After four-month seawater exposure, the CAI strength reduction has very small change up to 21 months, which might be related to seawater saturation inside the specimens. Since no additional seawater enters the composite specimens after a certain amount of time (Weitsman and Elahi, 2000), no new damage caused by seawater effect such as fiber-matrix interface strength reduction will occur. Therefore, the CAI strength of the wet specimen, which combines the effects of impact damage (not a function of seawater

exposure time), and the seawater damage (such as to the matrix), will have very small change in one to two years. Since there is no protective coating or painting on the composite plates, the future composite ship structures, which have strong coating or painting, should have excellent durability and dynamic failure properties. The CAI strength becomes relatively constant after a period of about 9.5 months. This is due to saturation in the composite specimens which will be discussed later.

The compressive failure during CAI testing is strongly dependent on sublaminate matrix buckling. The sublaminate buckling is shown to be proportional to the square of the specimen thickness. Consider the following equation which is used to explain the phenomenon of buckling in a column,

$$\sigma_{cr} = \frac{\pi^2 E}{(L/r)^2} \tag{4.1}$$

Here, σ_{cr} is the critical stress required to cause buckling, E is the modulus of elasticity, L is the unsupported length of the column and r is the smallest radius of gyration of the column. In case of sublaminate buckling, the critical buckling stress is proportional to the CAI strength of the specimens. Also, the unsupported length will be the length of the sublaminate matrix which will buckle and cause final failure. The radius of gyration in case of sublaminate buckling can be shown to be proportional to the thickness of the specimen as shown in equation 4.2.

$$r = \sqrt{\frac{I}{A}} \tag{4.2a}$$

$$I = \frac{1}{12} bt^3 \tag{4.2b}$$

$$A = bt \tag{4.2c}$$

Here, I is the moment of inertia, A is the area of that portion of the specimen under sublaminate buckling, b is the width of the specimen and t is thickness of the specimen. Substituting equation (4.2) into equation (4.1), it can be shown that the CAI strength is proportional to the square of the specimen thickness.

$$r = \frac{t}{\sqrt{12}} \tag{4.3}$$

It would be more reasonable to explain the variation in CAI/thickness^2 as a function of time. A graph of the variation of this quantity with time in months is shown in Fig. 4.7. There is an initial decrease in the dimensionalized CAI strength (from the dry values) followed by an increase when the specimens reach saturation.

Table 4.1. Variation of Compression-After-Impact (CAI) Strength with seawater exposure time

Time (months)	Mean CAI (Mpa)	% Reduction from dry strength
0	132.98 ± 7.59	0
4	140.40 ± 4.37	+5.58
9.5	121.39 ± 10.98	-8.72
13	125.63 ± 9.05	-5.53
18	128.15 ± 8.77	-3.63
22	122.22 ± 9.22	-8.09
25	122.18 ± 4.34	-8.12
28.5	119.15 ± 10.55	-10.4

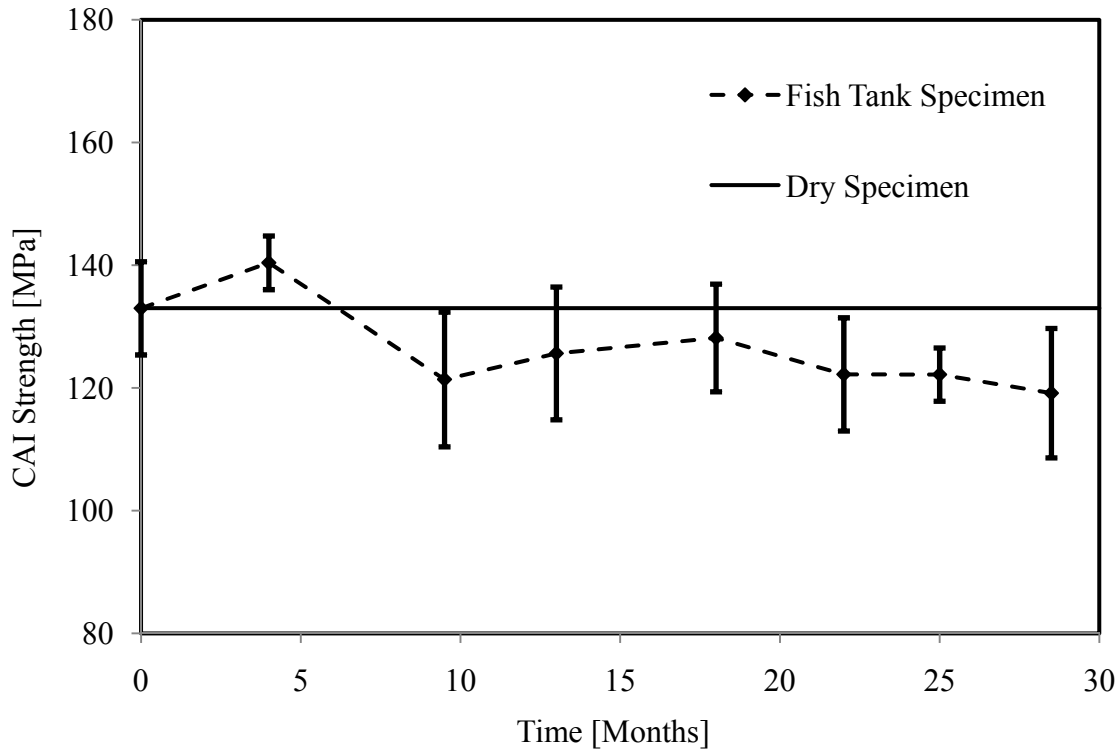

Fig. 4.6 Change in compressive strength (CAI) as a function of seawater exposure time

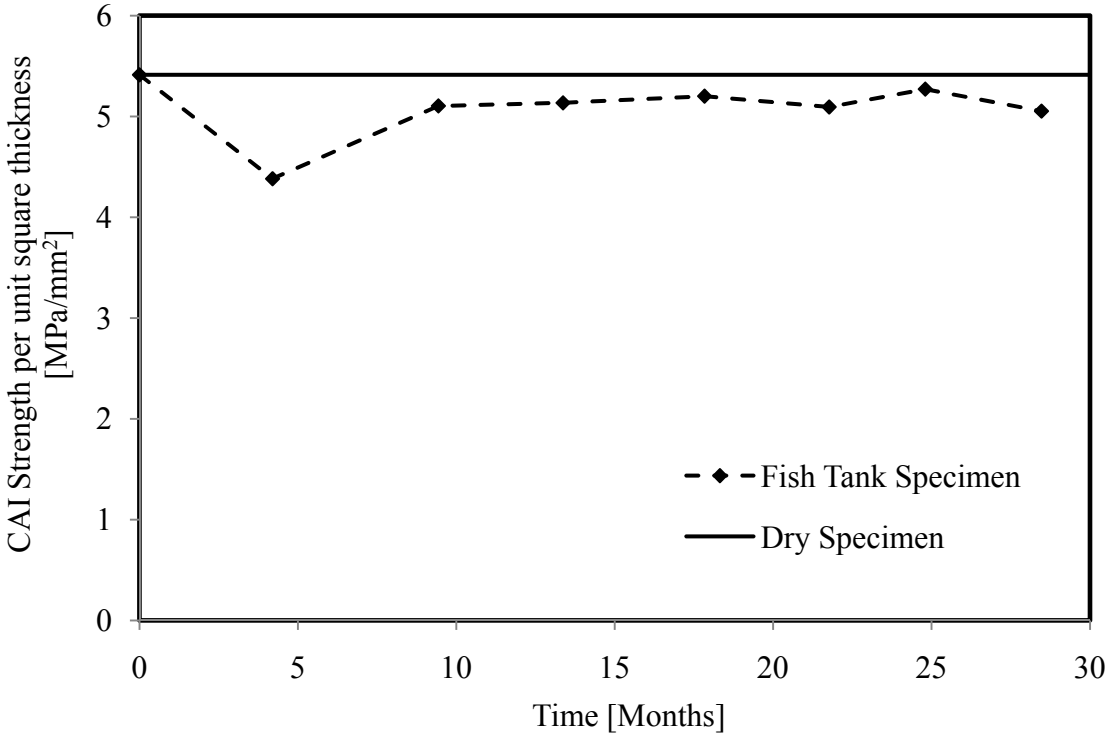

Fig. 4.7 Change in dimensionalized CAI strength as a function of seawater exposure time (months)

4.3 Numerical modeling of compression-after-impact

4.3.1 Moisture absorption in polymer composites

The ingress of moisture into polymers and composite materials is studied in order to predict the corresponding effect on the mechanical properties of the composite, matrix and fiber materials. There are numerous reports on sea water absorption in glass fiber reinforced polymer composites. The moisture absorption in glass/vinyl-ester composites and other similar systems with the same matrix have been observed to increase with time and ultimately reach saturation. While this behavior does not necessarily follow Fick's law, many previous researchers have assumed this behavior to follow Fick's second law of diffusion. Woven aramid-glass fiber/epoxy composites (Imielinska and Guillaumat, 2004), glass/vinyl ester, carbon/vinyl ester, carbon/epoxy, glass/epoxy (Murthy et al., 2010; Roy et al., 2001) and similar composite systems have moisture absorption curves assumed to obey Fick's law. Glass fiber reinforced polymer composites (GFRP) (Gellert and Turley, 1999) with different types of matrices and carbon fiber reinforced polymer composites (CFRP) have shown deviations from classical Fickian response. This acknowledges that there are supplementary moisture absorption mechanisms at play. Karbhari and Zhang (2003) report a two-stage diffusion processs in E-glass/vinylester composites under aqueous environments. In their case, there is an initial increase followed by a plateauing which is followed by a second increase in water absorption. The two-stage process is attributed to the entrapment and corresponding immobility of a portion of sea water within the polymer while the rest continues to diffuse. However, this report continues to assume the overall behavior to be Fickian. We assume a Fickian response for moisture absorption in the composite and matrix which has been commonly

assumed by previous researchers. Tsotsis and Weitsman (1994) present a simple graphical solution to calculate the diffusion parameters from a non-Fickian moisture absorption response for composites. Additionally, the response of neat vinyl ester resin has been assumed to be Fickian in nature by Sagi-Mana et al. (1998). Previous experimental results have been obtained from specimens immersed in sea water whereas our case deals with sea water exposure alone. Therefore, while the diffusion coefficient is expected to be the same as in existing literature, the time required for complete saturation will be more in case of exposure compared to immersion. Water absorption takes place at a faster rate at higher temperatures as has been reported by Liao et al. (1999). However, our case deals with water absorption at a normal temperature.

Fick's second law can be expressed as following.

$$\frac{\partial \phi}{\partial t} = D \frac{\partial^2 \phi}{\partial x^2} \tag{4.4}$$

where ϕ is the concentration of moisture, t is the time, x is position or length and D is the diffusion coefficient of the material. An approximate solution to Fick's second law in one-dimension can be expressed as

$$\frac{M_t}{M_\infty} = \frac{4}{\pi}\left(\frac{Dt}{d^2}\right)^{\frac{1}{2}} \tag{4.5}$$

Here, M_t is the mass of water uptake at time t, M_∞ is the mass of water uptake at time ∞, d is the 1-dimensional distance diffused by water. The diffusion coefficient is obtained from Murthy et al. (2010), who have used identical GFRP specimens, to be $2.1153 * 10^{-7}$ mm^2/s. Using this value, the time required for complete saturation for the thickness of the

E-Glass/VE composite (5 mm) can be calculated as 9 months. Our experimental data (Fig. 4.6) also seems to confirm this value of diffusion coefficient as there is little change in the value of CAI strength after the predicted saturation time of 9 months.

4.3.2 Degradation of material properties in matrix and fiber

The main role of the matrix in a high performance composite (like glass/vinyl ester) is to protect the sensitive fibers and to provide support local stress transfer from one fiber to another (Daniel and Ishai, 2005). However, the matrix has much lower strength and stiffness than the fibers and controls the final failure. Apicella et al. (1982, 1983) provide the only report on the elastic properties of the vinyl ester matrix. They present an increase in the elastic modulus of the polymer matrix due to loss of low molecular weight materials during hydrolysis. This increase in stiffness also causes more embrittlement in the matrix by plasticization due to water sorption. An increase in elastic modulus by 10% at a saturation percentage of 45 is reported by Apicella et al. (1983). The composite can be assumed to be homogenous when dry and when completely saturated. The partially saturated composite is assumed to be a combination of dry and saturated parts as shown in Fig. 4.8. It is acknowledged that a real composite will have a variation in elastic modulus at any given point depending on the saturation percentage. However, this is approximated by two-constituent model to understand the correlation in elastic modulus of the composite. A rule-of-mixtures would predict a linear increase in elastic modulus given the existing data at a saturation percentage of 45 is higher than the dry elastic modulus of the matrix. However, a linear assumption provides an

unreasonably high saturated elastic modulus value. Therefore, the saturated elastic modulus is assumed to taper off to a value 12 % higher than the dry value.

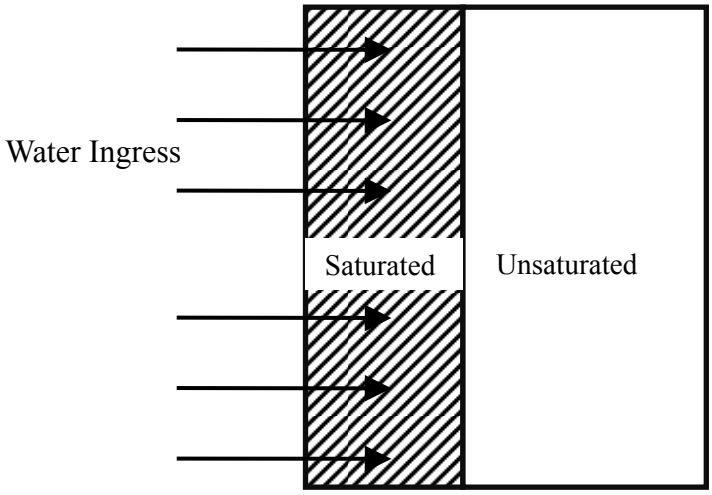

Fig. 4.8 Schematic diagram for model used to model elastic modulus of glass/vinyl ester composite

The variation of elastic modulus of the vinyl ester matrix with saturation percentage is assumed to be according to the following equation.

$$E = E_0 + \frac{\alpha s}{\beta + s} \tag{4.6}$$

where, E is the elastic modulus of the matrix at an overall composite saturation % of s and E_0 is the elastic modulus of the vinyl ester matrix, the parameters α (=0.4765 for our model) and β (=0.1687 for our model) are given as in equation (4.7).

$$\alpha = \frac{(s_t - 1)(E_0 - E_t)(E_{sat} - E_0)}{(E_t - E_0) + s_t(E_0 - E_{sat})} \tag{4.7a}$$

$$\beta = \frac{s_t(E_{sat} - E_t)}{(E_t - E_0) + s_t(E_0 - E_{sat})} \tag{4.7b}$$

where, s_t is the saturation percentage at time t, E_t is the elastic modulus of the matrix at time t, E_{sat} is the elastic modulus at saturation and E_0 is the dry elastic modulus of the matrix.

The only available data for the failure strains of the matrix are from Apicella et al. (1983) where the authors report a 57 percent decrease in failure strain at a saturation percent of 45. Based on this the tensile strain values, the tensile strength values are calculated assuming an elastic variation. The tensile strength of the matrix material is assumed to decrease with saturation percentage in an Arrenhius fashion according to following equation.

$$\sigma = \sigma_0 e^{(-\gamma s)} \tag{4.8}$$

where, σ is the tensile strength of the vinyl ester at a saturation % of s and σ_0 is the tensile strength of the dry matrix material, and γ (=0.5938 in our model) is a model parameter given as in equation (4.9).

$$\gamma = \frac{1}{s_t} \log\left(\frac{\sigma_0}{\sigma_t}\right) \tag{4.9}$$

where, σ_t is the tensile strength at time t and at a saturation percent of s_t and σ_t is the tensile strength of the dry matrix. The variation of elastic modulus and tensile strength of the matrix as a function of saturation percent is shown in Fig. 4.9. Equations (4.6) and (4.8) are used to plot these curves.

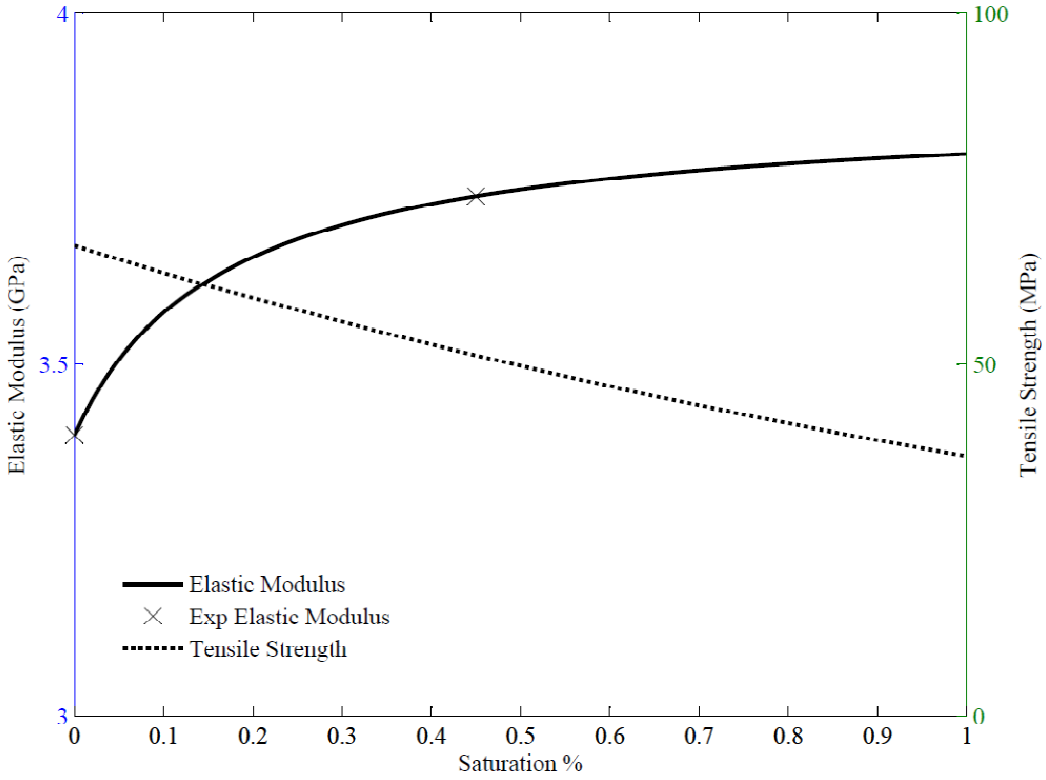

Fig. 4.9 Variation in matrix elastic modulus and tensile strength with sea water saturation percentage

Existing experimental data (Apicella et al., 1983) indicate only the degradation in tensile strength. The compressive strength of the matrix is assumed to degrade in a similar fashion as the tensile strength. The rationale for this is explained here. The degradation in strength happens due to the presence of voids which occur due to hydrolysis of matrix material. This can be modeled as a single cubical element with a spherical void at the center. This model is updated with material and damage parameters, and is subject to tensile and compressive strength. The tensile strength at a given void ratio is compared with the tensile strength of the model without the void. This is then compared with the compressive strength of the model with and without the void. The

decrease in both the compressive and tensile strengths is found to be the same. Therefore, the degradation in compressive strength of the matrix is assumed to be in similar fashion as the degradation in tensile strength.

There are few reports on the material degradation in E-glass fibers. Ramirez et al. (2008) present an equation for the degradation in tensile strength of E-glass fibers exposed to sea water. This equation has been fit to experimental data. However, this relation gives the degradation in tensile strength in terms of time of saturation whereas percentage saturation would be a better measure. There has been reported damage to the E-glass fiber and corresponding stress corrosion knee by Metcalfe and Schmitz (1972), Matthewson (1993) and Liao et al. (1999). However, the current investigation assumes no change in material properties of E-glass fibers after sea water exposure. It is acknowledged that there will be minor degradation in the fibers on sea water exposure. However, the change in elastic modulus or tensile strength of the fibers will not be so high as to cause significant changes to sublaminate buckling. The matrix sublaminate strength and hence the ultimate CAI strength will only show minimal changes if there is small change in the fiber properties. Therefore, the elastic modulus and tensile strength of the fiber are assumed to be undamaged throughout the entire saturation process. The elastic modulus of the vinyl ester is determined to be 3.4 GPa (Tekalur et al., 2008) and that of the fiber is found to be 70 GPa (Roy et al., 2001). The tensile and compressive strength of the vinyl ester matrix are obtained from the Derakane 3090 material property sheet as 69 MPa and 110 MPa respectively. The values of tensile and compressive strengths of the vinyl ester matrix for the RVE scale simulations are taken to be 67.8 MPa and 117.1 MPa. The saturated matrix elastic modulus is calculated from our model

(equation (4.6)) as 3.8 GPa. The tensile and compressive strength of the saturated vinyl ester matrix are calculated as 37.7 MPa and 58 MPa respectively.

4.3.3 Composite material properties

The properties of the composite material are calculated using a finite element model for a representative volume element (RVE) of size 10 mm x 12.5 mm x 0.625 mm. This RVE contains the matrix, and fiber in fill and warp directions. Let $\omega_{ph}^{(\gamma)}(\mathbf{x},t)$ be a scalar variable indicating the amount of damage in the constituent γ (which can be m, f or w for matrix, fiber fill direction and fiber warp direction respectively). Then we have,

$$\omega_{ph}^{(\gamma)}(\mathbf{x},t) = \phi_{ph}(\kappa_{ph}^{(\gamma)}(\mathbf{x},t)); \frac{\partial \phi_{ph}(\kappa_{ph}^{(\gamma)})}{\partial \kappa_{ph}^{(\gamma)}} \geq 0 \tag{4.10}$$

In which, $\kappa_{ph}^{(\gamma)}$ is expressed as

$$\kappa_{ph}^{(\gamma)}(\mathbf{x},t) = \max_{\tau \leq t}(\nu_{ph}^{(\gamma)}(\mathbf{x},\tau)) \tag{4.11}$$

Where $\nu_{ph}^{(\gamma)}$ is phase damage equivalent strain defined based on the strain-based damage theory (Simo et al., 1987) as

$$\nu_{ph}^{(\gamma)}(\mathbf{x},t) = \sqrt{\frac{1}{2}\left(\mathbf{F}^{(\gamma)}\hat{\boldsymbol{\varepsilon}}^{(\gamma)}\right)^T \hat{\mathbf{L}}^{(\gamma)}\left(\mathbf{F}^{(\gamma)}\hat{\boldsymbol{\varepsilon}}^{(\gamma)}\right)} \tag{4.12}$$

In which $\hat{\varepsilon}^{(\gamma)}$ is the vector of principal components of the average strains $\varepsilon_{ij}^{(\gamma)}$ within constituent phase γ; $\hat{\mathbf{L}}^{(\gamma)}$ the tensor of elastic moduli in principal directions of $\varepsilon_{ij}^{(\gamma)}$ and

$\mathbf{F}^{(\gamma)}$ the weighting matrix. The weighting matrix differentiates between damage accumulation when under tension or compression.

$$\mathbf{F}^{(\gamma)}(\mathbf{x},t) = diag\left(h_1^{(\gamma)}, h_2^{(\gamma)}, h_3^{(\gamma)}\right) \tag{4.13}$$

$$h_\xi^{(\gamma)}(\mathbf{x},t) = \frac{1}{2} + \frac{1}{\pi}\text{atan}\left(c_1^{(\gamma)}\hat{\varepsilon}_\xi^{(\gamma)}\right); \xi = 1,2,3 \tag{4.14}$$

Where $c_1^{(\gamma)}$ represents the contribution of tensile and compressive loadings in the principal directions, and *diag(.)* denotes diagonal matrix.

Damage in the constituent materials is assumed similar to Yan et al. (2010). The phase damage evolution function follows an arctangent law as shown below.

$$\phi_{ph}^{(\gamma)} = \frac{a\tan(a_{ph}^{(\gamma)}\kappa_{ph}^{(\gamma)}(\chi,t) - b_{ph}^{(\gamma)}) + a\tan(b_{ph}^{(\gamma)})}{\pi/2 + a\tan(b_{ph}^{(\gamma)})} \tag{4.15}$$

Here, $a_{ph}^{(\gamma)}$ and $b_{ph}^{(\gamma)}$ are material parameters which are functions of saturation percentage. The values of $a_{ph}^{(\gamma)}$ and $b_{ph}^{(\gamma)}$ are found for the dry matrix and fiber in fill and warp directions and are indicated in Table 4.2. The value of $a_{ph}^{(m)}$ is independent of saturation percentage and is maintained constant at 400. However, the value of $b_{ph}^{(m)}$ varies as a function of saturation percentage. This value is calculated for various saturation percentages at different values of elastic modulus and tensile strength to obey the arctangent damage model. The material parameter $b_{ph}^{(m)}$ is found to vary with saturation percentage s, according to the equation presented below.

$$b_{ph}^{(m)} = 0.005s^2 - 1.5s + 210 \tag{4.16}$$

The description of the averaging of the RVE (macroscale) stress and strain of the overall woven composite is provided in Yan et al. (2010). A similar approach is used in our work as well.

Table 4.2 Calibrated strength parameters for fiber in fill (f) and warp (w) directions and for matrix (m) in dry composite.

$a_{ph}^{(f)}$	$b_{ph}^{(f)}$	$c_1^{(f)}$	$a_{ph}^{(w)}$	$b_{ph}^{(w)}$	$c_1^{(w)}$	$a_{ph}^{(m)}$	$b_{ph}^{(m)}$	$c_1^{(m)}$
1.5	2.3	5.0	1.0	2.0	-28.0	400	212	15

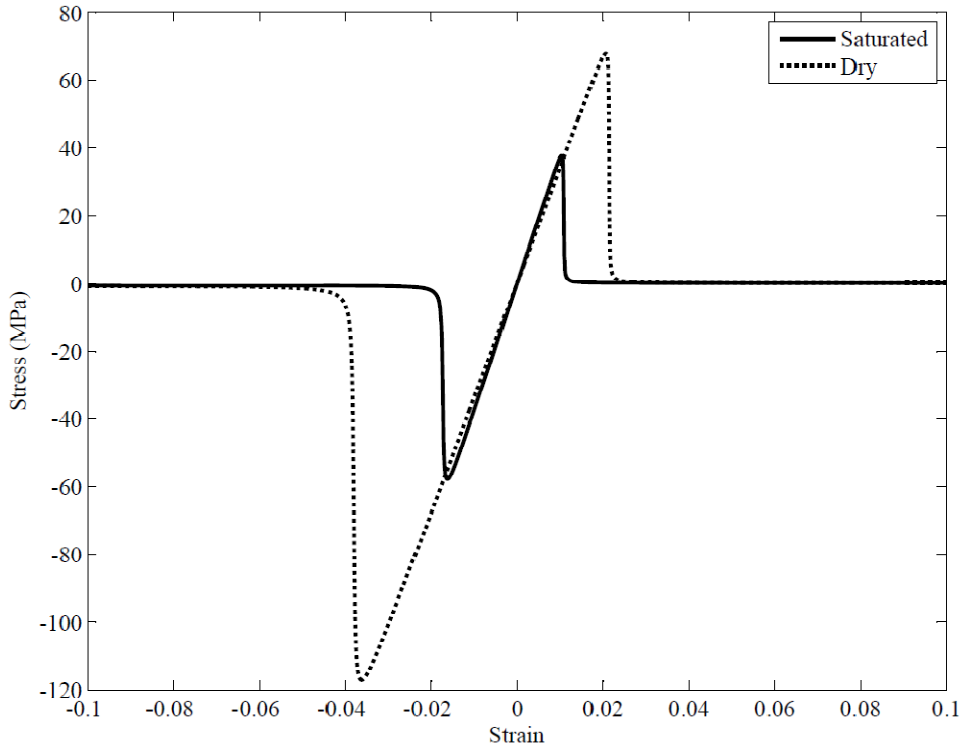

Fig. 4.10 Stress-strain diagram showing different material properties for dry and saturated vinyl ester matrix.

4.3.4 Calibration of undamaged material properties

The multiscale model defining failure in the plies has 9 material failure parameters including $a_{ph}^{(\gamma)}$, $b_{ph}^{(\gamma)}$, $c_1^{(\gamma)}$ with γ=m,w,f for matrix, fiber warp and fiber fill directions respectively. The The calibrated strength parameters for the matrix and fiber in the fill and warp directions are listed in Table 4.2. The properties of the fiber in the fully saturated (99.9 %) composite are taken to be the same as in the dry (0 %) composite. The matrix properties in fully saturated composite are calculated to be $a_{ph}^{(m)}$=400, $b_{ph}^{(m)}$=112, $c_1^{(m)}$=25.

The dry and the saturated stress-strain curves for the saturated and dry vinyl ester matrix are shown in Fig. 4.10. The positive values represent the tension direction and the negative values represent the compression direction. These values can then be used to obtain the composite stiffness values based on the linear-elastic computational homogenization method as outlined in Guedes and Kikuchi (1990). The stress-strain response of the overall composite computed using unit cell simulations is shown in Fig. 4.11 for the dry composite and in Fig. 4.12 for the completely saturated composite. In these two figures, the tension and compression response in the warp and fill directions of the composites are indicated. The values obtained from this are compared with experimentally obtained values as shown in Table 4.3.

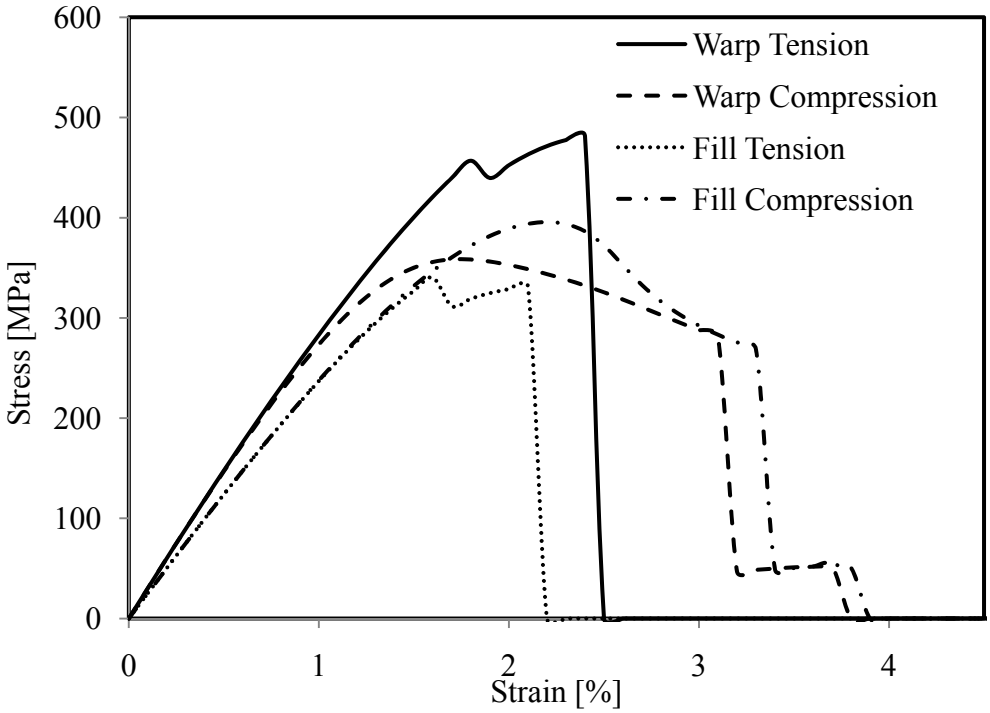

Fig. 4.11 Stress-strain response of the dry composite RVE along the fill and warp directions under tension and compression

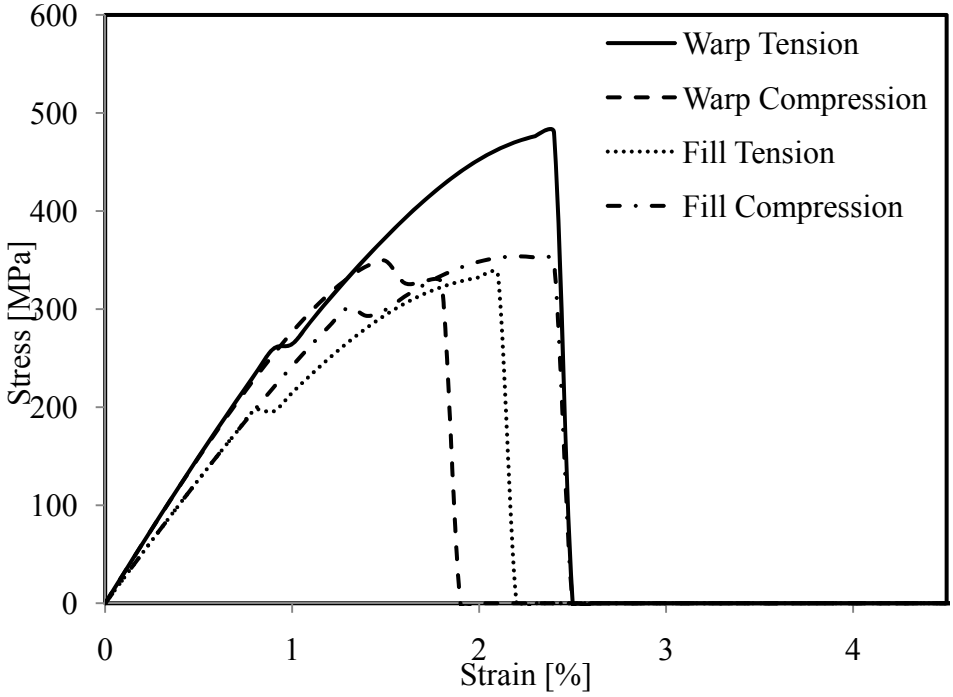

Fig. 4.12 Stress-strain response of the saturated composite RVE along the fill and warp directions under tension and compression

Table. 4.3 Strength properties of composite materials provided by experiments and RVE scale simulations

Composite Properties	Dry		Saturated	
	Experiments	Simulations	Experiments	Simulations
Compressive Strength				
Warp Direction	363.4 (75.0)	358.4	No data	349.1
Fill Direction	336.2 (25.2)	395.7	No data	335.3
Tensile Strength				
Warp Direction	512.5 (22.5)	481.5	478.3 (30.3)	480.1
Fill Direction	350.9 (8.9)	340.1	377.6 (51.3)	353.9

The experimental values of the strength paramaters presented in Table 4.2 for the dry composite are obtained from Tekalur et al. (2008). The experimental tensile strength values for the saturated case are obtained from Karbhari and Zhang (2003) and for the com. It is seen that while the compressive strength parameters of the composite show degradation after saturation, the tensile strength show little or no degradation. The interlaminar failure between composite laminates is modeled using cohesive surfaces which is described in more detail in Yan et al. (2010). The cohesive surface model includes seven parameters along the normal and shear directions which are related to the equivalent Young's and shear moduli within the interface region.

4.3.5 Numerical simulation of environmentally aged CAI response

The response of the glass/vinyl ester composite exposed to sea water aging as a function of time is discussed in this section. The dry and the saturated composite samples

have all the eight plies with the same material properties. However, in case of unsaturated samples the plies have different properties depending on the saturation levels in each of them. This saturation level in each ply is determined using Fick's equation by taking the average of the saturation percentage at the ends of the each ply. The corresponding ply is then assigned its material property based on the model for its constituents described earlier. The saturation percentages at different time periods in the various plies of the composite are as shown in Table 4.4. Here Ply 1 denotes the ply closest to exposed side of the composite and Ply 8 is the side farthest from the sea water. The finite element model of the E-glass/vinyl ester composite is shown in Fig. 4.13.

Table 4.4 Variation of saturation percentage [%] in the different plies with time in months.

Time [months]	Ply1	Ply2	Ply3	Ply4	Ply5	Ply6	Ply7	Ply8
1	100	100	94.6	78	60.2	49	41.4	35.8
2	100	100	100	94.5	75.6	63	54	47.3
3	100	100	100	100	96.3	84.9	71.7	62
4	100	100	100	100	100	94.6	82.8	71.6
5	100	100	100	100	100	99.6	85.4	74.7
8	100	100	100	100	100	100	100	94.5

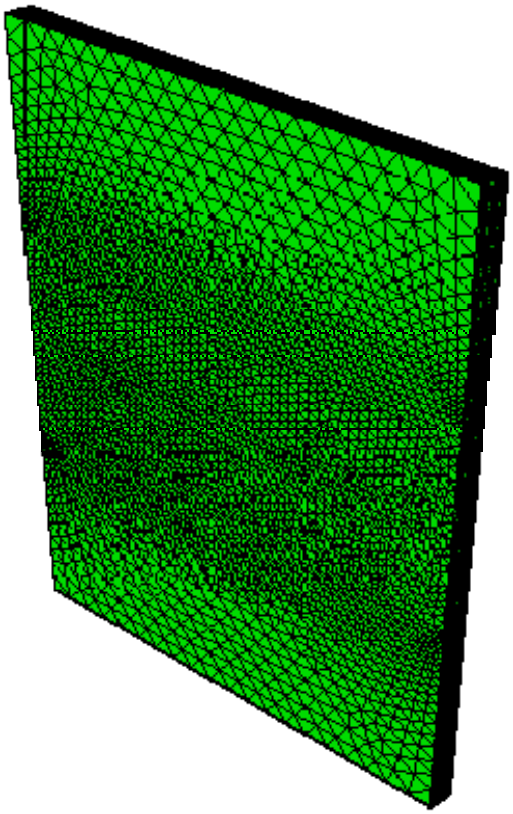

Fig. 4.13 Finite element model of E-glass/Vinyl Ester composite

The response of the CAI strength over the square of the sample thickness is plotted as a function of time as shown in Fig. 4.14. The experimental points are shown for comparison purpose. It is seen that the simulation capture the experimental model very well. The CAI strength is seen to be a function of the structural geometry and not a property of the material. There is a sharp decrease in the CAI strength/thickness^2 initially when the composite is unsaturated. This then increases when the composite becomes saturated. Our model captures this experimental response in a reasonable manner. The saturated value of CAI is lesser than the value for the dry composite at the same thickness. This is due to the degradation in material properties in case of saturated composite in comparison with the dry composite. However, the CAI strength of the

partially saturated composite is lower than that of the saturated composite (at the same square thickness) as seen in Fig. 4.14. The partially saturated composite has several plies with varying saturation percentages which have different material properties. From Table 4.3, it is seen that all the plies are partially saturated or fully saturated even at a time period of 1 month. Thus, there is an uneven degradation in material properties across the composite. There is also a material property mismatch between the different plies in the composite. This leads to a greater loss in CAI strength than the saturated composite. There is a 16 percent overall decrease in the CAI strength per unit square thickness between the dry and the saturated composite. However, there is a maximum of 23 percent decrease in the CAI strength between the dry composite and partially saturated composite. It is thus seen that the CAI strength is a property of the structural geometry of the composite rather than an intrinsic material property.

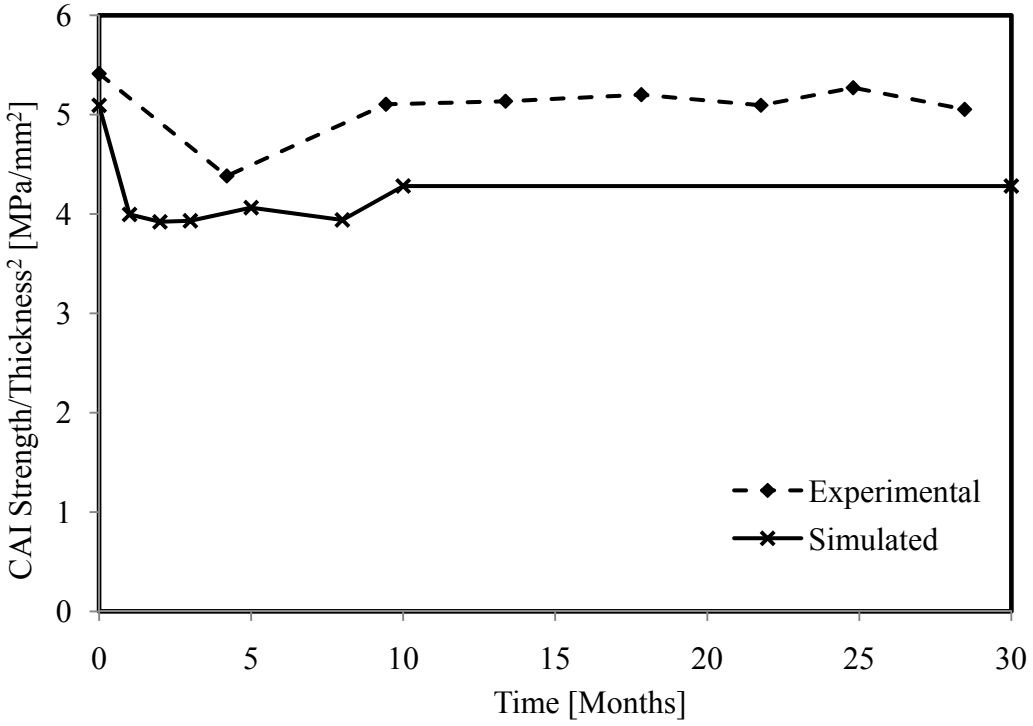

Fig. 4.14 Variation of CAI strength/thickness^2 as a function of time in months.

4.4 Conclusions

This chapter reports a combined experimental and numerical investigation on the evaluation of CAI strength of E-glass/Vinyl Ester composite subject to sea water exposure. A novel experimental technique has been developed to ensure that the composite panels are exposed to sea water instead of being immersed. This ensures that the boundary conditions in real life are replicated in the laboratory. The CAI strength is determined as a function of time for a period of about 30 months. A reduced order multiscale model is used to capture the damage mechanisms responsible for the degradation in material properties. It is shown that the CAI strength is a structural rather than a material property. The numerical model captures the decrease in unsaturated properties well due to the availability of experimental data. The lack of experimental data for saturated material properties leads to lesser accuracy in the prediction of saturated CAI properties using the numerical model.

CHAPTER V

CONCLUSIONS AND FUTURE RESEARCH

This dissertation has been focused on the interfacial fracture of bonded polymers and composites. A general motivation for this research has been the need for experimental data to verify theoretical criterions and to conduct numerical simulations. A brief overview of the completed objectives and new directions for future research are provided in this chapter.

A new short-beam shear fracture (SBSF) approach has been developed using the existing Iosipescu fixture. This approach is used to measure the mode-II fracture toughness of bonded polymers and unidirectional composites with preferred interfaces. Our approach is more efficient than previous methods due to a more accurate measurement of the failure load and due to the absence of friction between the crack faces. Also, experiments to determine the tensile, shear and fracture properties for bulk materials (polycarbonate and PMMA) and for bonded polymers and polymer/aluminum material systems has been carried out to generate necessary data for numerical simulations.

Failure prediction in brittle material traditionally follows a strength approach or a fracture toughness approach. A recently proposed criterion by Leguillon combines the two approaches and provides a novel failure criterion for fracture from notches. This dissertation provides a systematic experimental investigation for notch specimens with a connected interface. Both, same-material and bi-material configurations are used to

provide a wealth of experimental data which is expected to aid in the verification of the failure criterions. Also, the experimental data is expected to serve as a benchmark for future numerical simulations.

E-glass/vinyl ester composites belong to a class of composites called high performance composites. They are being successfully used by the navy in recent years. The evaluation of durability in such materials has been of primary concern. In this dissertation, systematic experimental investigations have been conducted over a period of 28 months to characterize the compression-after-impact strength of E-Glass/Vinyl Ester composites exposed to sea water. The damage in the composite due to sea water exposure is explained using a reduced order multiscale computational model. The impact-induced damage mechanism due to sea water is captured numerically and the results are shown to be similar to the experimental values.

Future research involves testing unidirectional composites using the SBSF approach. Currently only bonded polymers have been tested using this approach. Testing unidirectional composites would extend the practicality of this approach due to the wide applications of composite materials. Another area of future research would be to extend the method to calculate pure shear fracture properties of bi-material interfaces. Carbon fiber composites are also being by the navy due to their attractive strength properties. Evaluation of durability in carbon fiber composites will be of primary importance in the future.

REFERENCES

Abrate S (1998) Impact on composite structures, Cambridge University Press, New York.

Anderson TL (2004) Fracture mechanics: Fundamentals and applications, 3rd Edn. CRC Press.

Apicella A, Migliaresi C, Nicodemo L, Nicolais L, Iaccarino L, Roccotelli S (1982) Water sorption and mechanical properties of a glass-reinforced polyester resin, Composites, 13(4), 406-410.

Apicella A, Migliaresi C, Nicodemo L, Nicolais L, Iaccarino L, Roccotelli S (1983) The water ageing of unsaturated polyester-based composites: influence of resin chemical structure, Composites, 14(4), 387-392.

Arrese A, Carbjal N, Vargas G, Mujika F (2010) A new method for determining mode II R-curve by the End-Notched flexure test, Engineering Fracture Mechanics, 77, 51-70.

ASTM D1141 (2008) Standard practice for the preparation of substitute ocean water.

ASTM D5379 (2005) Standard test method for shear properties of composite materials by the V-notched beam method.

ASTM D7137 (2007) Standard test method for compressive residual strength properties of damaged polymer matrix composite plates.

Ayatollahi MR, Aliha MRM (2006) On determination of mode II fracture toughness using semi-circular bend specimen, International Journal of Solids and Structures, 43, 5217-5227.

Bansal A, Kumosa M (1998) Analysis of double edge-cracker Iosipescu specimens under biaxial loads, Engineering Fracture Mechanics, 59(1), 89-100.

Baucom JN, Rohatgi A, Pogue WR, Thomas JP (2006) Carbon nanofiber reinforced polymers, Materials Science and Technology, 2006 NRL Review, 1-2.

Bhattacharjee D, Knott JF (1995) Effect of mixed mode I and II loading on the fracture surface of polymethyl methacrylate (PMMA), International Journal of Fracture, 72, 359-381.

Bing Q, Sun CT (2007) Effect of compressive transverse normal stress on mode II fracture toughness in polymeric composites, International Journal of Fracture, 145, 89-97.

Boeing 787 Fact Sheet, http://www.boeing.com

Camacho GT, Ortiz M (1996) Computational modeling of impact damage in brittle materials, International Journal of Solids and Structures, 33, 2899-2938.

Cantwell WJ, Morton J (1991) The impact resistance of composite materials-a review, Composites, 22(5), 347-362.

Carpinteri A (1987) Stress-singularity and generalized fracture toughness at the vertex of re-entrant corners, Engineering Fracture Mechanics, 26(1), 143-155.

Coker D, Rosakis AJ (2001) Experimental observations of intersonic crack growth in asymmetrically loaded unidirectional composite plates, Philosophical Magazine A, 81(3), 571-595.

Comninou M (1977) The interface crack, Journal of Applied Mechanics, 44(4), 631-637.

Daniel, I. M. http://www.composites.northwestern.edu/

Daniel IM, Ishai O (2005) Engineering mechanics of composite materials, 2nd edn. Oxford University Press, New York.

Derakane 8090 Epoxy vinyl ester resin Material Property Sheet (2005)

Dunn ML, Suwito W, Cunningham S (1997a) Stress intensities at notch singularities. Engineering Fracture Mechanics, 57(4), 417-430.

Dunn ML, Suwito W, Cunningham S (1997b) Fracture initiation at sharp notches: Correlation using critical stress intensities, International Journal of Solids and Structures, 34(29), 3873-3883.

Erdogan F, Sih GC (1963) On the crack extension in plates under plane loading and plane shear, Journal of Basic Engineering, 85, 519-527.

El-Hajjar R, Haj-Ali R (2004) In-plane shear testing of thick-section pultruded FRP composites using a modified Arcan fixture, Composites Part B: Engineering, 35(5), 421-428.

Fett T (2005) Influence of a finite notch root radius on fracture toughness, Journal of European Ceramic Society, 25(5), 543-547.

Gellert EP, Turley DM (1999) Seawater immersion ageing of glass-fiber reinforced polymer laminates for marine applications, Composites: Part A, 30, 1259-1265.

Geng Y, Liu MY, Li J, Shi XM, Kim JK (2008) Effects of surfactant treatment on mechanical and electrical properties of CNT/epoxy nanocomposites, 39, 1876-1883.

Gomez FJ, Elices M (2003) A fracture criterion for sharp V-notched samples, 123, 163-175.

Gradin PA, Gustafson CG, Hojo M (1991) The influence of friction on the compliance and crack work rate on an end notched flexure specimen, Journal of Testing and Evaluation, 19(2), 149-154.

Grediac M, Pierron F, Vautrin A (1994) The Iosipescu in-plane shear test applied to composites: A new approach based on displacement field processing, 51(3), 409-417.

Griffith AA (1921) The phenomena of rupture and flow in solids, Philosophical Transactions of the Royal Society of London A, 221, 163–198.

Guedes JM, Kikuchi N (1990) Preprocessing and postprocessing for materials based on the homogenization method with adaptive finite element methods, 83, 143-198.

Hellen TK, Blackburn WS (1975) The calculation of stress intensity factors for combined tensile and shear loading, International Journal of Fracture, 27, 157-170.

Hutchinson J, Suo Z, (1992) Mixed-mode cracking in layered materials, Advances in Applied Mechanics 29, 63-191.

Imielinska K, Guillaumat L (2004) The effect of water immersion ageing on low-velocity impact behaviour of woven aramid–glass fibre/epoxy composites, Composite Science and Technology, 64, 2271–2278.

Irwin G (1957) Analysis of stresses and strains near the end of a crack traversing a plate, Journal of Applied Mechanics 24, 361–364.

Kadomateas GA (1999) Post-buckling and growth behavior of face-sheet delaminations in sandwich composites, AMD-Vol. 235, Thick Composites for Load Bearing Structures, (Y.D.S. Rajapakse and G.A. Kadomateas, Ed.), 51-60.

Karasek MC, Strait LH, Amateau MF (1995) Effect of temperature and moisture on the impact behaviour of graphite/epoxy composites: parts I and II. Journal of Material Research and Technology 17(1), 3–15.

Karbhari VM, Zhang S (2003) E-glass/Vinylester composites in aqueous environments-I: Experimental results, Applied Composite Materials, 10, 19-48.

Kootsookos A, Mouritz AP (2004) Seawater durability of glass- and carbon-polymer composites, Composites Science and Technology, 64, 1503-1511.

Krishnan A, Xu LR (2010) Effect of the interfacial stress distribution on the material interfacial strength measurement, Experimental Mechanics, 50, 283-288.

Krishnan A, Xu LR (2011a) Systematic evaluation of bonding strengths and fracture toughnesses of adhesive joints, *Journal of adhesion, (in press).*

Krishnan A, Xu LR (2011b) A short-beam shear fracture approach to measure the mode II fracture toughness of materials with preferred interfaces, *Submitted to International Journal of Fracture*.

Krishnan A, Xu LR (2011c) An integrated experimental and numerical analysis into notch and interface interactions in same-materials, *Manuscript in preparation*.

Kobayashi AS (ed) (1987) Handbook on experimental mechanics, Society of Experimental Mechanics, Inc. Prentice-Hall, New Jersey.

Leguillon D (2002) Strength or toughness? A criterion for crack onset at a notch, European Journal of Mechanics A/Solids, 61-72.

Leguillon D, Yosibash Z (2003) Crack onset at a V-notch. Influence of the notch-tip radius, International Journal of Fracture, 122, 1-21.

Li XF, Xu LR (2007) T-Stresses across static crack kinking, ASME Journal of Applied Mechanics, 74, 181-190.

Liao K, Schultheisz CR, Hunston DL (1999) Effects of environmental aging on the properties of pultruded GFRP, Composites: Part B, 30, 485-493.

Liechti KM, Chai Y-S (1991) Biaxial loading experiments for determining interfacial fracture toughness, Journal of Applied Mechanics, 58, 680-687.

Lin C-P, Douglas WH (1994) Failure mechanisms at the human dentin-resin interface: A fracture mechanics approach, Journal of Biomechanics, 8, 1037-1047.

Matthewson MJ (1993) Models for fiber reliability, Proceedings of the SPIE-The International Society for Optical Engineering, 1973, 128-137.

Melin LN, Neumeister JM (2006) Measuring constitutive shear behavior of orthotropic composites and evaluation of the modified Iosipescu test, Composite Structures, 76(1-2), 106-115.

Metcalfe AG, Schmitz GK (1972) Mechanism of stress corrosion in E glass filaments, Glass Technology, 13(1), 5-16.

Mouritz AP, Mathys Z (1999) Post-fire mechanical properties of marine polymer composites, Composites Structures, 47, 643-653.

Murthy HNN, Sreejith M, Krishna M, Sharma SC, Sheshadri TS (2010) Seawater durability of epoxy/vinyl ester reinforced with glass/carbon composites, Journal of Reinforced Plastics and Composites, 29(10), 1491-1499.

O'Dowd NP, Shih CF, Stout MG (1992) Test geometries for measuring interfacial fracture toughness, International Journal of Solids and Structures, 29(5), 571-589.

Oguni K, Ravichandran G (2001) Dynamic compressive behavior of unidirectional E-glass/vinylester composites, Journal of Materials Science, 36, 831-838.

ONR Fact Sheet (2008) Carbon Nanotubes Composites Program, ONR Program Code 33.

Pillay S, Vaidya UK, Janowski GM (2005) Liquid molding of carbon fabric-reinforced nylon matrix composite laminates, Journal of Thermoplastic Composite Materials, 18 (6), 509-527.

Priel E, Bussiba A, Gilad I, Yosibash Z (2007) Mixed mode failure criteria for brittle elastic V-notched structures, International Journal of Fracture, 144(4), 247-265.

Qian J, Fatemi A (1996) Mixed mode fatigue crack growth-A literature survey, Engineering Fracture Mechanics, 55(6), 969-990.

Qian H, Sun CT (2008) Effect of bondline thickness on mode I fracture in adhesive joints, Proceedings of the 2008 AIAA SDM Conference, Schaumburg, IL.

Ramirez FA, Carlsson LA, Acha BA (2008) Evaluation of water degradation of vinylester and epoxy matrix composites by single fiber and composite tests, Journal of Material Science, 43, 5230-5242.

Rice JR (1988) Elastic fracture mechanics concepts for interfacial cracks, Journal of Applied Mechanics, 55, 98-103.

Rice JR, Sih GC (1965) Plane problems of cracks in dissimilar media, Journal of Applied Mechanics, 32, 418-423.

Rosakis AJ, Ravi-Chandar K (1986) On crack-tip stress state: An experimental evaluation of three-dimensional effects, International Journal of Solids and Structures, 22, 121-134.

Roy R, Sarkar BK, Bose NR (2001) Effects of moisture on the mechanical properties of glass fiber reinforced vinylester resin composites, Bulletin of Material Sciences, 1, 87-94.

Ruiz G, Pandolfi A, Ortiz M (2001) Three-dimensional cohesive modeling of dynamic mixed-mode fracture, International Journal Numerical Methods in Engineering, 52, 97-120.

Sagi-Mana D, Narkis M, Siegmann A, Joseph R, Dodiuk H (1998) The effect of marine environment on a vinyl ester resin and its highly filled particulate quartz composites, Journal of Applied Polymer Science, 69, 2229-2234.

Sala G (2000) Composite degradation to fluid absorption, Composites Part B 31, 357-377.

Seweryn A (1994) Brittle fracture criterion for structures with sharp notches, Engineering Fracture Mechanics, 47(5), 673-681.

Smith LV, Weitsman YJ (1996) The immersed fatigue response of polymer composites, International Journal of Fracture, 82, 31-42.

Sih GC, Paris PC, Irwin GR (1965) On cracks in rectilinearly anisotropic bodies, International Journal of Fracture, 1, 189-203.

Sih GC (1974) Strain energy density factor applied to mixed mode crack problems, International Journal of Fracture, 10, 305-321.

Simo JC, Ju JW (1987) Strain- and stress-based continuum damage models, I. Formulation, International Journal of Solids and Structures, 23(7), 821-840.

Sorathia U, Ness J, Blum M (1999) Fire safety of composites in the US Navy, Composites: Part A, 30, 707-713.

Strait LH, Karasek ML, Amateau MF (1992) Effects of seawater immersion on the impact resistance of glass fiber reinforced epoxy composites, Journal of Composite Materials, 26(14), 2118- 2133.

Strandberg M (2002) Fracture at V-notches with contained plasticity, Engineering Fracture Mechanics, 69(3), 403-415.

Sullivan JL, Kao BG, Van Oene H (1984) Shear properties and a stress analysis obtained from vinyl-ester Iosipescu specimens, Experimental Mechanics, 223-232.

Sun CT (2008) Why LEFM is not applicable for bonded joints, 23rd Technical Conference, American Society for Composites, Memphis TN.

Sun CT, Qian H (2009) Brittle fracture beyond the stress intensity factor, Journal of mechanics of materials and structures, 4(4), 743-753.

Suresh S, Shih CF, Morrone A, O'Dowd NP (1990) Mixed mode fracture toughness of ceramic materials, Journal of American Ceramic Society, 73(5), 1257-67.

Tekalur SA, Shivakumar K, Shukla A (2008) Mechanical behavior and damage evolution in E-glass vinyl ester and carbon composites subjected to static and blast loads, Composites Part B: Engineering, 39, 57-65.

Theocaris PS, Andrianapoulos NP (1982) The T-criterion applied to ductile fracture, International Journal of Fracture, 20, 125-130.

Tsai J, Sun CT (2004) Dynamic compressive strength of polymeric composites, International Journal of Solids and Structures, 41, 3211-3224.

Tsotsis TK, Weitsman Y (1994) A simple graphical method for determining diffusion parameters for two-stage sorption in composites, Journal of Materials Science Letters, 13, 1635-1636.

Ulven C, Vaidya UK (2006) Post-fire low velocity impact response of marine grade sandwich composites, Composites Part A, 37 (7), 997-1004.

Walrath DE, Adams DF (1983) The Iosipescu shear test as applied to composite materials, Experimental Mechanics, 23(1), 105-110.

Wang J, Qiao P (2004) Novel beam analysis of end notched flexure specimen for mode-II fracture, Engineering Fracture Mechanics, 71, 219-231.

Weitsman YJ, Elahi M (2000) Effects of fluids on the deformation, strength and durability of polymeric composites—an overview, Mechanics of Time-Dependent Materials, 4,107–126.

Williams ML (1952) Stress singularities resulting from various boundary conditions in angular corners of plates in extension, Journal Applied Mechanics, 74, 526-528.

Williams ML (1957) On the stress distribution at the base of a stationary crack, ASME Journal of Applied Mechanics, 24, 109-114.

Williams JG, Ewing PD (1972) Fracture under complex stress-The angled crack problem, International Journal of Fracture Mechanics, 8, 441-446.

Wood CA, Bradley W, (1997) Determination of the effect of seawater on the interfacial strength of an interlayer E-glass/graphite/epoxy composite by in situ observation of transverse cracking in an environmental SEM, Composite Science and Technology, 57, 1033-1045.

Xu L, Tippur H (1995) Fracture parameters for interfacial cracks: an experimental-finite element study of crack tip fields and crack initiation toughness, International Journal of Fracture, 71(4), 345-363.

Xu L, Kou CH (1994) Effect of interfacial interleaf to the interlaminar fracture and intralaminar fracture of a new BMI matrix composites system, Journal of Reinforced Plastics and Composites, 13, 509-540.

Xu, LR, Rosakis AJ (2002) Impact failure characteristics in sandwich structures; Part I: Basic failure mode selections. International Journal of Solids and Structures, 39, 4215-4235.

Xu LR, Huang YY, Rosakis AJ (2003) Dynamic crack deflection and penetration at interfaces in homogenous materials: experimental studies and model predictions, Journal of Mechanics and Physics in Solids, 51, 461-486.

Xu LR, Rosakis AJ (2003) An experimental study on dynamic failure events in homogenous layered materials using dynamic photoelasticity and high-speed photography, Optics and Laser in Engineering, 40, 263-288.

Xu LR, Bhamidipati V, Zhong WH, Li J, Lukehart CM, Lara-Curzio E, Liu KC, Lance MJ (2004) Mechanical property characterization of a polymeric nanocomposite reinforced by graphitic nanofibers with reactive linkers, Journal of Composite Materials, 38, 1563-1582.

Xu LR, Sengupta S, Kuai H (2004a) Dissimilar material joints with and without free-edge stress singularities: Part I. A biologically inspired design, Experimental Mechanics, 44(6), 608-615.

Xu LR, Sengupta S, Kuai H (2004b) An experimental and numerical investigation of adhesive bonding strengths of polymer materials, International Journal of Adhesion and Adhesives, 24, 455-460.

Xu S, Reinhardt HW, Gappoev M (1996) Mode II fracture testing method for highly orthotropic materials like wood, International Journal of Fracture, 75, 85-214.

Yan H, Oskay C, Krishnan A, Xu LR (2010) Compression after impact response of woven fiber reinforced composites, Composites Science and technology, 70, 2128-2136.

Yosibash Z, Bussiba A, Gilad I (2004) Failure criteria for brittle elastic materials, International Journal of Fracture, 125, 307-333.

Yosibash Z, Priel E, Leguillon D (2006) A failure criterion for brittle elastic materials under mixed-mode loading, International Journal of Fracture, 141, 291-312.

Yoshihara H (2010) Mode I and mode II initiation fracture toughness and resistance curve of medium density fiberboard measured by double cantilever beam and three-point bend end-notched flexure tests, Engineering Fracture Mechanics, 77, 2537-2549.

Yoshihara H, Satoh A (2009) Shear and crack tip deformation correction for the double cantilever beam and three-point end-notched flexure specimens for mode I and II fracture toughness measurement of wood, Engineering Fracture Mechanics, 76(3), 335-346.